Bifurcations in simple models of Arctic sea ice



Edmund Derby

Wolfson College

University of Oxford

Supervised by

Raymond Pierrehumbert

A thesis submitted for the degree of *Doctor of Philosophy*

Hilary Term 2024

Contents

Acknowledgements 5
Abstract 6
Chapter 1 Introduction
1 Bifurcations and Arctic sea ice – motivation for study 7
1.1 Tipping points and bifurcations 7
1.2 Arctic sea ice and tipping points 10
2 Bifurcations in models of Arctic sea ice 12
2.1 Energy balance models 12
2.2 Intermediate complexity models 14
2.3 General circulation models 17
3 Bridging the gap between models 19
3.1 The EW09 ice model 21
4 Structure of the thesis 26
Chapter 2 The sea ice thickness distribution
1 Introduction 28
1.1 Statement of work 29
2 The ice thickness distribution 29
3 Modelling the ice thickness distribution 31
3.1 The time-evolution equation 31
3.2 The thermodynamic term 32
3.2.1 Treatment of open water 32
3.3 The advection term 35
3.4 The redistribution term 36
4 Mechanics parameterisations 37
4.1 Fokker-Planck parameterisation 37
4.1.1 Seasonal evolution and open water 39
4.1.2 Conservation of thickness 40
4.2 Coagulation parameterisation 45
4.2.1 Results using the coagulation parameterisation 49
5 Conclusions 55
Chapter 3 The Arctic single column model
1 Introduction 58

2 Key features of Arctic climate 59
2.1 Vertical temperature profile 59
2.2 Clouds 61
2.3 Horizontal heat transport 62
2.3.1 Atmospheric heat transport 63
2.3.2 Oceanic heat transport 64
3 The single column model 65
3.1 Outline of homebrew model components & modifications 69
3.1.1 Cloud scheme 69
3.1.2 Atmospheric heat transport 76
3.1.3 Sea ice 77
4 Model parameters and fit with reanalysis 78
4.1 Tuning the model 78
4.1.1 Column latitude and solar zenith angle 78
4.1.2 Wind speed 79
4.1.3 Cloud parameters 80
4.2 Comparison with reanalysis data 81
5 Summary 84

Chapter 4 Local atmospheric processes

1 Introduction 85
1.1 An important note 86
2 The clear sky column model 86
2.1 Bifurcation structure 86
2.2 The effect of vertical resolution 90
3 The cloudy column model 94
4 Sensitivity to heat transport structure 100
5 Conclusions 102

Chapter 5 Atmospheric heat transport

1 Introduction 106
2 Methods 108
2.1 Dry heat transport feedback 108
2.2 Moist heat transport feedback 111
3 Results 111
3.1 Introducing heat transport feedbacks 111
3.2 Sensitivity to dry heat transport feedback strength 114

3.3 Sensitivity to climate sensitivity 117
4 Conclusions 119

Chapter 6 Conclusions

1 Introduction 122
2 Conclusions 122
3 Further work 126
Bibliography 129

Acknowledgements

First of all, I would like to thank my supervisor, Raymond Pierrehumbert, for his guidance and insight across this project and for always managing to make me feel good after a supervision meeting.

I would also like to thank Srikanth Toppaladoddi for his help and support on my work using the ice thickness distribution without which I couldn't have tackled this area.

I'm deeply thankful to my friends in Oxford and beyond for giving me so many fond memories of the past four years and being such a generous support network. Special mentions must go to Tim Hempel, Andrew Styles, Matt Sutton, Emily van de Koot and Andrew Williams for being such great friends since the beginning of the DTP; and to Sally Blumenthal, Richard Chatterjee, Namrah Habib and Hamish Innes for being the best office mates I could have asked for.

During the summer of my third year I was fortunate to take part in a UKRI policy internship in the Government Office for Science. I'm very grateful to Amy Fairchild and the whole NSAR team circa March-June 2022 for giving me such a warm welcome to the world of government and a well-timed break from research.

Finally, I would like to give my biggest thanks to my parents and to Anna Wang for being there to give support every moment I needed it. This would have been a very different experience without them, and worse for it.

Abstract

The observed rapid decline of Arctic sea ice has raised concerns that anthropogenic warming could cause the abrupt loss of sea ice by passing a saddle-node bifurcation. A variety of simple models exhibit this behaviour, however most GCM studies simulate a smooth loss of sea ice without passing a bifurcation point. In this thesis I attempt to bridge the gap between these types of models by adding additional features to simple models and assessing their impact on the models' bifurcation structures.

I use the ice thickness distribution to resolve the effect of variability and mechanical processes within sea ice. My results indicate that, with an appropriate choice of parameterisation, mechanical processes reduce bistability in the system – likely induced by positive fluxes into open water being translated into an increased bottom heat flux.

I also use a single column model of the Arctic atmosphere coupled to a slab sea ice model to explore the impact of atmospheric processes. In the absence of heat transport feedbacks, the system exhibits broad perennially ice-covered and ice-free states separated by bifurcation points in clear sky and cloudy configurations. I find that the resolution of temperature inversions appears to destabilise the ice-covered state. I also find stabilising negative feedbacks from low clouds when ice-covered, and elevated clouds when ice-free, that strengthen bistability in the system.

Feedbacks in atmospheric heat transport significantly alter the bifurcation structure of the system – introducing a smooth loss of summer sea ice and significantly reducing the size of the bistable region. The bistable region shrinks further for stronger meridional heat transport and stronger warming of lower latitudes.

Chapter 1 Introduction

"Instead of my world, there would soon be only ice"

Ice, Anna Kavan

1 Bifurcations and Arctic sea ice – motivation for study

1.1 Tipping points and bifurcations

In recent years there has been a lot of attention given to tipping points in the Earth's climate. Lenton (2013) defines these as points at which a small change of a controlling parameter can cause qualitative change in the future state of a component of the Earth's climate (termed a 'tipping element'). If tipping points exist on potential trajectories for anthropogenic warming they would dramatically alter climate projections. In addition, if tipping points are associated with hysteresis or quasi-hysteresis then changes associated with them may be non-reversible on policy-relevant timescales. Tipping points have also been proposed as mechanisms behind abrupt transitions in Earth's palaeoclimate record (Brovkin *et al.*, 2021).

Of particular interest are tipping points where a small change of the controlling parameter causes the system to change to occupy an alternative stable state. For a slowly varying system with no internal-variability or noise, the parameter values at which the stability of the system changes are called bifurcation points. If crossing a bifurcation point results in a qualitative change in the system's state it is called a catastrophic bifurcation (Zeeman, 1982).

Figure 1 presents a system showing a common 'saddle-node' bifurcation seen in many simple climate models (e.g. Eisenman & Wettlaufer, 2009; Stommel, 1961). Here L_1 and L_2 are saddle-node bifurcation points marking the points where the

stable (solid) lines cease to be stable. If the system evolves past one of these points it would collapse into the alternative stable state. Pairs of saddle-node bifurcation points are linked by a third unstable state, represented here by a dashed line. Notably, if the system passes a bifurcation point and settles into the alternative stable state, and the bifurcation parameter is then slowly adjusted in the *reverse direction* the system will not return to its initial state until it passes the other bifurcation point. This non-reversible hysteresis behaviour is a hallmark of systems with saddle-node bifurcations and is often used as a test for detecting multistable states.

It should be noted that it can be difficult to detect bistability in a system by examining its transient response to changes in the bifurcation parameter. Li *et al.* (2013) find that a monostable GCM with an abrupt transition behaves very similarly to a bistable system when forced with slowly increasing CO_2 concentrations. This indicates that it is difficult to determine from transient observations whether a system is bistable. Similarly, Wagner and Eisenman (2015a) demonstrate that 'early warning signals' such as increased auto-correlation that are often used to detect a nearby tipping point can be seen in a system without bistability or an abrupt transition.

I am particularly interested in investigating bistability associated with saddle-node bifurcations as it is associated with a loss of reversibility and it can be seen in a variety of simple sea ice models (Eisenman, 2012).

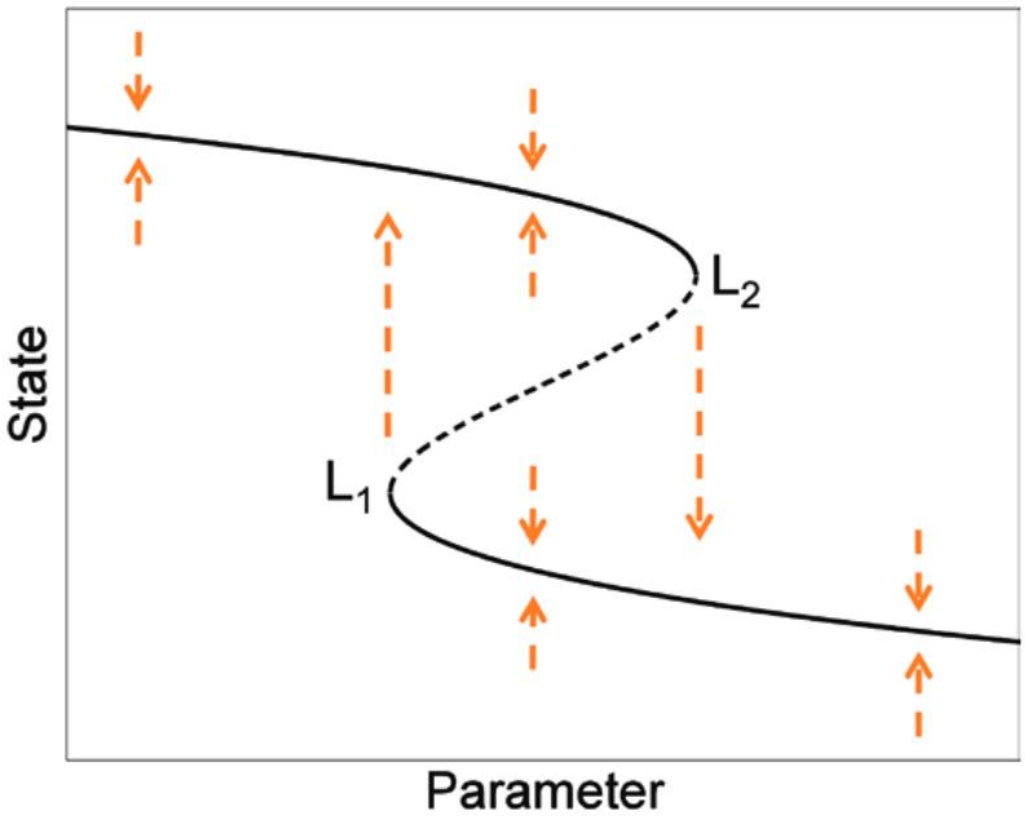


Figure 1 A bifurcation diagram showing the stable states (solid black lines) and unstable state (dashed black line) of a system with a pair of saddle-node bifurcations controlled by an arbitrary parameter. The system's attraction to the stable states is indicated by the dashed orange arrows. Points L_1 and L_2 mark the system's bifurcation points at which the stable states cease to be stable. Taken from Bathiany et al. *(2016).*

It is important to note that for a system's with multiple stable states there is more than one way it can transition from one stable state to another. Ashwin *et al.* (2012) identify 3 kinds of tipping behaviour for systems with saddle-node bifurcations.

- **Bifurcation-induced tipping** is the classic case where the bifurcation parameter is slowly adjusted such that the system follows the steady state up until a bifurcation point where the state ceases to be stable, leading the system to collapse into another stable state.
- **Noise-induced tipping** occurs when noise or internal variability in the system is strong enough to push the system into the attracting region of a different stable state while the initial state is still stable.

- **Rate-induced tipping** occurs when the bifurcation parameter is adjusted too quickly for the system to relax into the attracting region of its initial state and becomes attracted to a different state while the initial state is still stable.

Through noise-induced and rate-induced tipping, a system can tip into a qualitatively different state *before* it has passed a bifurcation point. Both behaviours become more likely as the system approaches the bifurcation point and the initial steady state becomes less attractive. They are also more likely for stronger noise/internal variability and faster rates of change.

Throughout this thesis I focus on mapping the steady state behaviour of systems so I don't consider noise- and rate-induced tipping directly, but they are important factors to consider when interpreting the potential evolution of a system with multiple stable states.

Saddle-node bifurcations have been observed in simple models of a range of different climate processes including: sea ice cover (Budyko, 1969; Sellers, 1969), the AMOC (Stommel, 1961), and the Indian monsoon (Zickfeld *et al.*, 2005). In each of these models bistability exists as a result of a strong state-dependent positive feedback. When such a feedback is strong enough it allows for two states to be stable in the same conditions. Lenton *et al.* (2008) and Bathiany *et al.* (2016) provide wider reviews of features of the Earth's climate that may undergo tipping points.

Throughout this thesis I will examine models that show saddle-node bifurcations associated with the loss of Arctic sea ice.

1.2 Arctic sea ice and tipping points

Sea ice plays a critical role in constraining the contemporary Arctic climate. It acts as an insulating layer between the ocean and atmosphere. The high albedo of sea ice (particularly when thick and/or snow covered) reflects the majority of solar

radiation from the surface and results in a vastly different surface energy budget compared to the open ocean (Perovich and Polashenski, 2012). The thermal properties of sea ice control the surface temperature of the ice-covered Arctic in a completely different way to open ocean, e.g. pinning the surface temperature when the ice top surface is ablating. In addition to its myriad effects on climate, sea ice is crucial for the existence of current Arctic ecosystems (Post *et al.*, 2013).

Arctic sea ice is currently being lost at a rapid rate, with the decline sharpest in summer – seen, for example, in PIOMAS reanalysis data available through to 2023 (Schweiger *et al.*, 2011). This rapid ice loss is linked to the amplification of warming in the Arctic, driven by a range of factors including the ice-albedo feedback, changes in the Arctic lapse rate and changes in heat transport convergence (e.g. Henry et al., 2021). This has led to widespread interest in the existence of a tipping point in Arctic sea ice cover and the potential for sea ice loss under anthropogenic warming to be irreversible due to hysteresis in the system.

Abrupt sea ice loss could have significant consequences on local atmospheric circulation (Liu *et al.*, 2016) and global circulation (Semmler *et al.*, 2016), as well as putting incredible strains on Arctic ecosystems and communities.

Tipping points in Arctic sea ice are also relevant to our understanding of Earth's paleoclimate. Stable warm, ice-free states at low CO_2 levels have been proposed as an explanation for equable climates in Earth's past (e.g. Abbot & Tziperman, 2008).

Seasonal cycles in ice cover allow for a range of possible bifurcation structures for the Arctic sea ice system. Eisenman (2012) classify 4 possible scenarios for the loss of Arctic sea ice, each of which have been simulated in low-order seasonal models:

1. Completely continuous and reversible transition from a perennially ice-covered to a perennially ice-free state. In this case the system does not exhibit bifurcations. (e.g. Wagner and Eisenman, 2015b).
2. Continuous and reversible loss of summer sea ice with a pair of saddle-node bifurcations separating a seasonally ice-free Arctic from a perennially ice-free state (e.g. Eisenman & Wettlaufer, 2009).
3. Saddle-node bifurcations separating a perennially ice-covered and a perennially ice-free state. There is either no seasonally ice-free state or the seasonally ice-free state cannot be reached by smooth evolution from the perennially ice-covered and ice-free states (e.g. Thorndike, 1992).
4. Saddle-node bifurcations separating a perennially ice-covered and a seasonally ice-free state, potentially coexistent with a pair of bifurcations separating the seasonally ice-free state from a perennially ice-free state as in scenario 2 (e.g. Abbot et al., 2011).

A range of models have been used to investigate the nature of the transition to a perennially ice-free Arctic. In the following section I give an overview of previous work done in this area.

2 Bifurcations in models of Arctic sea ice

2.1 Energy balance models

Bistable sea ice states separated by a saddle-node bifurcation were first observed in energy balance models (EBMs) that considered an annual-average climate state described by a single temperature coordinate with a non-linear temperature dependent albedo. See North (1990) for a more comprehensive review.

0-dimensional EBMs (representing the *global average* climate state) find two stable states separated by a saddle-node bifurcation: one close to the contemporary

climate and a low-albedo state with temperature well below the freezing point of water (Budyko, 1969).

Extending these models to simulate the zonally and annually averaged temperature field across a hemisphere of the Earth with a diffusive heat transport term introduces an additional steady state (Budyko, 1969; Sellers, 1969). Here the model can exist in stable states that: are fully ice-covered, are fully ice-free, or contain an ice-edge in the mid-latitudes. These states are separated by two pairs of saddle-node bifurcations. The bifurcation point separating the partially ice-covered hemisphere from the totally ice-free state is often termed the small ice cap instability (SICI) (Figure 2). In these models when ice cover would retreat beyond $\sim 70\ ^{\circ}N$ the system collapses into an ice-free state.

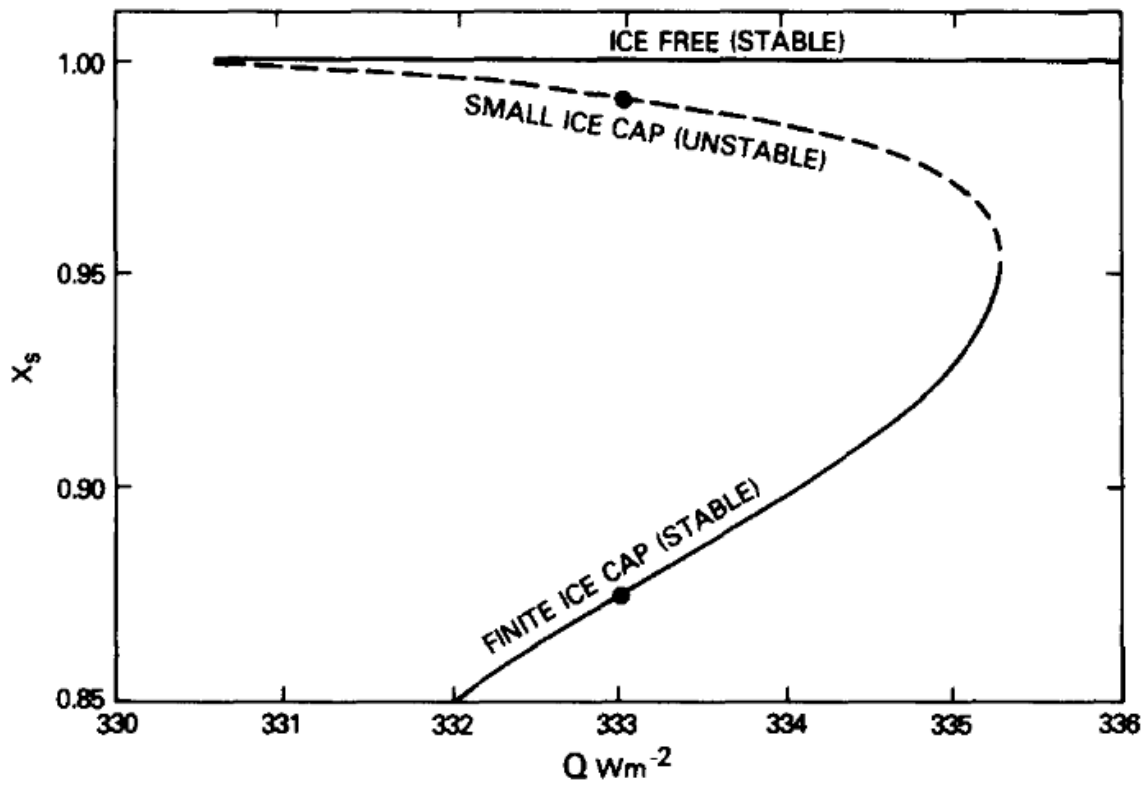


Figure 2 A detail of a bifurcation diagram of a 1-dimensional energy balance model showing 3 stable states. The model state is represented by the sine of the latitude of the ice edge, x_S. Here the finite ice cap and ice-free

states are visible (solid black lines) separated by the SICI unstable state (dashed line). For ice edges at latitudes greater than ~70 °N ice caps are unstable. Taken from North (1990).

Mengel, Short and North (1988) investigate the impact of seasonal variation by introducing a seasonally varying insolation. They continue to find bistable states with a perennially ice-covered pole and a seasonally ice-covered pole separated by a pair of bifurcation points. However, their system has a lower heat capacity near the poles which more closely aligns with a land-covered region than with an Arctic-like ocean-covered pole.

2.2 Intermediate complexity models

A range of other simplified models have been used to investigate sea ice bifurcations. In contrast to EBMs discussed above, many of these model the thickness evolution of sea ice based on a simplification of the theory of Maykut and Untersteiner (1971). *(Note: In some of the literature these models are referred to as single column models, to avoid confusion with models with vertically resolved atmospheres I will use the term* 0-dimensional models *as these models tend to describe sea ice as a point-like quantity described by a thickness variable. It should be noted that the original Maykut and Untersteiner (1971) paper has a resolved vertical dimension within the ice pack.).*

Thorndike (1992a) was among the first to demonstrate the existence of bistable states in a 0-dimensional model of the Arctic with resolved ice thickness. They represent the thermodynamic growth of ice using a simple two-season representation of seasonality with constant insolation during a cold and warm season. With this model they find a stable perennially ice-free and perennially ice-covered state, but no seasonally ice-free state. However, Moon and Wettlaufer (2012) demonstrate that the nature of this bifurcation is an artefact of the reduced

time resolution of the model. By allowing greater resolution of the seasonal cycle a smooth loss of summer sea ice is achieved.

Eisenman and Wettlaufer (2009) use a similar 0-dimensional model with a simplified thermodynamic model of sea ice growth (neglecting the vertical temperature profile and heat capacity of ice) and significantly greater time resolution. They find a smooth loss of summer sea ice and a saddle-node bifurcation associated with the loss of winter sea ice (Figure 3 (right)) when using prescribed seasonal cycles of fluxes at the ice surface. They also demonstrate that the seasonally ice-free state is made possible by the ice-growth rate feedback. The thermodynamic growth rate of ice is controlled by the vertical heat flux within the ice pack which is to first order inversely proportional to the thickness. This means thin ice grows much faster than thick ice. This thickness dependence is less pronounced during the melt season as surface temperatures are pinned to the melting point of ice. This feedback stabilises seasonally ice-free states. When the model is run without this feedback it only allows perennially ice-covered and perennially ice-free states (Figure 3 (left)).

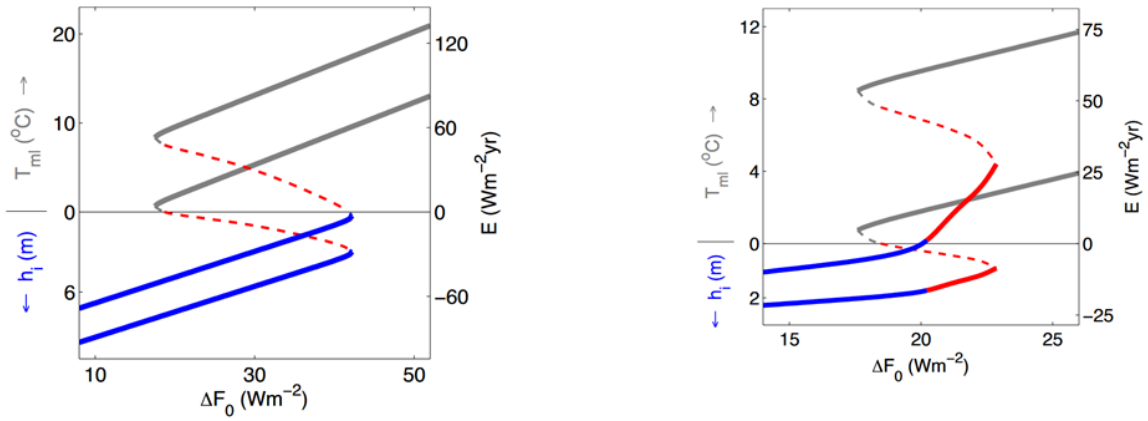


Figure 3 Bifurcation diagrams from the seasonally forced Eisenman and Wettlaufer (2009) for a constant bifurcation parameter ΔF_0 representing a surface radiative forcing perturbation. Each state for a given ΔF_0 is represented by a pair of lines. The lower line represents the winter extreme and the upper line the summer extreme. Solid lines represent stable states of the system and dashed lines unstable states. Blue lines are perennially ice-covered, red lines seasonally ice-free and grey lines perennially ice-free. The left-hand panel

shows the results for the model run without the ice-growth rate feedback. For a window of ΔF_0 values between $\sim 20\ Wm^{-2}$ and $\sim 40\ Wm^{-2}$ 3 states coexist: a stable perennially ice-covered state, a stable perennially ice-free state and an unstable seasonally ice-free state. The right-hand panel shows the bifurcation diagram when the ice-growth rate feedback is included. Here 3 states coexist between $\sim 18\ Wm^{-2}$ and $\sim 23\ Wm^{-2}$: a stable ice-covered state with a smooth transition between perennial and seasonal ice cover, a stable perennially ice-free state, and an unstable seasonally ice-free state.

Several studies have used the ice model used in Eisenman and Wettlaufer (2009) (henceforth referred to as EW09) as the basis for exploring the effect of additional climate features.

Wagner and Eisenman (2015b) combine the approaches of EW09's 0-dimensional model with heat transport resolving EBMs. They use a latitude resolving model of a hemisphere of the Earth with diffusive heat transport and the model surface represented using the EW09 model (that allows for a given point on the surface to exist in an ice-covered or ice-free mixed layer state). They found that the introduction of the diffusive heat transport term eliminated the saddle-node bifurcation giving a smooth, monostable transition from an ice-covered Arctic to an ice-free Arctic. Note that while this eliminated the SICI, the snowball bifurcation associated with the abrupt transition to a globally ice-covered state still existed in this configuration. When seasonality or heat transport were 'switched off' they recovered the multistable states seen in seen in Budyko (1969) and Sellers (1969) and Eisenman and Wettlaufer (2009) respectively. This result is in contrast to the bistable seasonally varying EBM in Mengel, Short and North (1988) – this discrepancy could be explained by the lack of ice thermodynamics and low heat capacity of the poles in Mengel, Short and North (1988). Aylmer, Ferreira and Feltham (2020) find that in an atmospheric EBM coupled to a representation of oceanic heat transport the ice edge position is more sensitive to changes in oceanic heat transport than atmospheric heat transport.

Abbot, Silber and Pierrehumbert (2011) explored the effect of clouds by introducing a simple parameterisation to a 0-dimensional version of EW09. They modify the surface albedo and downwelling longwave flux to represent Arctic cloud cover. Depending on the choice of parameters this model can exhibit 3 distinct stable states: a perennially ice-covered state, a seasonally ice-free state and a perennially ice-free state. These are separated by two pairs of saddle-node bifurcations. A shortcoming of this model is that it does not include vertical resolution of the atmosphere so cannot accurately represent the effect of the vertical structure of the atmosphere on the surface cloud radiative effect. In a more sophisticated model Abbot and Tziperman (2008, 2009) show that a bistable region with ice-covered and ice-free stable states can be maintained in a column model of the Arctic through the longwave effect of high convective clouds.

Moon and Wettlaufer (2017) introduced a stochastic noise term to the EW09 model. They found that with an additive noise term the system can reach a bistable state at a *lower* ΔF_0 value than in the non-stochastic case. They found that when in a bistable regime the system would exist in one of the two stable states with long dwell times and abrupt transitions to the alternate state.

2.3 General circulation models

There has also been widespread investigation of tipping points in sea ice using general circulation models (GCMs). As these are much more complicated and computationally intensive it is more difficult to use the methods used for simple models such as constructing Poincaré maps for stable and unstable states or covering a wide range of parameter space to search for stable states.

Holland, Bitz and Tremblay (2006) found periods of abrupt sea ice loss in GCM simulations following IPCC emissions scenarios through to 2100, but no evidence

to suggest these were transitions to alternative stable states. Tietsche *et al.* (2011) saw that when sea ice was artificially set to zero at various points along a climate trajectory for predicted 21st century emissions it quickly recovered to its previous state, suggesting the system is not bistable in the conditions tested. A weakness of this method is that if two stable states existed, the size of this perturbation might not be enough to change states.

Armour *et al.* (2011) and Ridley, Lowe and Hewitt (2012) both use a hysteresis method to test for sea ice bifurcations in GCMs. They smoothly increase atmospheric CO_2 concentrations until the Arctic becomes ice-free and then decrease them to their initial levels. In both experiments Arctic sea ice reforms reversibly without any hysteresis which would be expected in a bistable system if the system had stabilised into an alternative state. Winton (2006b, 2008b) however found different behaviour in two GCMs with one showing smooth loss of sea ice in smoothly increasing atmospheric CO_2 simulations and another showing an abrupt transition from a seasonally ice-free to a perennially ice-free state similar to a SICI event. This highlights a key difficulty in GCM studies as the cause of qualitatively different results like this is very difficult to isolate. Similar to Wagner and Eisenman (2015b), Winton (2008) identify changes in atmospheric heat transport as the principle damping mechanism controlling the linearity of sea ice loss in GCMs. This is because reduced heat transport for warm ice-free states prevents them from being stable at the same CO_2 concentrations as ice-covered states. A similar result is seen in an updated version of the GCM in Notz *et al.* (2013). When the model is allowed to run to equilibrium for a given CO_2 concentration Li *et al.* (2013) demonstrate that while the model undergoes abrupt change when losing winter sea ice it only ever has one stable state, but has very slow relaxation times (~ 1000 years) near the abrupt transition. The abrupt change in this model is

strengthened by the onset of convection in the Arctic, similar to Abbot and Tziperman (2008). In their model, wintertime convection stabilises the ice-free state for lower CO_2 concentrations due to the formation of warming high clouds. This behaviour is consistent with the idealised case of a monostable system with positive feedback just weak enough to not have a saddle node bifurcation (Lenton, 2013). On policy-relevant timescales this may be sufficient to qualify as tipping behaviour despite the lack of bistability as there is an abrupt change in ice cover and the system exhibits quasi-hysteretic behaviour. This highlights a weakness of detecting saddle-node bifurcations by following the system's transient response to changing CO_2 concentrations as quasi-hysteretic behaviour can appear if the system doesn't have sufficient time to relax to its equilibrium state.

Some experiments with simplified GCMs have exhibited multistability in sea ice cover. Using an atmosphere-only GCM without seasonality or continents Langen and Alexeev (2004) find 3 stable states analogous to the classic EBM states in Budyko (1969) and Sellers (1969) controlled by the size of surface ocean heat flux convergence. Using a fully coupled ice-atmosphere-ocean GCM with low spatial resolution and simplified atmospheric physics and ocean geometries, Ferreira, Marshall and Rose (2011) found 3 stable ice-cover states, corresponding to a snowball state, an ice-free state, and a state with an ice cap extending into the mid-latitudes (much lower than the classic SICI case).

3 Bridging the gap between models

It is clear from existing literature that there is a gap between a majority of GCMs which simulate a smooth loss of Arctic sea ice under projected CO_2 emission pathways, and simpler bistable models and a subset of GCMs which show tipping and quasi-tipping behaviour. Potential causes for this disparity are the absence or

oversimplification of key processes within simpler models, or misrepresentation of processes within GCMs.

The complexity of GCMs makes it a very difficult problem to understand what processes are responsible for this difference in model behaviour.

My aim in this thesis is to improve the understanding of this discrepancy using a 'bottom-up' approach of adding complexity to a simple climate model (the sea ice model used in EW09) to examine how additional climate features affect the stability of the sea ice system. The flexibility and computational cheapness of this more process-oriented approach that simple models allow make it easier to give a clear picture of how individual climate features affect the bifurcation structure of Arctic sea ice. However, it is more difficult to identify the importance of interactions between processes using where climate features are individually added and removed from a model.

The approach of adding complexity to simple sea ice models has been used previously to demonstrate significant changes to the system's bifurcation structure (Abbot, Silber and Pierrehumbert, 2011; Moon and Wettlaufer, 2012; Wagner and Eisenman, 2015b). A drawback of this approach is the wide range of processes not represented in simple models make it difficult to make predictive statements about the Arctic in reality. Each model configuration should instead be thought of as a highly simplified version of reality that allows us to understand how different features affect the behaviour of the Arctic's climate in reality rather than a mirror of the behaviour of the real world.

Following a range of intermediate complexity models (e.g. Abbot et al., 2011; Toppaladoddi & Wettlaufer, 2015) I use the sea ice model from Eisenman and

Wettlaufer (2009) (henceforth referred to as EW09) as the base model for my approach. In the next subsection I provide a detailed overview of this model.

3.1 The EW09 ice model

The EW09 model treats the Arctic as a spatially uniform domain with the surface either represented by a slab mixed layer ocean with temperature T_{ml} or a slab layer of sea ice with variable thickness h. The state of the surface is described using the scalar energy density coordinate, E, representing the energy stored in the Arctic as latent heat in ice (when ice-covered) and sensible heat in the mixed layer (when ice-free):

$$E = \begin{cases} -\rho_i L_i h & E < 0 \text{ (ice-covered)} \\ c_{ml} H_{ml} T_{ml} & E \geq 0 \text{ (ice-free)} \end{cases} \quad (1)$$

where ρ_i and L_i are the density and latent heat of fusion of ice; c_{ml} and H_{ml} are the specific heat capacity and depth of the ocean mixed layer. The mixed layer temperature, T_{ml} is defined as the temperature difference from the freezing point of ice, T_{fr}, such that the state $E = 0$ represents the point when the mixed layer is at the freezing point of water with no sea ice cover.

The state-dependent albedo, α, is parameterised using a tanh function:

$$\alpha(E) = \frac{\alpha_{ml} + \alpha_i}{2} + \frac{\alpha_{ml} - \alpha_i}{2} \tanh\left(\frac{E}{E_\alpha}\right) \quad (2)$$

where α_{ml} and α_i are the limiting cases of low and high albedo for open water and thick ice respectively; E_α is the characteristic energy density scale over which the albedo transition occurs. Eisenman and Wettlaufer (2009) justify this formulation as it approximates the gradual melt of sea ice in the Arctic as it approaches an ice-free state. The abrupt decrease in albedo in the tanh formulation also reflects the much weaker albedo of thin ice compared to thick ice.

When ice-covered, the thermodynamic evolution of the ice pack is simulated using a simplification of the model presented in Maykut and Untersteiner (1971), by considering fluxes at the top and bottom surfaces of the ice pack and the internal heat flux (Figure 4). Numerical models like that presented in Maykut and Untersteiner (1971) were a significant progression from classical work that began with Stefan (1891) which were limited to studying cases with analytical solutions.

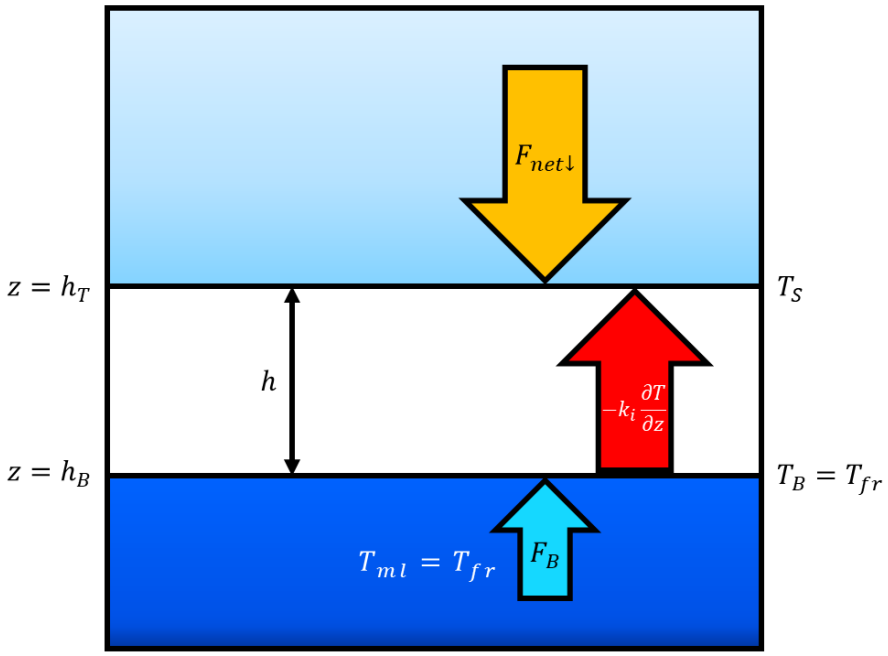


Figure 4 Schematic diagram of the ice-covered state of the EW09 model. The thermodynamic growth rate of ice is calculated by considering the balance between ablation at the ice top surface, $z = h_T$, and ablation/growth at the bottom surface, $z = h_B$. Top surface ablation is calculated from the balance between the net downward atmospheric flux, $F_{net\downarrow}$ and the internal heat flux $-k_i \frac{\partial T}{\partial z}$ when the surface temperature T_S is at the freezing point of water T_{fr}, otherwise it is set to zero. Growth/ablation at the bottom surface is calculated from the balance between the internal heat flux and the bottom surface heat flux, F_B. The ice top surface temperature, T_S, is calculated from a balance of fluxes at the ice-atmosphere interface when T_S would be below T_{fr}, otherwise it is kept pinned at T_{fr}. The ice bottom surface is assumed to be in thermal equilibrium with the mixed layer ocean which is kept at T_{fr} while ice is present.

When the upper surface of ice is below the freezing temperature, the fluxes at the ice-atmosphere interface are balanced, otherwise the surface temperature is held at the freezing point and a Stefan condition for surface ablation is applied:

$$F_{net\downarrow} - k_i \left(\frac{\partial T}{\partial z}\right)_{h_T} = \begin{cases} 0 & T < T_{fr} \\ -\rho_i L_i \dfrac{dh_T}{dt} & T = T_{fr} \end{cases} \quad (3)$$

where $F_{net\downarrow}$ is the net total of radiative and surface heat fluxes at the ice surface defined as positive downwards; k_i is the thermal conductivity of sea ice, assumed to be constant; z is the vertical position coordinate and h_T is the position of the ice top surface.

The ice bottom surface is assumed to always be in thermal equilibrium with the ocean mixed layer, with both fixed at the freezing temperature of water while ice is present. In all situations a Stefan condition for growth or ablation is applied:

$$k_i \left(\frac{\partial T}{\partial z}\right)_{h_B} + F_B = \rho_i L_i \frac{dh_B}{dt} \quad (4)$$

where h_B is the position of the ice bottom surface; and F_B is the heat flux from the ocean into the ice bottom surface.

The rate of change of the ice pack thickness, $h = h_T - h_B$, is therefore generally:

$$\frac{dh}{dt} = \begin{cases} -\dfrac{1}{\rho_i L_i}\left(k_i \left(\dfrac{\partial T}{\partial z}\right)_{h_B} + F_B\right) & T < T_{fr} \\ -\dfrac{1}{\rho_i L_i}\left(F_{net\downarrow} + F_B - k_i \left(\dfrac{\partial T}{\partial z}\right)_{h_T} + k_i \left(\dfrac{\partial T}{\partial z}\right)_{h_B}\right) & T = T_{fr} \end{cases} \quad (5)$$

Finally, the assumption is made that due to the large Stefan number (the ratio of latent heat to specific heat) of the ice pack, its internal temperature instantaneously relaxes to a linear profile following changes to temperature fluxes and ice thickness. This allows (5) to be re-written as:

$$\frac{dh}{dt} = -\frac{1}{\rho_i L_i}(F_{net\downarrow} + F_B) \quad (6)$$

which means that all net energy input into the ice pack from fluxes at the top and bottom surface is converted into a change in ice volume.

Combined with the simple energy evolution of the mixed layer ocean when ice-free this gives the time evolution of the energy density coordinate E for all conditions as:

$$\frac{dE}{dt} = F_{net\downarrow} + F_B + \nu_0 \mathcal{R}(-E) \tag{7}$$

where the final term on the right-hand side is an export term for sea ice. ν_0 is the fractional export rate of ice from the Arctic and $\mathcal{R}(x)$ is a ramp function such that the term only applies when the Arctic is ice-covered.

The final aspect of the EW09 model is the calculation of surface temperature which is necessary for the calculation of upwelling longwave radiation at the surface. When the surface temperature would be below the freezing point it is simply calculated from the balance of fluxes at the ice-atmosphere interface. When ice is present and the surface temperature would be above T_{fr} the surface temperature is kept pinned at T_{fr} while surface ablation takes place. When the system is ice-free the surface temperature is directly proportional to the coordinate E, $T = E/(c_{ml}H_{ml})$.

Unless stated otherwise I use the parameter values given in Table 1:

Parameter	Value
ρ_i	$917\ kgm^{-3}$
L_i	$333.4\ kJkg^{-1}$
c_{ml}	$4\ MJm^{-3}K^{-1}$
H_{ml}	$50\ m$
α_{ml}	0.2
α_i	0.68

E_α	$0.205\ MJm^{-2}$
k_i	$2.2\ Wm^{-2}K^{-1}$
F_B	$2\ Wm^{-2}$
ν_0	$10\%\ \text{year}^{-1}$

Table 1 Default parameter values for the EW09 ice model.

While this model has the advantage of simply capturing the evolution of Arctic sea ice it misses out a wide range of important features, including:

Simplifications within the ice pack

- Melt ponds and snow cover at the ice surface would impact the surface albedo and the boundary conditions for surface temperature and ablation.
- Deviations from a linear temperature profile within the ice pack would affect the thermodynamic growth rate of ice and increase ice sensitivity to forcing at the bottom surface.
- Shortwave absorption within the ice pack would modify the temperature profile within the ice pack which is unresolved in EW09.
- Variations in ice cover across the Arctic, including fractional ice cover and variation in mixed layer temperature smooth out the evolution of the mean surface albedo and would affect the overall surface energy budget – within this variable ice cover mechanical processes also affect the evolution of local ice thickness.

Simplifications outside the ice pack

- In their paper, Eisenman and Wettlaufer (2009) used prescribed seasonal cycles of surface fluxes and therefore didn't allow for feedbacks affecting these as the Arctic's state changes.

- Changes in the Arctic lapse rate, atmospheric humidity and cloud radiative effects would affect the balance of fluxes at the ice surface.
- Changes in atmospheric heat transport driven by changes in global circulation would affect radiative and surface heat fluxes at the ice surface.
- Changes to ocean heat flux convergence and energy fluxes into open water would affect the bottom heat flux, F_B.

4 Structure of the thesis

In this thesis I aim to address the effect of some of these missing features on the bifurcation structure of the Arctic sea ice system from the base state of this model (Figure 3, (right)). The three areas I address are:

1. Variations in Arctic ice cover
2. Local ice-atmosphere feedbacks
3. The role of atmospheric heat transport

In chapter 2 I discuss the use of the ice thickness distribution to explore the effect of variable ice-cover on the bifurcation structure of the Arctic. I give an overview of the theory of the ice thickness distribution and demonstrate the suitability of two different parameterisations of mechanical interactions within the ice pack for this work. Finally, I present results showing the effect of mechanical interactions on the bifurcation structure of the system using one of these parameterisations.

To address the role of ice-atmosphere feedbacks and atmospheric heat transport I couple a sea ice model to a single column model of the Arctic atmosphere. In chapter 3 I give a broad overview of some key features of the climate of the Arctic atmosphere, discuss the construction of my column model and compare it to reanalysis and observations.

In chapter 4 I use the single column model to investigate the effect of local atmospheric processes on the stability structure of Arctic sea ice. I present results exploring the impact of vertical temperature structure, clouds and atmospheric forcing structure on the system's bifurcation structure.

In chapter 5 I introduce simple representations of atmospheric heat transport to the model to investigate how changes in heat transport affect the system's bifurcation structure, including exploring the sensitivity to the strength of these feedbacks.

In chapter 6 I present overall conclusions from my work and present ideas for further research.

Chapter 2 The sea ice thickness distribution

1 Introduction

Slab sea ice models like EW09 discussed in the previous chapter do not allow for any spatial variation in the ice cover to be represented at a given timestep. In reality a given area of sea ice cover often includes open water, thin recently formed ice, and thick multi-year ice and pressure ridges concurrently, with large variations in thickness seen over length scales of $\sim 100\ m$ (Eicken and Lange, 1989).

Many properties of sea ice are thickness-dependent, including: surface temperature, albedo and compressive strength. This thickness dependence means that thin and thick ice evolve differently over time, e.g. thin ice grows much faster than thick ice and is more likely to deform in mechanical processes. Slab ice models only represent one thickness so cannot accurately represent the distribution of these ice properties (that typically vary non-linearly with thickness) in the ice pack or the concurrent evolution of thin and thick ice. Moreover, the EW09 model cannot represent a partially ice-covered Arctic, only letting it be completely ice-covered or completely ice-free. Differences in albedo, surface temperature and heat fluxes mean that energy exchange over open water is very different to over ice and changes to the open water fraction significantly alter the overall surface energy budget of the Arctic. It is therefore more accurate to represent the variation in surface cover in the Arctic than to use a single aggregate thickness as in EW09.

In this chapter I discuss how the ice thickness distribution, as introduced in Thorndike *et al.* (1975), can be used to resolve these features in a relatively simple model. In section 2 I give an overview of the theory of the ice thickness distribution. In section 3 I outline how I model its time evolution. In section 4 I detail two parameterisations of the mechanical redistribution term (Fokker-Planck and coagulation schemes) and present results using each. In section 5 I present conclusions of this work and suggest possibilities for further work.

1.1 Statement of work

The Fokker-Planck formulation of ice mechanics as outlined in section 4.1, including the extension to allow for the formation of open water, is derived from Toppaladoddi and Wettlaufer (2015, 2017) and Toppaladoddi, Moon and Wettlaufer (2023). All analysis of this work is my own.

2 The ice thickness distribution

Thorndike *et al.* (1975) propose an elegant way of representing variable ice cover without the need for spatial resolution using the ice thickness distribution, $g(h)$.

For a region, R, large enough to contain a range of different ice thicknesses $g(h)$ is a probability distribution function such that the integral of g over a given thickness interval, (h_1, h_2) is the probability, $P(h_1, h_2)$, that a randomly selected point in the region is covered by ice within that thickness interval i.e.

$$\int_{h_0}^{h_1} g(h)dh = P(h_1, h_2) \tag{8}$$

$P(h_1, h_2)$ can alternatively be interpreted as the area fraction within the region with ice cover in the thickness interval (h_1, h_2). Figure 5 shows an example of a sea ice thickness distribution for the inner Arctic derived from satellite observations.

A note on normalisation: Throughout this chapter I will use the convention that g only describes the *ice-covered* parts of R. I define the area fraction of the *ice-free* parts of R as the open water fraction, A. To ensure conservation of probability, the following criteria must always be satisfied:

$$\int_0^\infty g(h)dh + A = 1 \tag{9}$$

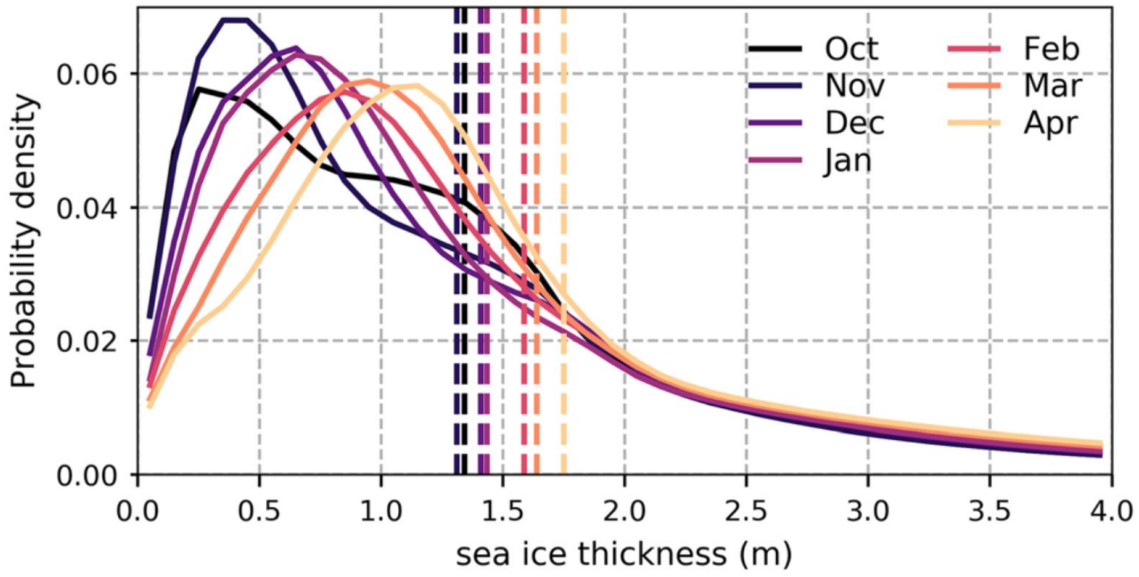


Figure 5 Sea ice thickness distributions for October through April covering the Central Arctic, Beaufort Sea, Chukchi Sea, East Siberian Sea and Laptev Sea. Thickness distributions are derived from ICESat-2 freeboard measurements and a model for snow thickness. Dashed lines indicate the monthly mean thickness for each month. Taken from Petty et al. *(2020). The thickness distributions have a characteristic single-peaked shape (peaking here between* 0.5 *and* 1.5 m *with an approximately exponentially decaying tail of thick ice.*

The evolution of g can be described by the following partial differential equation (Thorndike *et al.*, 1975) which is discussed in more detail in section 3:

$$\frac{\partial g}{\partial t} = -\frac{\partial}{\partial h}(fg) - \nabla \cdot (\boldsymbol{u}g) + \psi \tag{10}$$

where f is the thermodynamic growth rate of ice, $\boldsymbol{u}$ is the velocity field of the ice pack, and ψ is a redistribution function representing changes to g due to mechanical processes in the ice pack.

Modelling the ice thickness distribution is of interest for the existence of multistable states in the Arctic as the resolution of a range of ice thicknesses and open water alters non-linearities in the model system. In GCM simulations using a low resolution ice thickness distribution model (with 5 thickness categories and an open water category) Holland *et al.* (2006) find that the resolution of a tail of thin ice and a non-zero open water fraction lowers the albedo for a given mean thickness – this effectively smooths out the relationship between albedo and domain mean ice thickness, potentially disrupting bistability in the system. Holland *et al.* (2006) also find that resolving the low thickness tail allows for a region of fast-growing thin ice to exist for all mean thicknesses. This provides a stabilising effect on ice cover and may increase the stability of an ice-covered branch in a bistable system.

Moreover, it is of interest to see how the behaviour of the system changes when the model-state is changed from a single variable, E, to a continuous function, g, for the ice-covered state.

In the next section I discuss the time-evolution of the ice-thickness distribution in detail.

3 Modelling the ice thickness distribution

3.1 The time-evolution equation

The time evolution of g is described by (10). The terms on the right-hand side represent respectively:

1. The thermodynamic growth of ice, described by the growth rate f.
2. Advection of the ice pack, described by the ice pack velocity field $\boldsymbol{u}$.
3. Mechanical redistribution of the ice pack, described by a redistribution function ψ.

I will discuss each of these terms in more detail below.

3.2 The thermodynamic term

Along with advection of ice into and out of the system, thermodynamic growth is one of the mechanisms by which the mean thickness of ice in the system can change. It is represented by a growth rate $f(h)$ that acts to shift $g(h)$ in thickness space.

Throughout this chapter I calculate $f(h)$ for a given thickness using the simplified thermodynamic model used in EW09 (see chapter 1) from net energy input at the top and bottom surfaces of the ice pack:

$$f(h) = -\frac{1}{\rho_i L_i}(F_{net\downarrow}(h) + F_B) \tag{11}$$

where $F_{net\downarrow}(h)$ is the net energy flux at the top surface of the ice pack and F_B is the ocean heat flux at the ice bottom surface.

As I use the convention that $g(h)$ only describes the ice-covered regions of R, this means that (10) doesn't account for the energy fluxes over the ice-free parts of the model domain. It is therefore necessary to include additional terms, formulated as part of my own work, to account for the energy budget over open water.

3.2.1 Treatment of open water

The model can exist in one of three cases:

1. Completely ice-covered, $A = 0$.
2. Completely ice-free, $A = 1$.
3. Partially ice-covered, $0 < A < 1$.

In cases 2 and 3 there is energy flux into the system through the open water fraction that must be accounted for (Figure 6).

For case 2, when the system is *completely ice-free* I treat the mixed layer surface as a slab ocean with uniform temperature T_{ml} and fixed heat capacity and depth c_{ml} and H_{ml} (identically to EW09). When the ocean is ice-free and would cool below the freezing point of water I keep the temperature fixed there and convert the excess energy deficit into latent heat in a newly formed ice layer. For the sake of simplicity, I assume that the entire open water fraction freezes over uniformly. I approximate a uniformly thick ice thickness distribution using a Gaussian with mean thickness, h_f, and standard deviation, $h_f/6$, such that the newly formed ice has equal energy to the energy deficit and covers the whole model domain. This is roughly equivalent to the treatment of open water freeze-up in EW09 where the model state instantaneously becomes fully ice-covered and qualitatively agrees with observations of a secondary peak of young ice in the Arctic winter (Eicken and Lange, 1989). Following this step, the ocean ceases to be ice-free and so this is only done for one time step. Toppaladoddi, Moon and Wettlaufer (2023) similarly assume open water instantaneously freezes over when the open water flux becomes negative, however they do not include the delta spike like term I use to represent the newly formed thin ice layer.

When the system is *partially ice-covered* and the net energy flux into open water is *positive* I convert this into an additional heat flux at the ice bottom surface, essentially assuming instantaneous conversion of energy storage to a bottom heat flux. This follows previous work suggesting that energy input into open water contributes to the heat flux at the bottom surface (Maykut and McPhee, 1995; Perovich *et al.*, 2008). The assumption that 100% of the open water flux is converted into bottom melt is a simplification and doesn't account for contributions to lateral melt of ice, heat storage within the mixed layer, or heat lost to the deeper ocean. For example, Horvat, Tziperman and Campin (2016) find that lateral mixing of warm

water near ice floe edges enhances basal melt near floe boundaries – effectively increasing lateral melt of the ice floes.

When the system would be *partially ice-covered* and the net energy flux into open water is *negative* I convert this negative flux into latent heat in a newly formed ice layer in the same manner as discussed above for the completely ice-free case. The newly formed ice layer has mean thickness h_f and standard deviation $h_f/6$, such that it has equal energy to the energy deficit and covers the whole region of open water. This means that when the net energy flux over open water is negative and the mixed layer temperature is at the freezing point of water the system must be completely ice-covered.

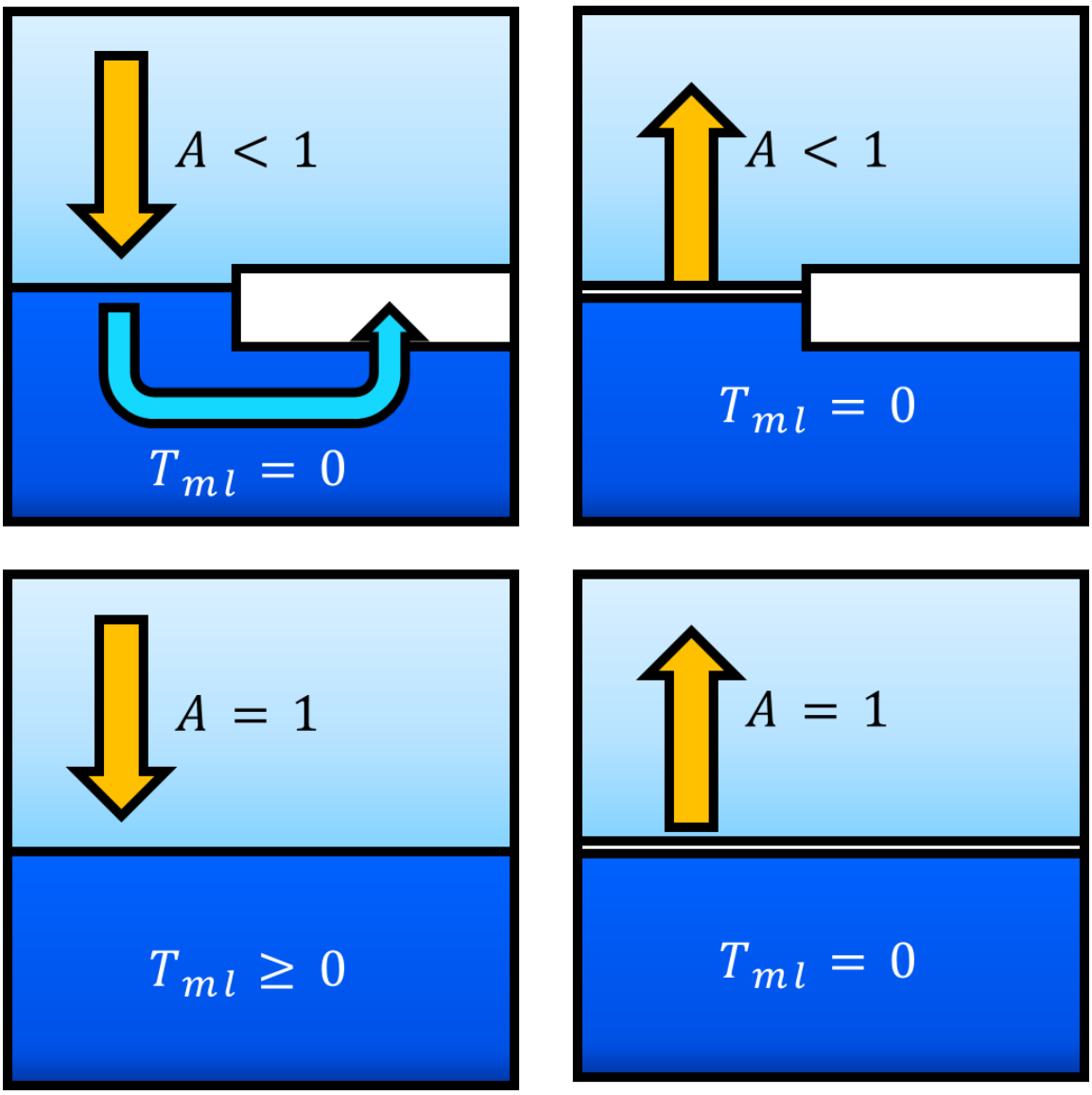


Figure 6 Schematic showing the treatment of open water flux (orange arrow) in the ice thickness distribution model. When the system is partially ice-covered ($A < 1$) and there is a positive flux into open water (top left) the open water flux is converted into an additional bottom heat flux (blue arrow). When the system is partially ice-covered ($A < 1$) and there is a negative heat flux into open water (top right) the open water region instantaneously freezes over in a Gaussian thickness distribution. When the system is ice-free ($A = 1$) the mixed layer ocean evolves as a slab layer with heat capacity and thickness, c_{ml} and H_{ml}, (bottom left). When the system is ice-free ($A = 1$) and the open water flux would make the mixed layer ocean cool below the freezing point of water (bottom right) the mixed layer cools to the freezing point and the excess energy deficit is converted into a thin layer of ice covering the whole model domain.

3.3 The advection term

The second term on the right-hand side of (10) represents the advection of the ice pack, described by its velocity field $\boldsymbol{u}$. As my model doesn't resolve horizontal

dimensions I don't explicitly include this term. Similar to EW09 I include an ice export term, $\frac{\partial g}{\partial t}\Big|_{export} = -\nu_0 g$, where ν_0 represents the rate of ice exported out of the Arctic region with a corresponding open water source term, $\frac{dA}{dt} = \nu_0 \int_0^\infty g dh$. Like EW09 I use a constant value of $10\%\ \mathrm{year}^{-1}$. This applies the simplification that the fractional export rate does not vary with time or open water fraction, and that ice of all thickness is exported at the same rate.

3.4 The redistribution term

The third term in the right-hand side of (10) represents the effect of mechanical processes within the ice pack. On aggregate these processes act to redistribute thickness in the domain, converting thinner ice into thicker ice and creating open water. On the individual floe scale these consist of rafting and ridging processes where ice floes ride over one another and destructively collide into one another respectively (Vella and Wettlaufer, 2008). There is no simple mathematical closure that captures the range of mechanical processes sea ice undergoes and the accurate representation of these effects has been the principle difficulty in proceeding to a complete representation of the ice thickness distribution.

Under the assumption that mechanical processes cannot create ice or destroy ice, only rearrange its distribution in the domain, ψ is subject to the constraint:

$$\int_0^\infty h\psi dh = 0 \qquad (12)$$

Later in this chapter I evaluate whether this constraint is satisfied for the Fokker-Planck mechanics parameterisation.

As mechanical processes needn't conserve the open water fraction of the domain. ψ can change the area under the curve using my formulation of g. This is in contrast

to other formulations (e.g. Thorndike *et al.*, 1975) where ψ must additionally be constrained to conserve this quantity.

Creating a simple but accurate formulation of ψ is one of the chief difficulties in modelling the ice thickness distribution. In their original paper Thorndike *et al.* (1975) present a formulation of ψ by considering divergent and convergent modes of ice motion independently, however it required information on the strain rate of the ice pack and unconstrained functions to be specified. Further work has attempted to build up a closed form of ψ by considering redistribution as a sum of simplified coagulation processes (Thorndike, 2000; Godlovitch, Illner and Monahan, 2011) and by using observations to tune a Fokker-Planck model of mechanical processes (Toppaladoddi and Wettlaufer, 2015, 2017).

In the following section I will discuss these two parameterisations of ψ in more detail.

4 Mechanics parameterisations

4.1 Fokker-Planck parameterisation

Toppaladoddi and Wettlaufer (2015, 2017) propose a parameterisation of mechanical processes that considers mechanical processes as stochastic events with a probability of altering a floe's position in *thickness space*. Their key insight is noting the separation of length and time scales of mechanical processes relative to the evolution of g. Mechanical processes typically occur on length scales of $\sim 10\ m$ and domains with length scales of $\sim 100\ km$ are needed to define g. They argue that this separation of scale means that so many mechanical processes take place during the of evolution of g that ψ doesn't need to resolve individual collisions, only their aggregate effect on the distribution. To this end they write ψ as:

$$\psi = \int_0^\infty [g(h')w(h,h') - g(h)w(h',h)]dh' \quad (13)$$

where $w(h,h')$ and $w(h',h)$ represent the transition probabilities of floes of thicknesses h' and h being displaced by a mechanical process to thickness h and h' respectively. The left-hand term of the integral represents the sum effect of all mechanical processes creating floes of thickness h and the right hand term is a sink term representing the sum effect of all mechanical processes converting floes of thickness h to another thickness.

Assuming that $w(h,h') = w(h',h)$, (13) can be expanded, giving:

$$\psi = \int_0^\infty \left[w(h,h') \left(\frac{\partial g}{\partial h}(h'-h) + \frac{\partial^2 g}{\partial h^2}\frac{(h'-h)^2}{2} + \mathcal{O}((h'-h)^3) \right) \right] dh' \quad (14)$$

Taking the first and second order terms gives:

$$\psi = k_1(h)\frac{\partial g}{\partial h} + k_2(h)\frac{\partial^2 g}{\partial h^2} \quad (15)$$

where:

$$k_1(h) = \int_0^\infty [(h'-h)w(h,h')]dh' \,; k_2(h) = \int_0^\infty \left[\frac{(h'-h)^2}{2} w(h,h') \right] dh' \quad (16)$$

This lets (10) (in the absence of an advection term) be written in the form of a Fokker-Planck equation:

$$\frac{\partial g}{\partial t} = \frac{\partial}{\partial h}\big((k_1 - f)g\big) + \frac{\partial^2}{\partial h^2}(k_2 g) \quad (17)$$

Here all information about mechanical processes is included in the parameters k_1 and k_2. These are statistical parameters and are not straightforward to derive from physical principles. Toppaladoddi and Wettlaufer (2015) assume that k_1 and k_2 are constants and choose values by calculating an expression for the steady state ice thickness distribution in winter and tuning these parameters to fit ICESat

observations, giving $k_1 = 7.2 \cdot 10^{-8}\, ms^{-1}$ and $k_2 = 5.6 \cdot 10^{-8}\, m^2 s^{-1}$ (values cited here are different due to non-dimensionalisation in Toppaladoddi and Wettlaufer (2015)). Unless stated otherwise, I use these constant values in this chapter.

4.1.1 Seasonal evolution and open water

Toppaladoddi and Wettlaufer (2017) explore the evolution of the system using prescribed annual cycles of surface fluxes taken from Maykut and Untersteiner (1971). However, they do not allow for the formation of open water in their model and renormalize g at each timestep to ensure conservation of ice volume.

Following Toppaladoddi, Moon and Wettlaufer (2023) the model can be extended to allow for the formation of open water by accounting for the probability flux, J, across the $h = 0$ boundary. The rate of change of the open water fraction, A, can be found by considering rate of change of probability, by differentiating (9):

$$\frac{dA}{dt} = -J|_{h=0} = \left((k_1 - f)g + \frac{\partial}{\partial h}(k_2 g) \right)\Bigg|_{h=0} \tag{18}$$

This can then be used to specify a boundary condition at $h = 0$ by assuming the closure $A = H_c g|_{h=0}$, where H_c is a constant that can be interpreted as the cut-off thickness at which ice and open water become indistinguishable (set at $10\, cm$ unless stated otherwise). Giving the boundary condition:

$$\frac{dg|_{h=0}}{dt} = \frac{1}{H_c}\left((k_1 - f)g + \frac{\partial}{\partial h}(k_2 g) \right)\Bigg|_{h=0} \tag{19}$$

As this boundary condition is derived from the statement of probability conservation there is no longer a need to renormalise the distribution at each timestep. This boundary condition is only applied when the net open water flux is positive and open water formation is expected. When the net open water flux is negative the ice-free

region completely freezes over as discussed in section 3.2.1 and the boundary condition is set such that $g(h = 0) = 0$.

The far-field boundary condition is set such that $g \to 0$ as $h \to \infty$.

4.1.2 Conservation of thickness

Here I present some steady seasonal cycles of the model as outlined above using the Fokker-Planck parameterisation. The seasonal cycle of f was calculated using the same prescribed forcing cycles, albedo parameterisation and linearised Stefan-Boltzmann law as in EW09. Equation (17) was solved using a fully implicit scheme with first and second order centred differences for the advection and diffusion terms respectively. In each case the net surface energy flux, $F_{net\downarrow}$, includes an additional downward perturbation, ΔF_0. In each case the distribution was initiated at the beginning of the 1st of January using the steady state winter distribution given in

Toppaladoddi and Wettlaufer (2015). The model was run with a timestep of 1 hour, a thickness interval of 10 cm and a maximum thickness of 10 m.

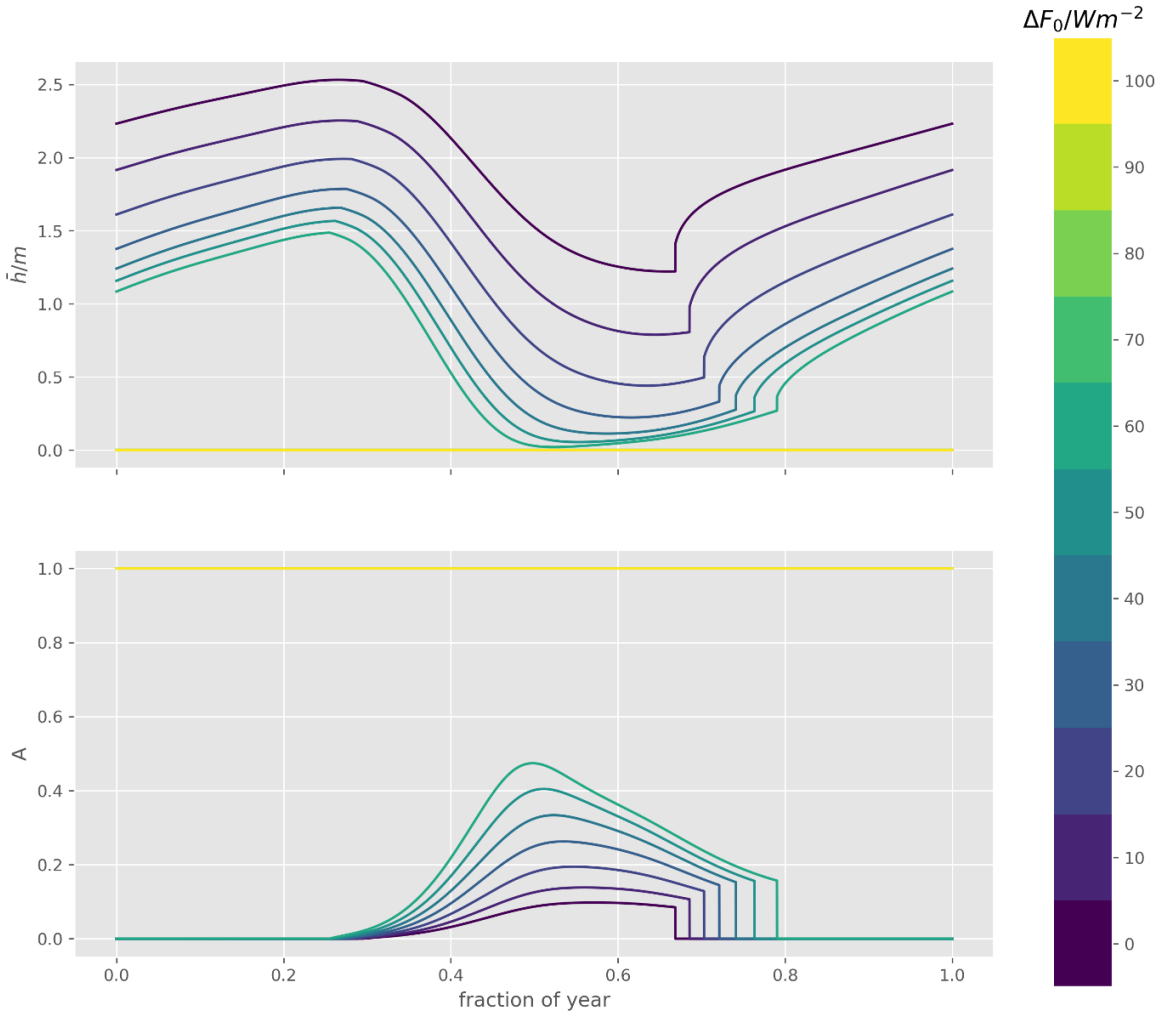


Figure 7 Steady state seasonal cycles of the ice thickness distribution using the seasonal cycles of forcing, albedo parameterisation and linearised Stefan-Boltzmann equation from EW09 and ice mechanics represented by the Fokker-Planck parameterisation using constant $k_1 = 7.2 \cdot 10^{-8}$ and $k_2 = 5.6 \cdot 10^{-8}$. In each model run the surface forcing was perturbed by a constant value ΔF_0 (shown in colorbar). Top plot shows the steady state seasonal cycles of the domain mean thickness, $\bar{h}$. Bottom plot shows the steady state seasonal cycles of the open water fraction, A.

Figure 7 shows steady state seasonal cycles of the domain mean ice thickness, $\bar{h}$, and open water fraction, A, for ΔF_0 values from $0 - 100 Wm^{-2}$.

It is immediately apparent that the model shows an unrealistic kink in the mean ice thickness when open water freezes over. As discussed earlier, the model

instantaneously freezes all open water when the net surface energy flux over open water becomes negative. This means that at this point the open water fraction instantaneously decreases to 0. It also leads to a coincidental sharp increase in the rate of change of $\bar{h}$ as the newly formed region of thin ice grows much faster than the rest of the ice pack leading to the kink seen in the evolution of the mean thickness. (There is also a small discontinuous increase in $\bar{h}$ introduced at the moment of open water freeze-up due to renormalisation of g to ensure probability is conserved. This inflate the size of the kink beyond what would be seen purely from the freeze-up of open water). This differs from observations and stems from the uniform treatment of the mixed layer. The model could be modified to fit observations better by parameterising gradual freeze-up of open water.

Equally unusual is the stability of the ice cover to extremely high radiative forcing perturbations in this model configuration. Strikingly, the system is modelled as being in a perennially ice-covered state for surface forcing perturbations up to and including $60\ Wm^{-2}$ – over twice the size of the perturbation to make a similar model without a thickness distribution perennially ice-free (Eisenman and Wettlaufer, 2009). Moreover, the sensitivity of $\bar{h}$ to increased surface forcing *decreases* as the ice cover thins. This is the opposite of what would be expected from the sharp decrease in albedo as the ice cover thins and open water fraction increases. It is possible that the thickness distribution's resolution of a tail of fast-growing thin ice helps stabilise the system for greater forcing perturbations, but this level of stabilisation wouldn't be expected (note that switching off the growth rate feedback in Eisenman and Wettlaufer (2009) resulted in a smaller change in the position of the bifurcation point than is seen here).

The persistence of the ice cover can be explained by considering the time evolution of $\bar{h}$. As discussed previously, mechanical processes cannot create or destroy ice, only redistribute it, so ψ must satisfy (12). Testing for this using the Fokker-Planck parameterisation yields the expression:

$$\int_0^\infty h\psi dh = (k_2 g)|_{h=0} - \int_0^\infty k_1 g \, dh \tag{20}$$

For constant k_1 and k_2 this reduces (using the closure $A = H_c g|_{h=0}$) to:

$$\int_0^\infty h\psi dh = k_2 \frac{A}{H_c} - k_1(1 - A) \tag{21}$$

From here it is clear that (12) is satisfied only when $A = \frac{k_1}{k_1 + k_2/H_c}$, in all other model states ice volume is not conserved by this mechanics parameterisation and (21) represents a systematic error term in the evolution of $\bar{h}$ and by extension g. The first term on the right-hand side represents a source of ice volume and the second term a sink. Even with $A = 0$ the Fokker-Planck parameterisation implies a systematic decrease of $\bar{h}$ without a clear physical justification.

Figure 8 plots the value of this term for the same seasonal cycle data as in Figure 7. It can be seen here that for low ΔF_0 the sink term dominates compared to the source and the mechanics parameterisation leads to an underestimation of $\bar{h}$ and as ΔF_0 increases the source term dominates due to changes in open water fraction leading to an overestimation of $\bar{h}$. For large ΔF_0 values, as A reaches large values in the summer melt season the large source term stabilises the thin ice cover and prevents the system from becoming ice-free. Only in the simulations where $\Delta F_0 > 60 W m^{-2}$ are the thermodynamic effects large enough to outweigh this additional term and push the system into an ice-free state.

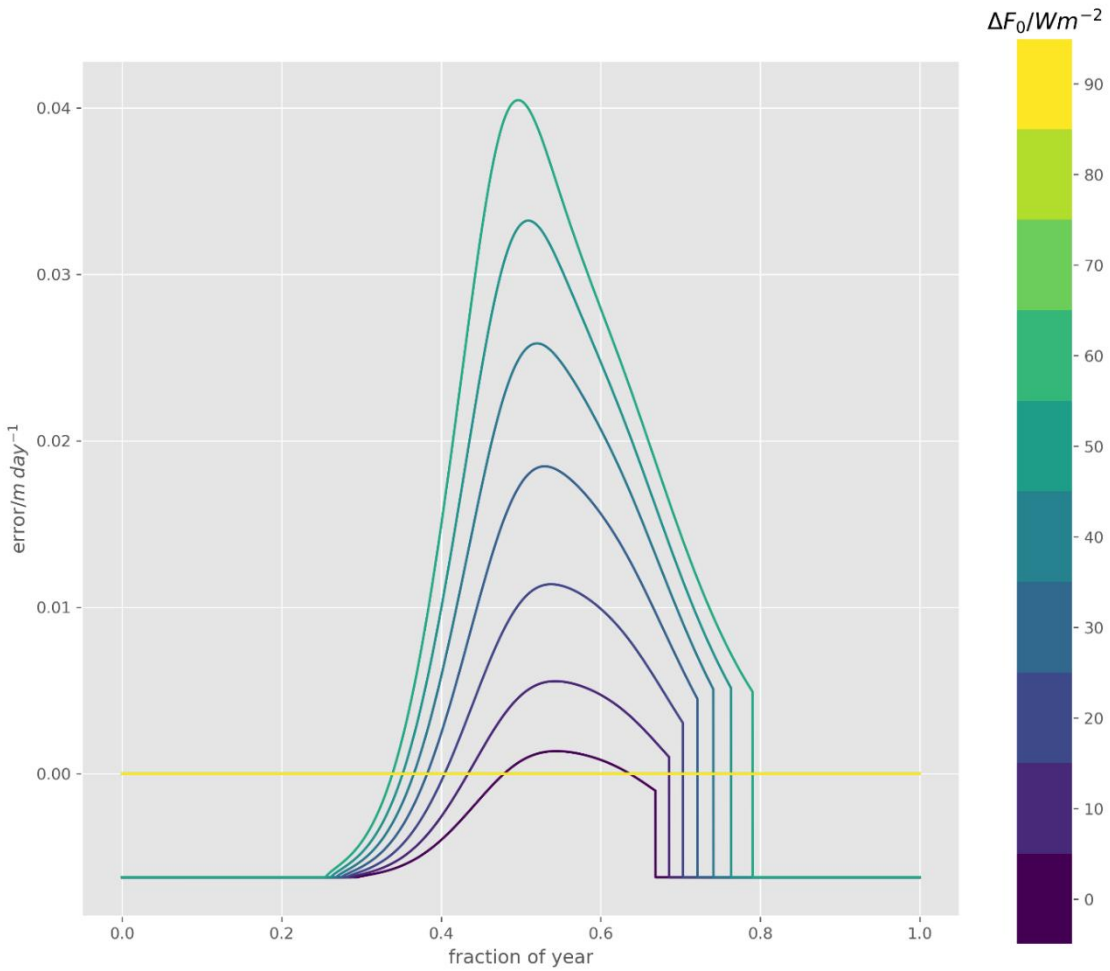


Figure 8 Steady state seasonal cycles of the change in mean thickness due to the redistribution function, ψ, for the same simulations as in Figure 7.

Equation (20) can be interpreted by considering the physical significance of the constants k_1 and k_2 as first and second moments of the transition probability function $w(h, h')$. k_1 therefore, represents the mean thickness change an ice floe undergoes in a mechanical process and k_2 is a measure of the variance of the thickness change. With constant k_1 and k_2 ψ can be interpreted as a uniform advection in thickness space, with advective velocity k_1, superimposed with a diffusive term with diffusivity k_2 to spread out g. The source and sink terms in (20) then simply represent the advective flux across the $h = 0$ boundary and the change in mean thickness as the distribution is truncated at $h = 0$ arising from the choice of constant k_1 and k_2. In this light it is clear that (12) can't be satisfied with constant,

non-zero k_1 and k_2. The necessary constraint on k_1 and k_2 to conserve mean thickness can be calculated as.

$$g(0) = \frac{k_1}{k_2} \int_0^\infty g dh \tag{22}$$

However, choosing appropriate forms of both functions and tuning them to observations is a non-trivial task. In this light I turn my attention to an alternative mechanics parameterisation that will ensure ice-volume conservation.

4.2 Coagulation parameterisation

In this section I will explore an alternative parameterisation of ψ designed to ensure the conservation of energy in the model using the coagulation equation. Formulations of this kind have previously been used by Thorndike (2000) and Godlovitch, Illner and Monahan (2011). Unlike the Fokker-Planck parameterisation, which uses a 'top-down' approach – considering mechanical processes from a statistical perspective – this approach works from the bottom up by considering a class of idealised processes and scaling this up across the entire distribution.

I begin by assuming that each individual mechanical process can be described by the following framework. Consider two segments of ice of equal area and with thicknesses h' and h''. In a single collision event, these two segments combine to create a new segment of equal area and thickness $h' + h''$and a region of open water of equal area (Figure 9). This is analogous to an idealised rafting event.

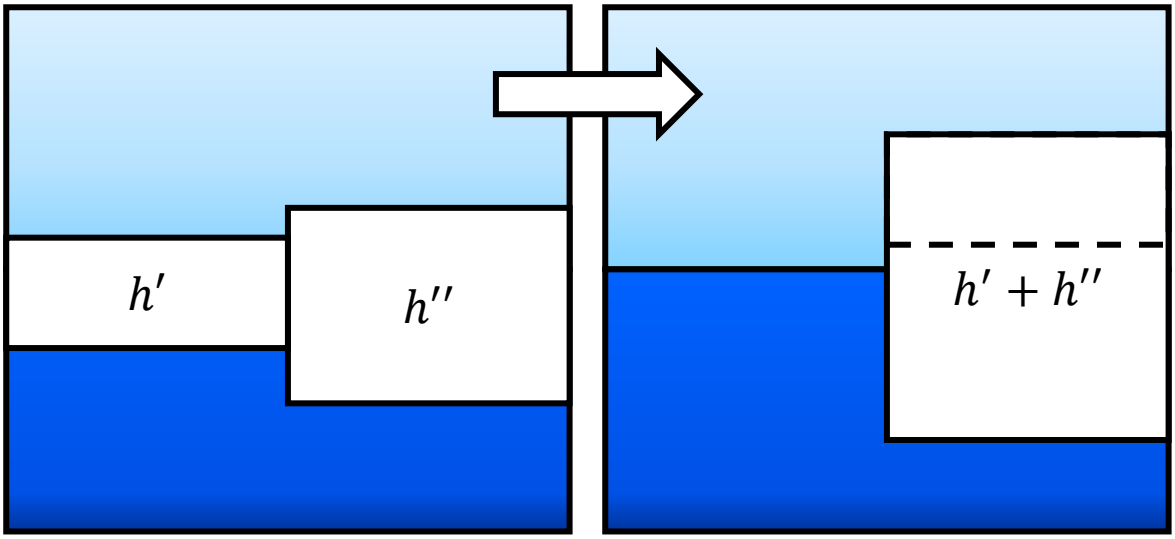


Figure 9 Schematic diagram showing the base process described by the coagulation parameterisation. In a single event 2 segments of equal area and thicknesses h' and h'' combine to form a new segment of thickness $h' + h''$ and a region of open water – each of the same area as the original segments.

The rate of processes of this type for two arbitrary thicknesses can be described by a symmetric coagulation kernel, $K(h', h'')$. The change in g due to coagulation processes is then:

$$\frac{\partial g}{\partial t} = \frac{1}{2}\int_0^h K(h-h', h')g(h-h')g(h')dh' - \int_0^\infty K(h, h')g(h)g(h')dh' \qquad (23)$$

Here the first term on the right-hand side is the mechanical source term for ice segments of thickness h from collisions of two smaller segments (the prefactor of ½ is there to prevent double counting as two parent segments are needed to create a child segment), and the second term is the mechanical sink term from segments of thickness h colliding with any other segment.

Equation (23) describes the aggregate effect of a large number of conservative processes and therefore has the advantage of ensuring the constraint (12) is maintained.

In the following subsection I present steady state seasonal cycles of the sea ice thickness distribution using the coagulation parameterisation with a constant kernel:

$$K(x,y) = r \tag{24}$$

In this case the time evolution of the model reduces to:

$$\frac{\partial g}{\partial t} = -\frac{\partial}{\partial h}(fg) + r\left(-2(1-A)g + \int_0^\infty g(h)g(h-h')dh'\right) \tag{25}$$

$$\frac{dA}{dt} = r(1-A)^2 \tag{26}$$

Equation (25) can be simply derived by substituting (24) into (23). Equation (26) can then be calculated by ensuring that area is conserved in the system.

An additional term for the evolution of A is required to conserve probability.

As r is not easily constrained by observational data I carry out model runs for a range of values from 0 to $10^{-5}\ ms^{-1}$. I use a step-wise process for model evolution, first using a first-order upwind scheme for the thermodynamic growth of ice and then applying the mechanics scheme.

The model is forced identically to the Fokker-Planck simulations above with prescribed forcing, albedo parameterisation and linearised Stefan-Boltzmann law from EW09.

Figure 10 shows the seasonal cycles of the model's mean thickness and ice area fraction for $\Delta F_0 = 0\ Wm^{-2}$ when modelled using the coagulation mechanics parameterisation with $r = 10^{-7}\ ms^{-1}$. There are slight discontinuities in the mean thickness seasonal cycle. One of these coincides with the freeze-up of open water and can be explained by a numerical error due to the probability distribution of newly formed ice (described in Section 3.2.1) being incapable of exactly conserving probability and ice thickness at the model's resolution. The other is due to the thick ice tail of the thickness distribution extending beyond the maximum modelled ice thickness. When the growth rate becomes negative at the maximum modelled ice

thickness a boundary condition is applied that sets $g(h_{max}) = 0$ which gives this slight discontinuity in the mean thickness. Figure 10 also shows a slightly different ice area fraction to that seen for the Fokker-Planck parameterisation in Figure 7. There is a similarly abrupt freeze-up of open water, but this coincides with the open water fraction reaching its maximum value, unlike in the Fokker-Planck case. This is because the Fokker-Planck parameterisation allows for mechanical processes to *decrease* the open water fraction. This is not possible with coagulation mechanics so the open water fraction (ice area fraction) monotonically increases (decreases) until open water freezes up entirely.

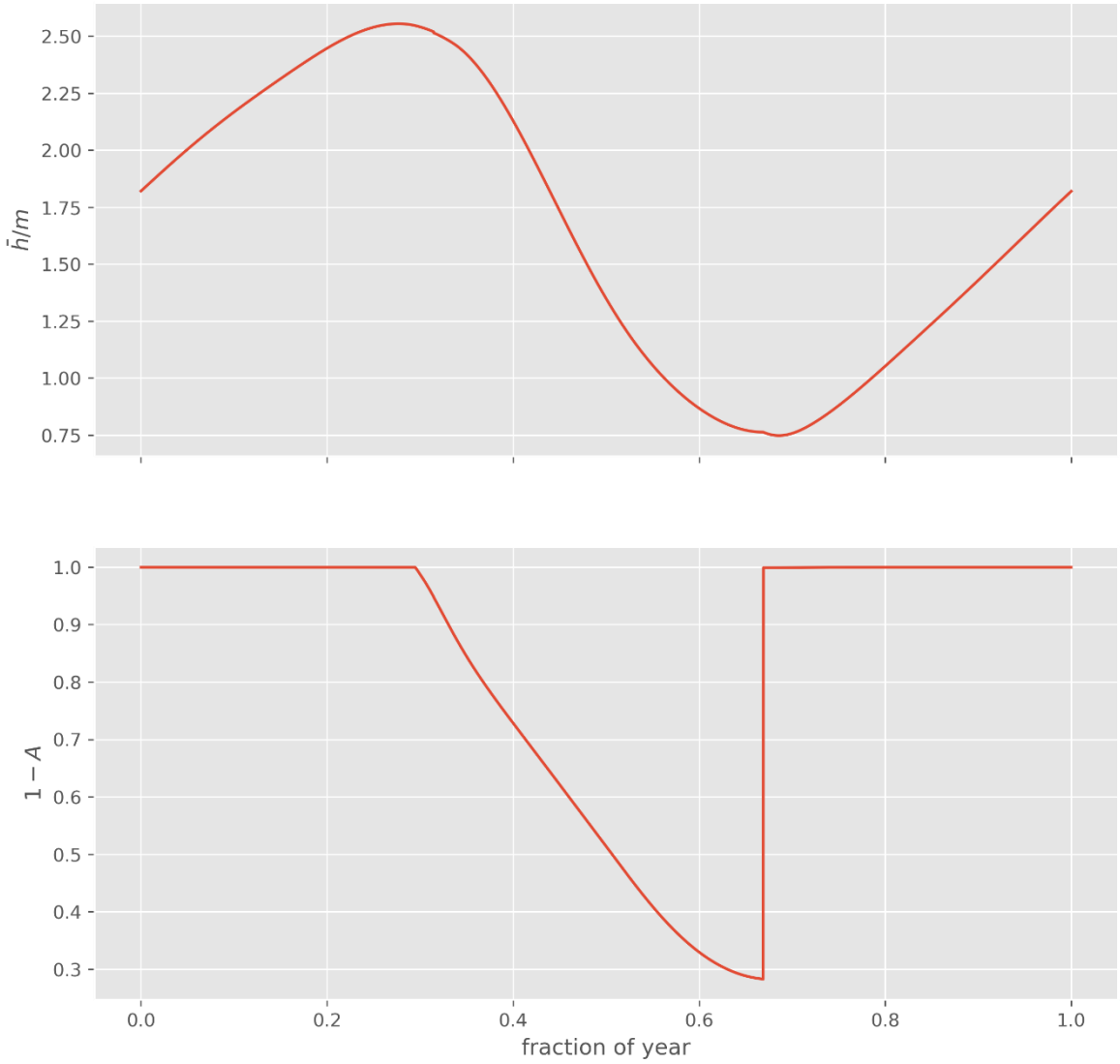


Figure 10 Seasonal cycles of mean thickness of the ice pack, $\bar{h} = \int_0^{h_{max}} ghdh$, and the ice area fraction, $1 - A = \int_0^{h_{max}} gdh$, when the ice thickness distribution is modelled using the coagulation mechanics parameterisation using the EW09 surface forcing cycles with $\Delta F_0 = 0\ Wm^{-2}$ and $r = 10^{-7}\ ms^{-1}$.

4.2.1 Results using the coagulation parameterisation

Figure 11 shows the bifurcation structure of the system for r values of $0\ ms^{-1}$ and $10^{-7}\ ms^{-1}$ when the system is forced by a surface radiative forcing perturbation ΔF_0. The model state is represented using the scalar mean surface energy density, E, similar to that used in EW09:

$$E = \begin{cases} -\rho_i L_i \bar{h} & E < 0 \text{ (ice-covered)} \\ c_{ml} H_{ml} T_{ml} & E \geq 0 \text{ (ice-free)} \end{cases} \quad (27)$$

For the blue branch the system was initiated with the steady state thickness distribution identified in Toppaladoddi and Wettlaufer (2015) for the lowest forcing configuration and with the beginning of the seasonal cycle of the previous steady state as the forcing was incrementally increased. For the red branch the system was initiated with a mixed layer temperature of $278\ K$ for the lowest forcing configuration. As the forcing was incrementally increased the system was initiated with the beginning of the seasonal cycle of the previous steady state if that was ice-free, if the previous steady state was not ice-free it was initiated with a mixed layer temperature of $278\ K$. The system was run with a timestep of 2 hours, thickness resolution of 10 cm, and a maximum thickness of 10 m. The form of Figure 11 showed no change when initiated with a variety of initial conditions. The steady state seasonal cycles are represented by the shaded regions and are bounded by solid lines representing annual extremes. The abrupt vertical lines mark the points where the system switches to an alternative stable state. The seasonal temperature range of the ice-free state is quite large as in Eisenman and Wettlaufer (2009) – this is possibly due to the lack of heat loss to the deep ocean in these models. Figure 12 shows an example of the seasonal cycle of ice thickness distributions modelled by the coagulation mechanics parameterisation for $r = 10^{-7}\, ms^{-1}$. In this approximation of the statistical equilibrium state the changes in the quantities $\int_0^\infty g\, dh$ and $\int_0^\infty gh\, dh$ between one year and the next are $9 \cdot \dot{1}0^{-9}$ and $0.0009\, m$ respectively.

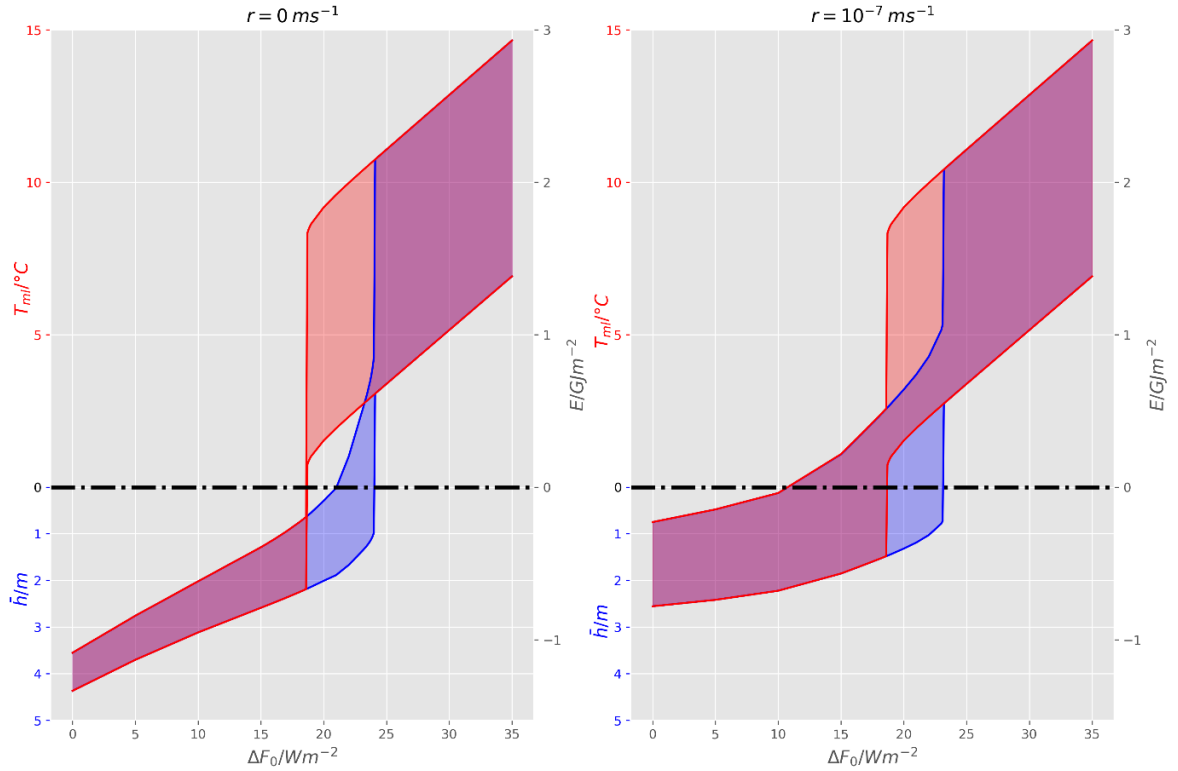


Figure 11 Bifurcation diagrams for the ice thickness distribution using the coagulation mechanics scheme with a constant kernel with values of $0\ ms^{-1}$ (i.e. no mechanics – left) and $10^{-7}\ ms^{-1}$ (right). The model was forced with prescribed surface forcing data from EW09 and used the same albedo parameterisation and linearised Stefan-Boltzmann law as EW09. Steady states were found by initiating the model in ice-covered (blue) and ice-free (red) states. For each surface forcing perturbation, ΔF_0, solid lines plot the annual maximum (upper curve) and annual minimum (lower curve) total surface energy density, E. The shaded region represents the data covered in the seasonal cycle between these extremes. For negative E the system is ice-covered with mean thickness, $\bar{h} = -E/(\rho_i L_i)$, for positive E the system is ice-free with mixed layer temperature, $T_{ml} = E/(c_{ml} H_{ml})$.

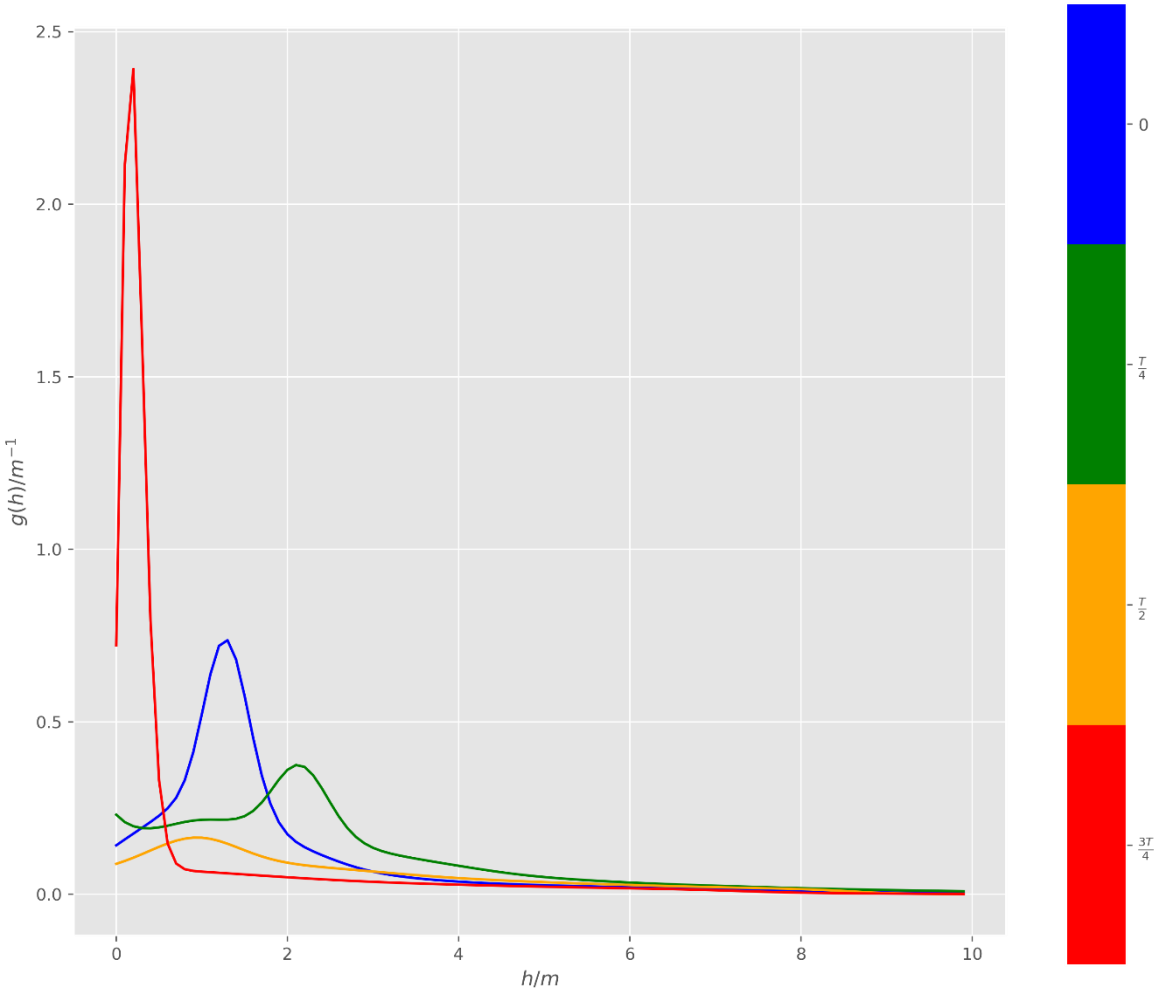


Figure 12 Seasonal cycle of the ice thickness distribution when modelled with the coagulation mechanics parameterisation with $r = 10^{-7}\ ms^{-1}$ and with $\Delta F_0 = 0\ Wm^{-2}$. Thickness distributions are shown for points in the year equally separated in time: $t = 0, \frac{T}{4}, \frac{T}{2}, \frac{3T}{4}$ – where $t = 0$ is the beginning of January 1st, and T is the quarter of the length of the year.

The strength of bistability for a given configuration can be measured as the range of ΔF_0 values for which there are two stable solutions which I represent as B.

For $r = 0\ ms^{-1}$ (left), $B = 5.4\ Wm^{-2}$ – a similar value to the value for the standard slab ice EW09 model, $B = 5.2\ Wm^{-2}$. This suggests that in this implementation of the model, in the absence of mechanical processes, resolving a distribution of ice thicknesses slightly stabilises the ice cover. A stabilising effect is likely due to the resolution of a tail of fast-growing thin ice for high mean thicknesses. However, the difference is very small and dispersion from the upwind scheme for thermodynamic growth may have introduced errors to the system.

Comparing $r = 10^{-7}\ ms^{-1}$ (right) to $r = 0\ ms^{-1}$ (left) illustrates the effect collisions have on the system. As the only difference between the two is in their representation of sea ice, the upper ice-free band is identical for the two cases, however the lower ice-covered band shows some clear differences. For low ΔF_0 values the mean ice thickness, $\bar{h}$, of the system is much lower when mechanics are resolved. This is likely because the mechanics term acts as a source for open water therefore decreasing the mean albedo of the system and increasing the total energy input. The sensitivity of $\bar{h}$ to increasing ΔF_0 is much less when mechanics are included however, and in both cases the ice-covered state ceases to be stable at similar points – for $r = 10^{-7}\ ms^{-1}$, $B = 4.5\ Wm^{-2}$. Interestingly, introducing collisions in the $r = 10^{-7}\ ms^{-1}$ case changes the nature of the abrupt transition associated with cooling the ice-free branch past its bifurcation point. Without collisions the system transitions from a perennially ice-free to a perennially ice-covered state, but with $r = 10^{-7}\ ms^{-1}$ it transitions from a perennially ice-free to a seasonally ice-free state.

Figure 13 shows the width of the bistable region, B, for the r values for each model run. As r increases the width of the bistable region decreases, until B reaches a value of 0 between $r = 10^{-7}\ ms^{-1}$ and $r = 2 \cdot 10^{-7}\ ms^{-1}$. The sensitivity of B to changes in r increases with r – the change in B as r increases from 1 to $2 \cdot 10^{-7}\ ms^{-1}$. is approximately 4 times larger than the change as r increases from 0 to $10^{-7}\ ms^{-1}$. Note that the kink seen in Figure 13 is an artefact of the resolution of r values tested.

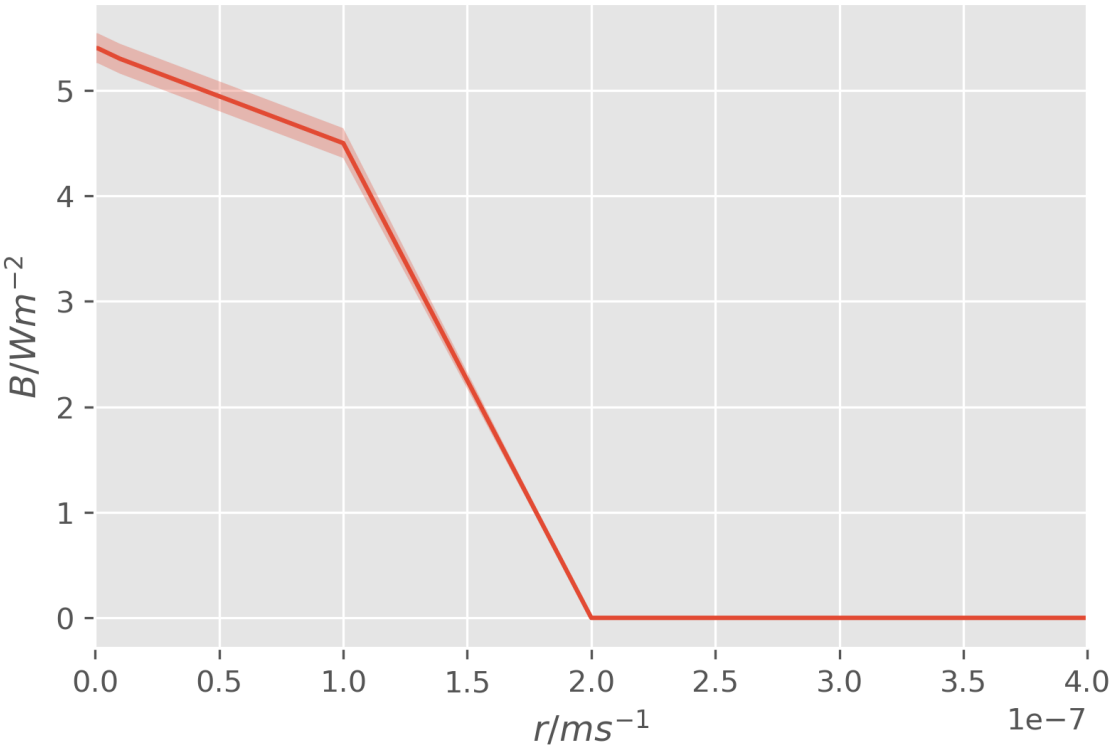


Figure 13 The relationship between the width, B, of the bistable region of the ice thickness distribution model and r, the constant coagulation kernel. The shaded region around the line represents the uncertainty in B, calculated from the resolution of ΔF_0 values used when searching for bistable states. For $r > 2 \cdot 10^{-7}\ ms^{-1}$ the uncertainty is $\pm 0.005\ Wm^{-2}$. The model is run in the same configuration as in Figure 11.

This result suggests that the inclusion of mechanical processes in a sea ice model reduces bistability by destabilising the ice-covered state. Interestingly, for $r > 2 \cdot 10^{-7}$ the system ceases to be bistable – in line with most GCM experiments (Armour *et al.*, 2011; Ridley, Lowe and Hewitt, 2012). This could potentially be interpreted as being due to frequent collisions increasing the system's open water fraction during the melt season, therefore increasing the bottom flux and melt rate. For sufficiently large r this causes the system to become ice-free for a value of ΔF_0 that is less than the bifurcation point on the ice-free branch. However, the degree to which bistability is reduced is highly dependent on the rate at which collisions take place, represented here by a coagulation kernel which is poorly constrained. This work could be extended by tuning the model output for $\Delta F_0 = 0$ to observations to find an

estimate of r in line with observations – allowing the effect of ice mechanics on bistability to be better constrained.

A further uncertainty is the functional form of the coagulation kernel, K. Here I have assumed it takes on a constant value, but this is a simplification as it assumes that ice segments of any thickness are as likely as each other to be involved in a mechanical process. A more accurate representation would preferentially represent processes involving thin ice. However, Godlovitch, Illner and Monahan (2011) show that a kernel of the form $K(x,y) \propto exp\big(-\beta(x+y)\big)$ models the evolution of g similarly to a constant kernel so the choice of kernel form may not have much impact.

5 Conclusions

In this chapter I give an overview of the ice thickness distribution, $g(h)$, and demonstrate its use for two different parameterisations of the redistribution term, ψ: the Fokker-Planck parameterisation and the coagulation parameterisation.

I demonstrate that due to an error term in the conservation of ice mean thickness, the Fokker-Planck parameterisation (Toppaladoddi, Moon and Wettlaufer, 2023) stabilises the ice thickness distribution from entering an ice-free state for very high surface forcing perturbations. This is due to the choice of constant values for the model parameters representing the first and second moments of the thickness transition probability, k_1 and k_2. I use an extension of the model outlined in Toppaladoddi, Moon and Wettlaufer (2023) that accounts for energy fluxes over open water – but similar behaviour can be seen without this modification. While this makes this parameterisation of ψ unsuitable for the modelling of the transition to an ice-free system, this parameterisation still holds value for its ability to fit contemporary observations with a very simple and computationally cheap functional form. This model could be extended to allow for a more accurate transition to an ice-

free state by incorporating a dependence on h and $g(h)$ into k_1 and k_2, however it would be much more difficult to constrain the form of these arbitrary functions and tune them to fit observations.

I also present steady state seasonal cycles of the ice thickness distribution using the coagulation parameterisation. When the frequency of mechanical events is set to 0 the system shows only a slight decrease of $0.2\ Wm^{-2}$ in the width, B, of the bistable region. As some numerical error is expected to be introduced by dispersion in the upwind scheme used for the thermodynamic growth of g this result is not strong enough to suggest any effect on the bistability of the system from the representation of a range of ice thicknesses. I then investigated the effect of increasing the frequency of mechanical events by changing the value of the constant coagulation kernel, r. As r increases, B decreases – likely due to mechanics increasing the area fraction of low-albedo open water and thin ice, therefore increasing the total energy input to the system. It is important to note that the magnitude of this effect depends on the treatment of energy input into the model's open water fraction. It is likely that I overestimate the contribution of this to ice melt which would exaggerate its impact as I presume 100% of it is converted into bottom melt, whereas in reality it would also contribute to warming of the mixed layer, lateral melt and ocean heat transport. The value of r for which bistability in the system stops is between $r = 10^{-7}\ ms^{-1}$ and $r = 2 \cdot 10^{-7}\ ms^{-1}$. The coagulation kernel is an arbitrary two-variable function so is poorly constrained. Even for the constant kernel that I assume it is hard to constrain r and harder still to determine how it would evolve in a changing climate. It is therefore difficult to constrain the size of the effect of mechanics on bistability in the system. A potential method for tuning a given functional form of the coagulation kernel would be to compare the decay rate of the model's thick-ice tail when forced with contemporary surface forcing cycles to the

decay rate of the observed ice thickness distribution’s thick-ice tail. The model could be tuned to the parameters that best agree with the observed decay rate.

Chapter 3 The Arctic single column model

"Nature is a temple in which living columns sometimes emit confused words. Man approaches it through forests of symbols, which observe him with familiar glances"

Correspondences, Charles Baudelaire[1]

1 Introduction

Models like the thickness distribution models in the previous chapter and EW09 only explicitly resolve changes in the Arctic ice cover and so can only explicitly resolve feedbacks related to sea ice cover. However, even models with a suppressed ice-albedo feedback show pronounced Arctic amplification of surface warming (e.g. Winton, 2006) indicating the importance of other feedbacks for the response of the Arctic surface to a changing climate, including cloud, lapse rate, water vapour and heat transport feedbacks.

Many of these feedbacks arise from changes in the Arctic atmosphere, which then affect the surface energy budget. This emphasises the importance of resolving changes in the Arctic atmosphere to accurately model the bifurcation structure of Arctic sea ice. To investigate this, I coupled a single column model (SCM) of the Arctic atmosphere to the EW09 sea ice model (outlined in chapter 1).

In section 2 of this chapter I explore several key features of Arctic climate in more detail and outline how they might affect the bifurcation structure of Arctic sea ice. In section 3 I then give an overview of the single column model and discuss how these

[1] Translator unknown

features are represented in it. I then discuss tuning the model and compare it to observations in section 4. In section 5 I present a summary.

Results from this model are presented in the following chapters. Chapter 4 explores the effect of local atmospheric processes within the Arctic atmosphere on the bifurcation structure and chapter 5 how atmospheric heat transport feedbacks affect the bifurcation structure.

2 Key features of Arctic climate

2.1 Vertical temperature profile

Recent work has emphasised the importance of resolving the vertical structure of the Arctic atmosphere to capture surface based Arctic amplification (Payne, Jansen and Cronin, 2015; Cronin and Jansen, 2016; Henry *et al.*, 2021).

Low latitude climates can roughly be approximated as being in radiative convective equilibrium, where convection is active and fixes temperature profiles to the moist adiabat. This distributes the atmospheric temperature response to forcing throughout the convectively active part of the atmosphere. As a result, warming is enhanced in the upper troposphere and weaker near the surface. (Payne, Jansen and Cronin (2015) and Cronin and Jansen (2016) demonstrate that high-latitude climates are better approximated by radiative-advective equilibrium. Here longwave cooling of the atmosphere is balanced by atmospheric heat transport and atmospheric absorption of solar radiation. Crucially, they identify that unlike the circumstance of radiative-convective equilibrium, the temperature response of the system depends on the vertical structure of the forcing. They demonstrate that increased CO_2 concentration in the absence of a water vapour feedback leads to surface amplified warming in high-latitudes compared to low-latitudes. (The stronger water vapour feedback at low-latitudes masks this relative amplification between

high- and low-latitudes). This surface amplification of polar warming was first identified using a GCM in Manabe and Wetherald (1975).

Henry *et al.* (2021) extend this work by considering the temperature response of low- and high-latitude columns to a range of different forcings. Their results show that increases in longwave absorbers (CO_2 and water vapour) lead to bottom heavy warming, whereas increases in atmospheric heat transport warm the upper troposphere more.

This behaviour is related to the prevalence of surface-based temperature inversions in the Arctic climate (Medeiros *et al.*, 2011). These are regions of vertically increasing temperature near the surface, with temperature differences reaching up to $20\ K$ maintained by a balance of radiative cooling and advective heat transport (Serreze and Barry, 2014). Bintanja, Graversen and Hazeleger (2011) demonstrate that the cooling efficiency of the Arctic atmosphere decreases with increasing temperature inversion strength and demonstrate that stronger temperature inversions lead to stronger temperature amplification.

It is clear that 0-dimensional models of the kind discussed previously cannot capture either: the ‘Arctic amplification’ caused by the surface-weighted warming from increased longwave absorber concentration, or the sensitivity of the Arctic atmosphere to the vertical structure of forcing. This second point is important when considering changes in cloud cover and heat transport within the Arctic. It is likely that this additional amplification term will act to destabilise the stable ice state – decreasing regions of bistability in the Arctic sea ice system.

Another reason it is important for a model to resolve the vertical structure of the Arctic atmosphere is that in the absence of fast convective processes the Arctic atmosphere often doesn’t have time to reach an equilibrium state compared to the

timescale of seasonal changes in insolation and heat transport. The slow timescale is because the temperature profile is largely controlled by slow radiative processes. This is in contrast to systems with relatively fast atmospheric responses where the atmosphere can quickly reach an equilibrium state with the insolation and surface conditions. The long-term equilibrium behaviour of the system is more accurately characterised by tracking its transient behaviour, not approximating an equilibrium state.

2.2 Clouds

The radiative effect of clouds on the surface can generally be partitioned into a negative shortwave and positive longwave component. In the shortwave, the increased albedo of clouds with respect to the atmosphere *decreases* the fraction of downwelling shortwave flux reaching the surface. In the longwave, the increased emissivity of clouds with respect to the atmosphere closes atmospheric windows for outgoing longwave radiation and *increases* downwelling longwave flux at the surface.

Throughout this thesis I will use the term *cloud radiative effect (CRE)* to refer to the difference in *net downward* radiation fluxes, $F_{net\downarrow}$, at the *surface* between a cloudy and clear sky atmospheric state:

$$CRE_{SW} = F_{SW,\,net\downarrow,\,cloudy} - F_{SW,\,net\downarrow,\,clear\ sky} \tag{28}$$

$$CRE_{LW} = F_{LW,\,net\downarrow,\,cloudy} - F_{LW,\,net\downarrow,\,clear\ sky} \tag{29}$$

$$CRE_{net} = CRE_{SW} + CRE_{LW} \tag{30}$$

where subscript SW and LW represent shortwave and longwave fluxes respectively.

The shortwave cloud radiative effect is weakened in the contemporary Arctic because of two key factors. During polar night there is no insolation in the Arctic, meaning clouds have no shortwave effect on the surface radiation budget for much

of the year. Secondly, the net surface shortwave flux at the surface is already low in the absence of clouds due to the high surface albedo of the Arctic, meaning the shortwave cloud radiative effect is small even when sunlight is present. These factors mean that generally the net surface longwave cloud radiative effect dominates giving Arctic clouds a positive effect in the annual average. Low level Arctic clouds contribute significantly to this as they radiate at a relatively high temperature to the surface. Observations over the ice-covered Beaufort sea from the SHEBA campaign show a net-positive cloud radiative effect all year round except briefly in July (Shupe and Intrieri, 2004).

Seasonality in Arctic cloud cover is primarily driven by low level cloud cover. During summer there is a strong increase in low cloud cover in the Arctic, caused by the advection of moist air from lower latitudes that condenses in the colder Arctic atmosphere (Curry *et al.*, 1996).

The longwave radiative effect of clouds increases with their radiating cloud base temperature (Dong *et al.*, 2010). Due to the Arctic temperature inversion low Arctic clouds often radiate at a greater temperature than the Arctic surface and contribute strongly to a positive cloud radiative effect, particularly during winter. As a result, temperature inversions are typically weaker in cloudy than clear sky conditions (Serreze and Barry, 2014).

Abbot and Tziperman (2008) identify the formation of high convective clouds in winter as a potential mechanism for stabilising ice-free Arctic states due to their positive cloud radiative effect inhibiting the formation of ice in the winter.

2.3 Horizontal heat transport

If there were no energy transport from lower latitudes into the Arctic it would exist at much lower temperatures, due to the low input of solar energy (zero during polar

night). Heat transport by the atmosphere and oceans allows the Arctic to maintain its temperature.

Serreze *et al.* (2007) demonstrate from ERA-40 reanalysis data and other sources that the annual energy deficit in the Arctic atmosphere-ocean column north of $70\,°N$ from radiative fluxes is $-110\,Wm^{-2}$. This is primarily compensated by atmospheric heat flux convergence of $100\,Wm^{-2}$ with heat fluxes at the surface balancing the remaining $10\,Wm^{-2}$. Limiting their analysis to the Arctic ocean domain only they calculate the size of ocean heat transport as $3\,Wm^{-2}$ – two orders of magnitude less than the atmospheric heat transport.

2.3.1 Atmospheric heat transport

Atmospheric energy transport into the Arctic can be broken down into the component parts of moist static energy:

$$\left(c_p T + \Phi + L_v q\right)v \qquad (31)$$

where c_p is the specific heat capacity of dry air at constant pressure, T is air temperature, Φ is geopotential, L_v is the latent heat of vaporisation of water, q is specific humidity, and v is northward windspeed. There is also a contribution from kinetic energy, but this is small so can be neglected.

Sensible heat transport is the largest contribution ($\sim 66\,Wm^{-2}$), while latent heat and geopotential components are similar in magnitude ($\sim 16\,Wm^{-2}$) (Cardinale *et al.*, 2021).

In the contemporary climate, atmospheric heat transport is strongest in winter and weakest in summer. This seasonality is driven by the sensible component as the meridional temperature gradient is strongest then. Both latent and geopotential

components are strongest in summer, driven by seasonal cycles in atmospheric water content and geopotential.

Changes to atmospheric heat transport under global warming are uncertain. As the Arctic warms at a greater rate than lower latitudes, the meridional temperature gradient will decrease likely leading to a decrease in sensible heat transport, but a moister atmosphere overall will likely lead to an increase in latent heat transport (e.g. Yoshimori et al., 2014). The relative size of these contributions is uncertain. Henry and Vallis (2021) find that in a GCM without clouds or sea ice these changes cancel out and the overall size of atmospheric heat transport stays roughly constant for doubled and quadrupled atmospheric CO_2.

A more moisture heavy atmospheric heat transport is likely to be more effective at warming the surface for two reasons: a) the increase in specific humidity and cloud cover would increase surface downwelling longwave fluxes, and b) latent heat transport is more bottom-heavy and therefore more effective at heating the surface for a system in radiative-advective equilibrium.

2.3.2 Oceanic heat transport

Serreze *et al.* (2007) indicates that ocean heat transport is roughly constant at $\sim 3\ Wm^{-2}$ throughout the year and that changes to ocean/ice heat content is driven by surface fluxes. This is in agreement with work suggesting the ice-ocean heat flux is primarily driven by surface fluxes as opposed to ocean heat transport (e.g. Maykut & McPhee, 1995). In their analysis Yoshimori *et al.* (2014) find that feedbacks in ocean heat transport are of secondary importance compared to atmospheric heat transport feedbacks under CO_2 increases. However, it should be noted that ocean heat flux (if delivered at the sea ice bottom surface) is more effective at thinning ice cover than heat flux at the ice top surface. This is because the shallower

temperature gradient near the ice bottom surface makes ice thickness more sensitive to changes in bottom heat flux.

The small size of the oceanic heat transport is linked to the fact that the Arctic is mostly bounded by land with a few open ocean gateways. Oceanic heat convergence will likely be larger near these gateways, but these effects are not resolved in my column model.

3 The single column model

To resolve the effect of local atmospheric feedbacks on sea ice and the surface energy budget I coupled a sea ice model to a single column model of the Arctic atmosphere. I used the climt modular framework (Merwin Monteiro, McGibbon and Caballero, 2018) to construct and run this model. I used the following built-in model components:

- The RRTMG radiation scheme (Clough *et al.*, 2005) and built-in insolation scheme to represent shortwave and longwave radiation. RRTMG has separate model components to represent shortwave and longwave radiation. It represents the radiative effect of all significant atmospheric gases. It uses a two-stream approximation and splits fluxes into spectral bands. When clouds are included I use the McICA method (Pincus, Barker and Morcrette, 2003) to allow for fractional cloud area within a model level .
- The Emanuel convection scheme (Emanuel and Živković-Rothman, 1999) to represent convection – this is a mass-flux convection scheme. Note that in climt the dry convective adjustment step is included in a separate component (also used).

- The SimplePhysics scheme (Reed and Jablonowski, 2012) to represent surface heat fluxes, a simple diffusive boundary layer and large-scale condensation (in the absence of a cloud scheme).

I also included additional components to represent:

- Air temperature and moisture tendencies from atmospheric heat transport.
- A mixed-phase saturation adjustment cloud scheme based on Tao, Simpson and McCumber (1989).
- A surface component allowing for uniformly ice-covered and ice-free states based on Eisenman and Wettlaufer (2009). Note this does not model the ice thickness distribution.

These additional components are discussed in greater detail in subsection 3.1.

The SCM in effect solves the following equations for the rate of change of air temperature, T, and specific humidity, q:

$$\frac{\partial T}{\partial t} = \frac{\partial T}{\partial t}|_{rad} + \frac{\partial T}{\partial t}|_{conv} + \frac{\partial T}{\partial t}|_{adv} + \frac{\partial T}{\partial t}|_{cond} + \frac{\partial T}{\partial t}|_{boundary} \quad (32)$$

$$\frac{\partial \mathrm{q}}{\partial \mathrm{t}} = \frac{\partial \mathrm{q}}{\partial \mathrm{t}}|_{\mathrm{conv}} + \frac{\partial \mathrm{q}}{\partial \mathrm{t}}|_{\mathrm{adv}} + \frac{\partial \mathrm{q}}{\partial \mathrm{t}}|_{\mathrm{cond}} + \frac{\partial \mathrm{q}}{\partial \mathrm{t}}|_{\mathrm{boundary}} \quad (33)$$

The subscripts rad, conv, adv, cond and boundary represent the effect of radiation, convection, atmospheric advection, condensation and boundary processes respectively. These are represented using the components discussed above.

When run in a clear-sky consideration, any water in excess of saturation is condensed and immediately precipitated to the surface. When the cloud scheme is included this is compensated by a change in cloud liquid water and cloud ice, q_c and q_i such that:

$$\frac{\partial \mathrm{q_c}}{\partial \mathrm{t}} + \frac{\partial \mathrm{q_i}}{\partial \mathrm{t}} = -\frac{\partial \mathrm{q}}{\partial \mathrm{t}}|_{cond} + \frac{\partial \mathrm{q_c}}{\partial \mathrm{t}}|_{precip} + \frac{\partial \mathrm{q_i}}{\partial \mathrm{t}}|_{precip} \quad (34)$$

The subscript precip represents precipitation. These are represented using the components discussed above.

The column model as a whole is represented in the schematic Figure 14.

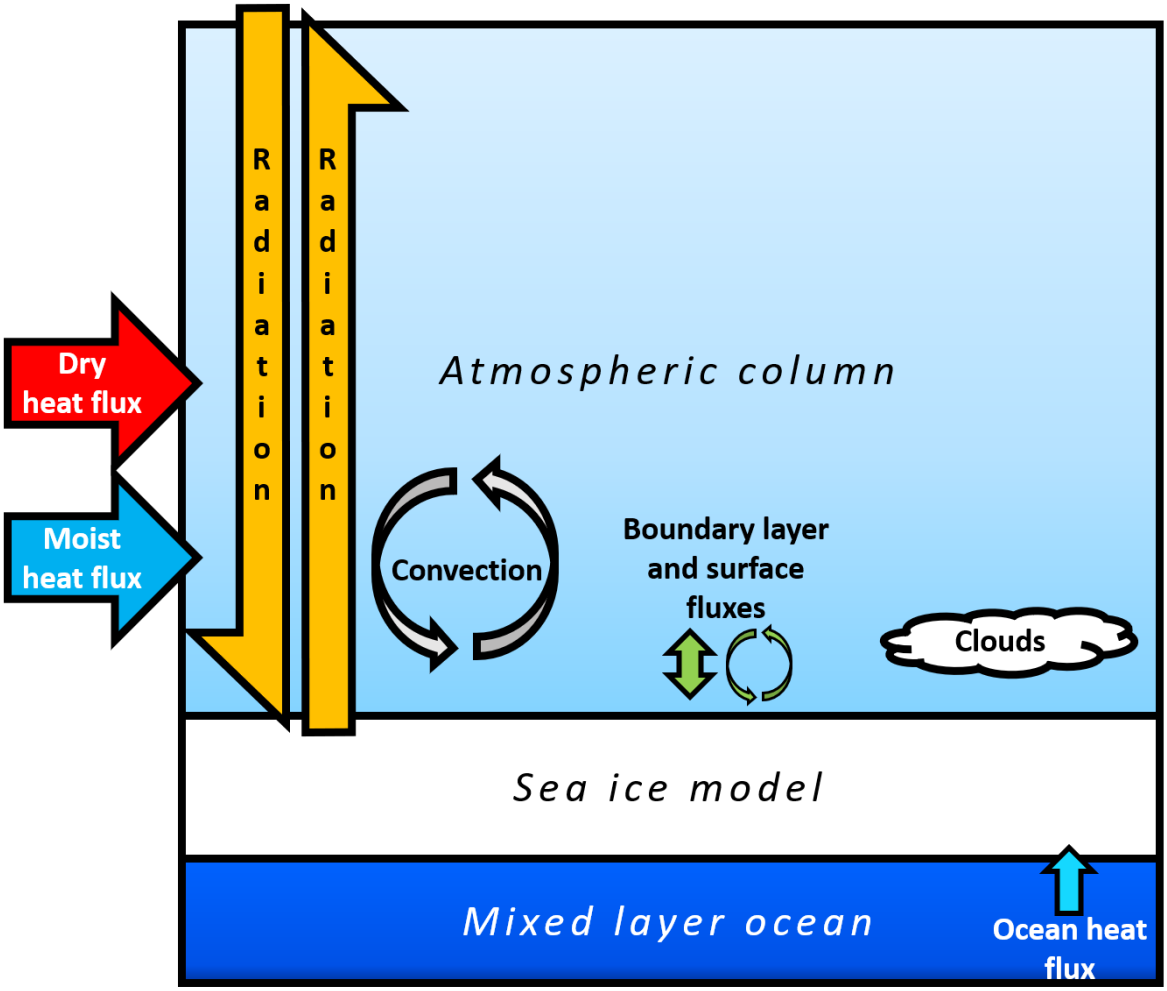


Figure 14 Schematic diagram of the components included in the single column model. The model is forced at the sides by dry and moist heat transport. The surface is represented by the EW09 ice model (which resolves a constant ocean heat flux). The column atmosphere uses the RRTMG radiation scheme; the Emanuel convection scheme; SimplePhysics scheme for the boundary layer and surface fluxes; and a mixed-phase saturation-adjustment cloud scheme.

Figure 15 shows an example simulation of a column model in radiative-convective equilibrium run using climt. As expected for a system in approximate radiative-convective equilibrium the temperature profile follows a moist adiabat above the dew point and a dry adiabat below the dew point. Throughout the troposphere, air

temperature tendencies from shortwave radiation, longwave radiation and convection balance out. Near the surface turbulent heat fluxes disrupt this balance. The model also produces a stratospheric temperature inversion caused by absorption of UV radiation by ozone.

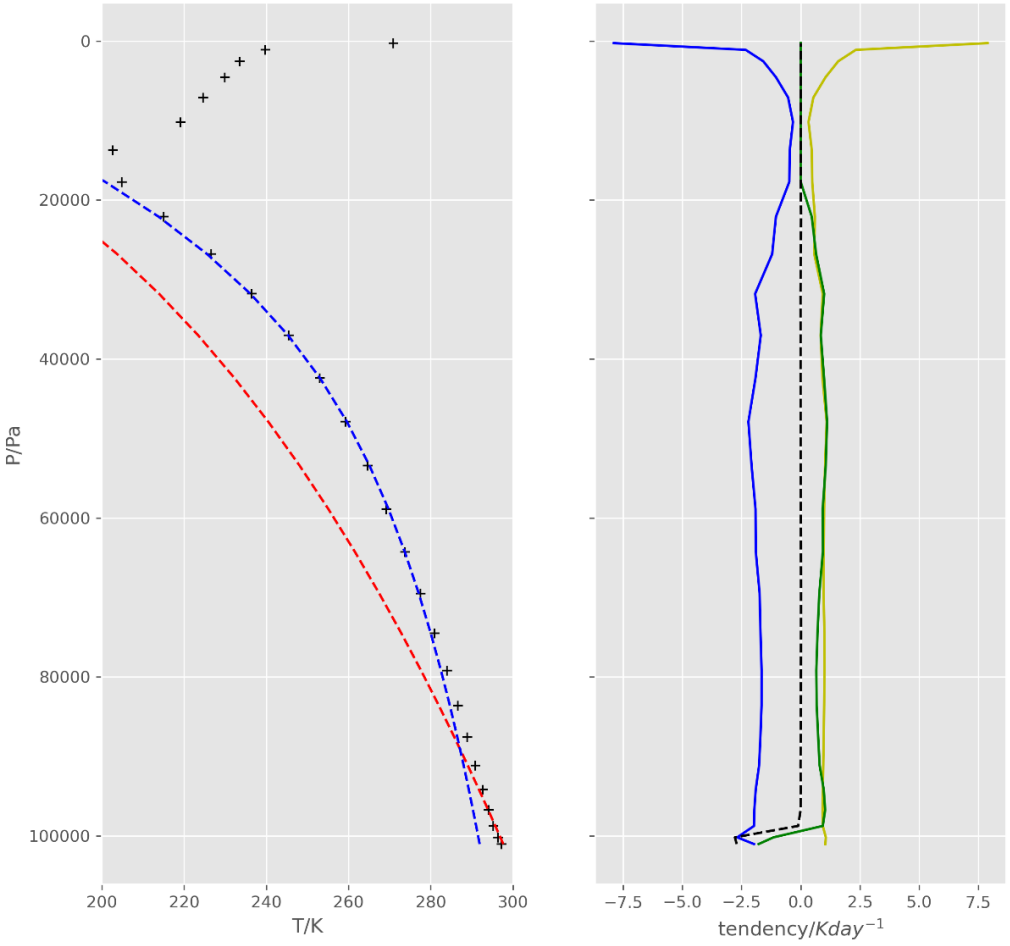


Figure 15 Left: Approximate radiative convective equilibrium temperature profile found using a climt model (black +'s), plotted against a moist (blue dashes) and dry (red dashes) adiabat. Right: Balance of air temperature tendencies from longwave radiation (blue); shortwave radiation (yellow); and convection (green). Total air temperature tendency is plotted as a black dashed line. The model output was calculated using a column model using: RRTMG shortwave and longwave components for radiation, the simple physics boundary scheme, the Emanuel convection scheme with a dry convective adjustment component and a slab ocean.

This example model was run without any seasonal variation or external forcing. The model included the default RRTMG radiation, Emanuel convection and SimplePhysics components. The surface was represented as a slab ocean with depth of $5\,\mathrm{m}$. The solar zenith angle was held constant at $2\pi/5$ radians. The incoming flux at the top of atmosphere is equal to the solar constant (set at $1367\ Wm^{-2}$) multiplied by the cosine of the solar zenith angle.

In the following sub-section, I outline how I represented important features of Arctic climate through new model components and modifications to built-in components.

3.1 Outline of homebrew model components & modifications

I made the following adjustments to built-in components in climt:

- **Simple Physics** – I modified the calculation of surface latent heat fluxes to use the latent heat of sublimation of ice when the surface is ice covered (Andreas *et al.*, 2010), instead of the default latent heat of vaporisation.
- **Instellation** – I modified the component to compute the diurnally averaged solar zenith angle, which I used throughout my project.
- **RRTMG** – RRTMG was unstable in model runs with high CO_2 when the upper atmosphere reached low temperatures. To prevent the model crashing I imposed an artificial temperature minimum of $155\ K$ for layers where the air pressure was below $2\ kPa$.

In the following sections I outline additional model components I included to simulate clouds, atmospheric heat transport, and sea ice.

3.1.1 Cloud scheme

I represented clouds in my model using a simple mixed-phase saturation adjustment scheme based on Tao, Simpson and McCumber (1989). The form of mixed-phase

saturation adjustment used has been shown to give good agreement with SHEBA observational data (Fu and Hollars, 2004). In this scheme all water vapour over the saturation threshold is converted into either cloud liquid water or cloud ice. Throughout this section q_c and q_i represent the mixing ratios of cloud liquid water and cloud ice respectively.

A change in specific humidity, dq, to account for saturation adjustment is converted into condensation to cloud liquid water, dq_c, and deposition into cloud ice, dq_i, according to:

$$dq_c = dq \cdot \mathrm{CND} \tag{35}$$

$$dq_i = dq \cdot \mathrm{DEP} \tag{36}$$

where:

$$\mathrm{CND} = \begin{cases} 1 & \text{if } T > T_0 \\ \dfrac{T - T_{00}}{T_0 - T_{00}} & \text{if } T_{00} < T < T_0 \\ 0 & \text{if } T < T_{00} \end{cases} \tag{37}$$

$$\mathrm{DEP} = \begin{cases} 0 & \text{if } T > T_0 \\ \dfrac{T_0 - T}{T_0 - T_{00}} & \text{if } T_{00} < T < T_0 \\ 1 & \text{if } T < T_{00} \end{cases} \tag{38}$$

Here T_0 and T_{00} are the threshold air temperatures beyond which supersaturated water is fully converted into liquid water and ice respectively. Here dq, dq_c and dq_i can be interpreted as the condensation terms in equations (33) and (34).

For saturation adjustment calculations, the saturation specific humidity, q_s, is calculated as an average of the saturation specific humidity over liquid water, q_{ws}, and over ice, q_{is}, weighted by the mixing ratios of cloud water, q_c, and cloud ice, q_i,

respectively. When there is no cloud water in a model layer, q_s is weighted using CND and DEP instead.

$$q_s = \begin{cases} \dfrac{q_c q_{ws} + q_i q_{is}}{q_c + q_i} & \text{if } (q_c + q_i) > 0 \\ \mathrm{CND} q_{ws} + \mathrm{DEP} q_{is} & \text{if } (q_c + q_i) = 0 \end{cases} \tag{39}$$

Precipitation is represented at each timestep as an autoconversion process: for cloud liquid water the parameterisation outlined in Sundqvist (1978) is used; and for cloud ice a parameterisation similar to the autoconversion of cloud ice used in IFS (Forbes, 2021).

$$\left.\frac{\partial q_c}{\partial t}\right|_{precip} = -c_{c,0} q_c \left(1 - e^{-\left(\frac{q_c}{q_{c,crit}^2}\right)^2}\right) \tag{40}$$

$$\left.\frac{\partial q_i}{\partial t}\right|_{precip} = -c_{i,0} e^{0.0025\ K^{-1}\cdot(T - T_{fr})} q_i \left(1 - e^{-\left(\frac{q_i}{q_{i,crit}}\right)^2}\right) \tag{41}$$

where the c_0 parameters are base rates for the autoconversion of cloud water to precipitation; q_{crit} are critical cloud water thresholds; and T_{fr} is the freezing point of water (set at $273\ K$). For cloud ice the autoconversion rate increases exponentially with air temperature – this roughly approximates the fact that the aggregation of ice crystals depends on the structure of the crystals which is temperature dependent.

Cloud area fraction, f, is difficult to parameterise due to the lack of a clear physically based parameterisation. I initially used a constant cloud area fraction throughout the atmospheric column, but this led to extremely high surface fluxes and only allowed an ice-covered Arctic in contemporary conditions for $f \approx 0.05$. I then explored two different representations:

1. ERA5 cloud area fraction
2. Parameterised cloud area fraction

3.1.1.1 ERA5 cloud area fraction

In this case I fixed cloud area fraction to the annual mean cloud area fraction of the Arctic (defined as the region north of $70\,°N$) for ERA5 reanalysis over the period 1979-2022.

To correct for differences over land and ocean/sea ice I removed data over land and replaced it with a zonal average of data over ocean/sea ice. This doesn't allow the cloud area fraction to respond to changes in the model, but includes vertical variation.

3.1.1.2 Parameterised cloud area fraction

I also consider the cloud area fraction parameterisation outlined in Le Treut and Li (1991), modified to fit the mixed-phase saturation-adjustment scheme outlined in 3.1.1. The parameterisation determines the cloud area fraction, f, by considering the *total water content*, q_t, in a model layer. This is the sum of cloud liquid water, cloud ice and water vapour in the model layer, $q_t = q_c + q_i + q$. Precipitation (which isn't tracked in this column model) is not considered. q_t is assumed to be uniformly distributed with width $2\Delta q$ – giving maximum and minimum values of $q_t \pm \Delta q$. This implies that for non-zero Δq regions of a model-layer can be super-saturated even when the mean humidity is below the saturation point, and vice versa. The cloud fraction is diagnosed as the fraction of the distribution that is greater than the saturation specific humidity, q_s (Figure 16).

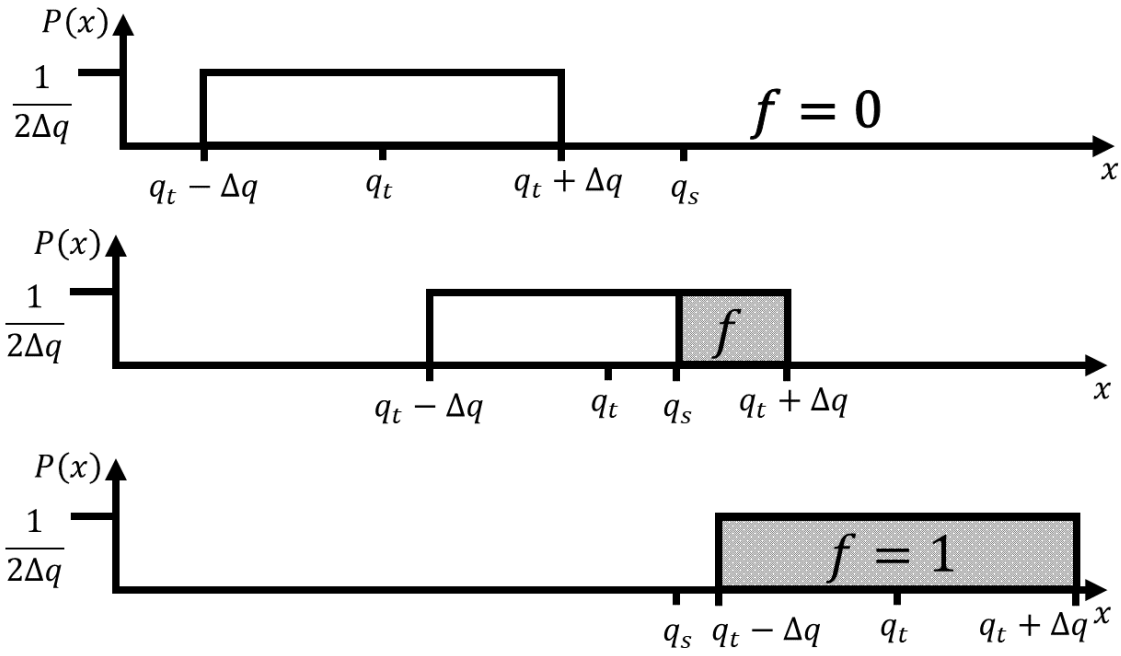


Figure 16 Schematic illustrating the calculation of cloud area fraction, f, uniform distribution of water content, q_t, for completely cloud-free, partially cloud-covered, and completely cloud-covered cases.

A model layer can exist in one of three states:

- **Cloud free:** $q_t + \Delta q < q_s$, $f = 0$.
- **Partially cloud covered:** $q_t - \Delta q < q_s < q_t + \Delta q$, $f = \frac{q_t + \Delta q - q_s}{2\Delta q}$.
- **Completely cloud covered:** $q_s < q_t - \Delta q$, $f = 1$.

In the limiting case where $\Delta q = 0$ this reduces to the simple saturation adjustment case outlined in 3.1.1. This is equivalent to assuming that water vapour is well mixed across the grid cell. I follow Le Treut and Li (1991) and use the form $\Delta q = \gamma q_t$ where γ is some constant fraction less than one.

Below I go through how I couple this cloud area fraction parameterisation with the mixed phase saturation adjustment scheme.

As this parameterisation assumes variable water content across a model layer, q represents the *mean* specific humidity across the layer and scales non-linearly with q_t as the cloud fraction increases. When the system is cloud free $(f = 0)$ the water

content consists only of water vapour so $q = q_t$, the mean total water content of the cloud-free region. When the system is completely cloud covered $(f = 1)$ I assume all regions exist at the point of saturation so $q = q_s$. Taking a weighted combination of these when the system is partially cloud-covered $(0 < f < 1)$ gives $q = f q_s + (1 - f)\frac{q_s + (q_t - \Delta q)}{2}$. Overall:

$$q = \begin{cases} q_t & \text{if } f = 0 \\ \dfrac{2q_s q_t(1+\gamma) - q_s^2 - q_t^2(1-\gamma)^2}{4\gamma q_t} & \text{if } 0 < f < 1 \\ q_s & \text{if } f = 1 \end{cases} \qquad (42)$$

For $f = 1$ and $0 < f < 1$ q is fixed for a given q_s and q_t – this equation therefore gives the specific humidity to which the cloud scheme should try to adjust to, q_{adj}. For $f = 0$ the cloud scheme instead tries to adjust to the specific humidity at which clouds first form, $\frac{q_s}{1+\gamma}$ (see Figure 16). This gives:

$$q_{adj} = \begin{cases} \dfrac{q_s}{1+\gamma} & \text{if } f = 0 \\ \dfrac{2q_s q_t(1+\gamma) - q_s^2 - q_t^2(1-\gamma)^2}{4\gamma q_t} & \text{if } 0 < f < 1 \\ q_s & \text{if } f = 1 \end{cases} \qquad (43)$$

As in Tao, Simpson and McCumber (1989), I adjust to the adjustment specific humidity *at the end* of the adjustment process, q_{adj}^{t+dt}. As the total water content is unaffected by the saturation adjustment process this is controlled purely by changes to q_s. I.e.

$$dq_{adj} = \begin{cases} \dfrac{dq_s}{1+\gamma} & \text{if } f = 0 \\ \dfrac{q_t(1+\gamma) - q_s}{2\gamma q_t} dq_s & \text{if } 0 < f < 1 \\ dq_s & \text{if } f = 1 \end{cases} \qquad (44)$$

Using the q_s definition (39).

$$dq_s = \begin{cases} \dfrac{A_1 q_c q_{ws} + A_2 q_i q_{ws}}{q_c + q_i} dT & \text{if } (q_c + q_i) > 0 \\ (A_1 \mathrm{CND} q_{ws} + A_2 \mathrm{DEP} q_{is}) dT & \text{if } (q_c + q_i) = 0 \end{cases} \tag{45}$$

where $A_1(T)$ and $A_2(T)$ are functions of T.

The dq_s term can be written in terms of dq by relating the change in temperature to the change in specific humidity from condensation/evaporation: $dT = -A_3 dq$ where $A_3 = \frac{L_v \mathrm{CND} + L_s \mathrm{DEP}}{c_p}$.

The adjustment step can then be written as:

$$dq = -q + q_{adj} + dq_{adj} \tag{46}$$

$$dT = -A_3 dq \tag{47}$$

which can be rearranged as:

$$dq = \begin{cases} \dfrac{-q + \dfrac{q_s}{1+\gamma}}{1 + A_3 \dfrac{1}{1+\gamma} q_s} & \text{if } f = 0 \\ \dfrac{-q + \dfrac{2q_s q_t (1+\gamma) - q_s^2 - q_t^2 (1-\gamma)^2}{4\gamma q_t}}{1 + A_3 \dfrac{q_t(1+\gamma) - q_s}{2\gamma q_t} q_s} & \text{if } 0 < f < 1 \\ \dfrac{-q + q_s}{1 + A_3 q_s} & \text{if } f = 1 \end{cases} \tag{48}$$

$$dT = \begin{cases} \dfrac{A_3 \left(q - \dfrac{q_s}{1+\gamma} \right)}{1 + A_3 \dfrac{1}{1+\gamma} q_s} & \text{if } f = 0 \\ \dfrac{A_3 \left(q - \dfrac{2q_s q_t (1+\gamma) - q_s^2 - q_t^2 (1-\gamma)^2}{4\gamma q_t} \right)}{1 + A_3 \dfrac{q_t(1+\gamma) - q_s}{2\gamma q_t} q_s} & \text{if } 0 < f < 1 \\ \dfrac{A_3 (q - q_s)}{1 + A_3 q_s} & \text{if } f = 1 \end{cases} \tag{49}$$

Equations (35) and (36) then partition this into changes in cloud liquid water and cloud ice, dq_c and dq_i, according to CND and DEP.

At each timestep I applied upper and lower limits to dq, dT, dq_c and dq_i to prevent them reaching negative values. When I applied one of these limits I adjusted the other differentials to ensure conservation of moisture/energy. dq can be interpreted as the condensation/evaporation term in (32) and (33).

3.1.2 Atmospheric heat transport

I represented atmospheric heat transport into the Arctic by including components to apply tendencies to air temperature and specific humidity to the column model.

As in Cronin and Jansen (2016) I represent the vertical structure of atmospheric heat transport using power law profiles. I chose to use this simplification over using data from reanalysis to make interpretation of the model outputs simpler and as it allows the vertical structure of heat transport to be easily modified by changing the exponent of the power law profile. However, it cannot represent more complex structures, such as inversions in atmospheric heat transport profiles. I extend this work by considering dry and sensible components of heat transport separately, corresponding to tendencies of air temperature and specific humidity. I represent each with separate power law distributions:

$$F = \int_0^{p_S} Q(p)dp \tag{50}$$

$$Q(p) = n\frac{F}{p_S}\left(\frac{p}{p_S}\right)^{n-1} \tag{51}$$

where F is the convergence of atmospheric heat transport (with the dimensions of a radiative forcing term) into the column and Q is its vertical structure. Giving the following tendencies:

$$\frac{dT}{dt} = Q_{dry}\frac{g}{c_p} \tag{52}$$

$$\frac{dq}{dt} = Q_{moist}\frac{g}{L_v} \tag{53}$$

The dry component of atmospheric heat transport includes sensible heat and geopotential components. Due to the difficulty of representing geopotential transport in a single column model I represent the effect of both terms in a single dry heat transport term.

By default in my model runs I use seasonal cycles for dry and moist heat transport across 70 °N over the period 1980-2016 from NASA-MERRA-2 reanalysis data as calculated by Cardinale *et al.* (2021). The default parameters for the power law distributions are $n = 1$ for dry transport, corresponding to a temperature tendency uniformly distributed in pressure coordinates, and $n = 2$ for moist transport, corresponding to a more bottom-heavy specific humidity tendency directly proportional to air pressure. These values correspond roughly to profiles from reanalysis in Cardinale *et al.* (2021).

3.1.3 Sea ice

I represented sea ice in my model using the EW09 ice model. This model is discussed in greater detail in chapter 1. I give an overview of the modifications made to integrate it into the SCM below.

The energy density coordinate, E, evolves according to the net energy flux, calculated interactively from the SCM:

$$\frac{\partial E}{\partial t} = F_{SW\downarrow} - F_{SW\uparrow} + F_{LW\downarrow} - F_{LW\uparrow} - F_{SH} - F_{LH} + F_B + \nu_0\mathcal{R}(-E) \tag{54}$$

where F_{SW} and F_{LW} represent surface radiative shortwave and longwave fluxes and ↓ and ↑ represent the downwelling and upwelling components respectively. F_{SH} and F_{LH} represent the surface sensible and latent heat fluxes (defined as positive upward). F_B is the ocean heat flux at the ice bottom surface and the term $\nu_0\mathcal{R}(-E)$

represents the export of sea ice from the system. These terms are represented using the same values as discussed in chapter 1.

When the system is ice-covered and the surface temperature, T_s, is below the freezing point of ice, T_s is calculated by solving for energy balance at the ice upper surface. Unlike EW09, I use the Newton-Raphson method to solve the quartic equation:

$$F_{SW\downarrow} - F_{SW\uparrow} + F_{LW\downarrow} - \sigma T_S^4 - F_{SH} - F_{LH} - k_i \frac{T_S - T_B}{h} = 0 \quad (55)$$

To correct for a numerical error in this calculation caused by diverging surface heat fluxes, I use a rolling average of the fluxes specified by climt over a 3-hour timescale.

My component also sets the surface specific humidity to the vapour pressure of water vapour over liquid water when ice-free and the vapour pressure over ice when ice-covered. This is then fed into the Simple Physics boundary layer scheme giving greater surface latent heat fluxes when the surface is ice-free.

4 Model parameters and fit with reanalysis

4.1 Tuning the model

The model as described above has many free parameters. I tune these by fitting them as closely to data from observations and reanalysis. Throughout, I run the model with 30 vertical levels to ensure stability.

4.1.1 Column latitude and solar zenith angle

The column model is designed to simulate the climate of the Arctic from $70 - 90\,°N$. Figure 17 illustrates the range of surface insolation cycles at different latitudes in this region.

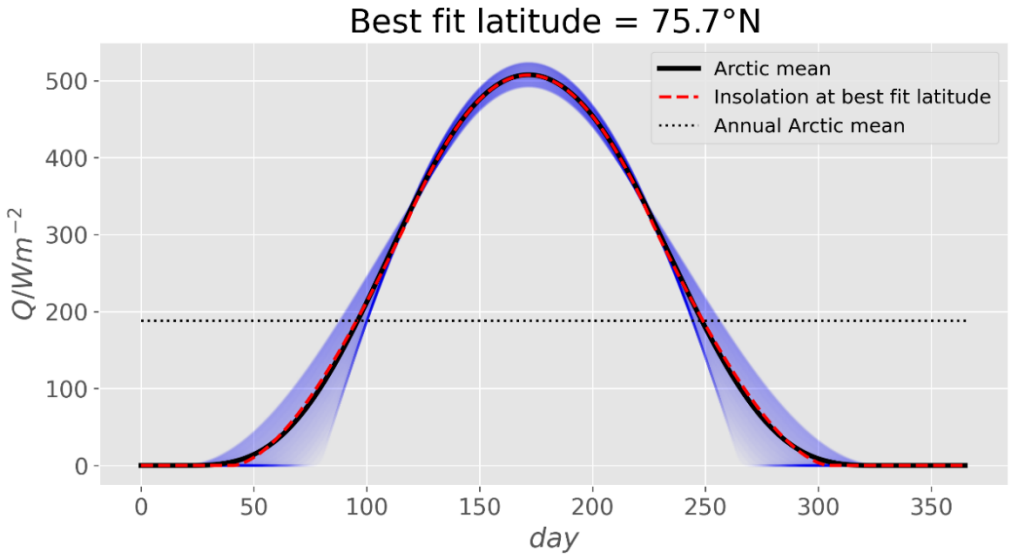


Figure 17 This figure illustrates the annual cycle of surface insolation from $70 - 90\,°N$. The blue envelope marks the area-weighted distribution of surface insolation for each day of the year – darker colours represent a larger population in the distribution. The solid black line plots the area weighted mean surface insolation cycle in the region. The dashed red line plots the surface insolation cycle at $75.7\,°N$ – the best fit at a given latitude to the area weighted mean. The dotted black line plots the area weighted annual mean insolation.

Throughout my project I use a default column latitude of $75.7\,°N$ to approximate the mean insolation cycle between $70 - 90\,°N$ in an easily repeatable way. This gives very good agreement to the Arctic mean, with a slight overestimation of the length of polar night and small discrepancies in surface insolation in Spring and Autumn.

4.1.2 Wind speed

Wind speed is an input parameter for the Emanuel convection and Simple Physics components. Notably surface fluxes are proportional to the near-surface wind speed. I then tuned the column's wind speed by testing the sensitivity of turbulent heat fluxes to different vertically uniform wind speeds (Figure 18). Note that here the heat fluxes are defined as positive when pointing *upwards*. All speeds tested showed the same qualitative form, with the sensible heat flux pointing downwards year-round and weakening during summer (consistent with a weakening inversion) and the latent heat flux near zero during winter and positive during summer.

Based on this sensitivity test I chose a wind speed of $3.0\,ms^{-1}$ as it most closely resembles observational seasonal cycles of each surface heat flux and their total from Persson *et al.* (2002).

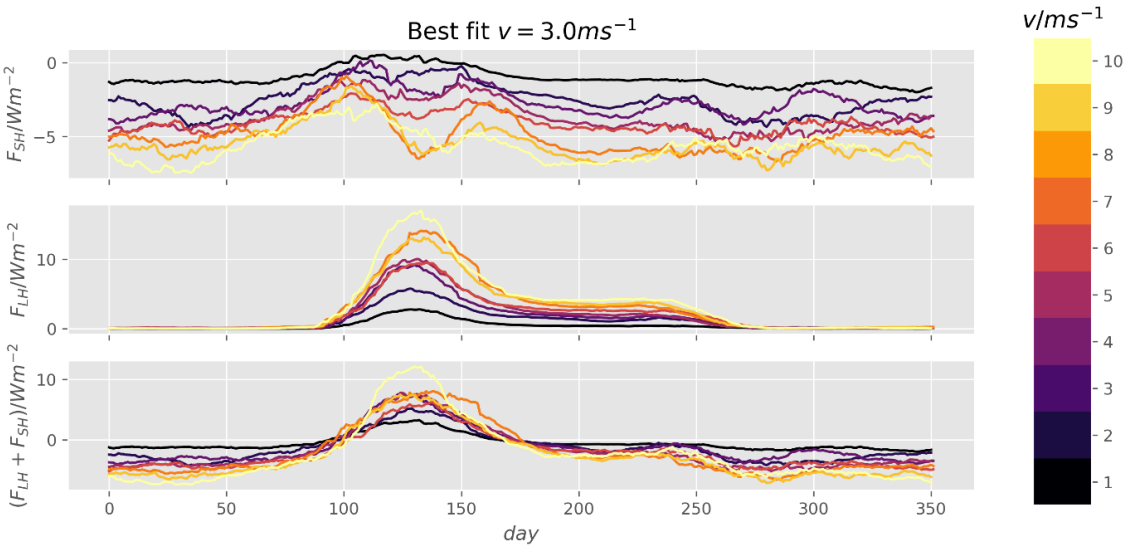


Figure 18 The sensitivity of surface sensible and latent heat fluxes, $F_{SH}$and F_{LH}, and their total to wind speed for the column model in a cloudless configuration. Run with 30 vertical levels.

4.1.3 Cloud parameters

I set the threshold temperatures T_{00} and T_0 at $250\ K$ and $273\ K$, approximately consistent with values used in the ECMWF IFS cloud scheme (ECMWF, 2023).

I set γ in the cloud area fraction parameterisation to 0.2 as in Le Treut and Li (1991). Figure 19 plots γ as calculated from ERA5 reanalysis data weighted by q_t. I area-weighted the reanalysis data and masked datapoints over land with zonally averaged over sea data. The distribution is bimodal with a peak just below 0.2 mainly driven by the lowest model level and a second broader peak centred on 0.5 for higher levels. This suggests a potential underestimation of γ in my model runs which would result in an underestimation of f when $f < 1/2$ and an overestimation when $f > 1/2$ (see Figure 16).

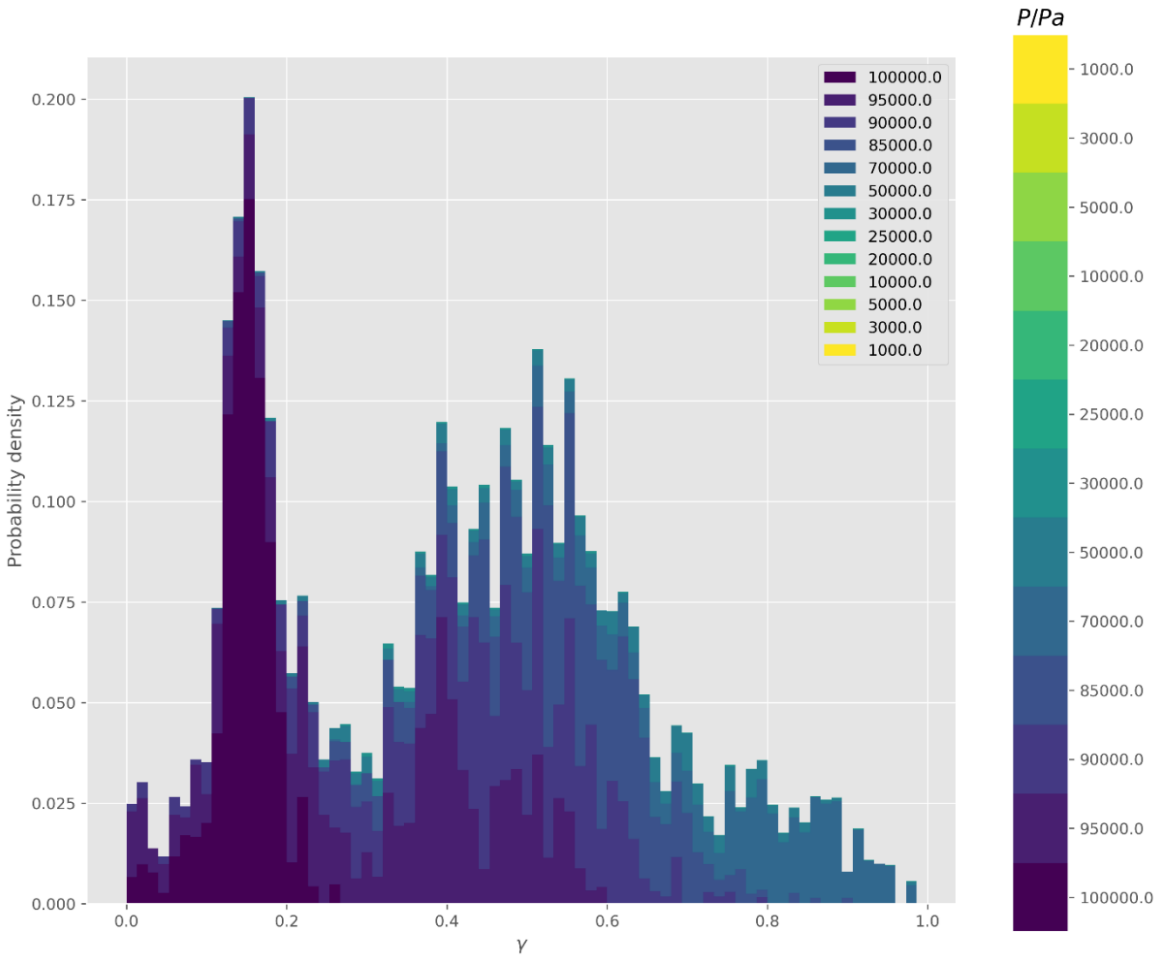


Figure 19 Stacked histogram showing γ values for the cloud area fraction parameterisation as calculated from area-weighted ERA5 reanalysis data over the Arctic. Data is weighted by the amount of total water, q_t, at each datapoint.

4.2 Comparison with reanalysis data

Figure 20 compares the steady state seasonal cycle of the SCM run in the default configuration outlined above to the average seasonal cycle from ERA5 reanalysis over the period 1979-2022 for the region $70 - 90\,°N$. To provide a good comparison with the SCM, I masked out land-covered regions of the reanalysis data and replaced them with the zonally averaged ocean-covered state profile.

The SCM shows broad agreement with reanalysis, capturing the overall structure of profiles of temperature, specific humidity and cloud liquid water. For pressures

greater than $\sim 500\ hPa$ the model broadly captures the structure of cloud ice and cloud fraction profiles, however at greater elevation it significantly overestimates these – modelling a high cloud layer not seen in reanalysis. This discrepancy in the highest model layers could be caused by inaccurate tuning of γ as discussed above. It is also possible the autoconversion equation (41) is insufficient to model the precipitation of ice at the low temperatures in these model levels. A high cloud layer like the one simulated here is also seen in CESM2 GCM simulations (McIlhattan, Kay and L'Ecuyer, 2020). Artificially removing this layer in the SCM only leads to a small change in the seasonal cycle of the net surface energy flux. Other than this the model shows a cold bias below $\sim 800\ hPa$ outside of summer, overestimates summer specific humidity and underestimates it throughout the rest of the year. It also shows much more pronounced temperature inversions than the reanalysis, though these are in agreement with other products (e.g. Devasthale et al., 2010) and are likely due to low vertical resolution in the reanalysis data.

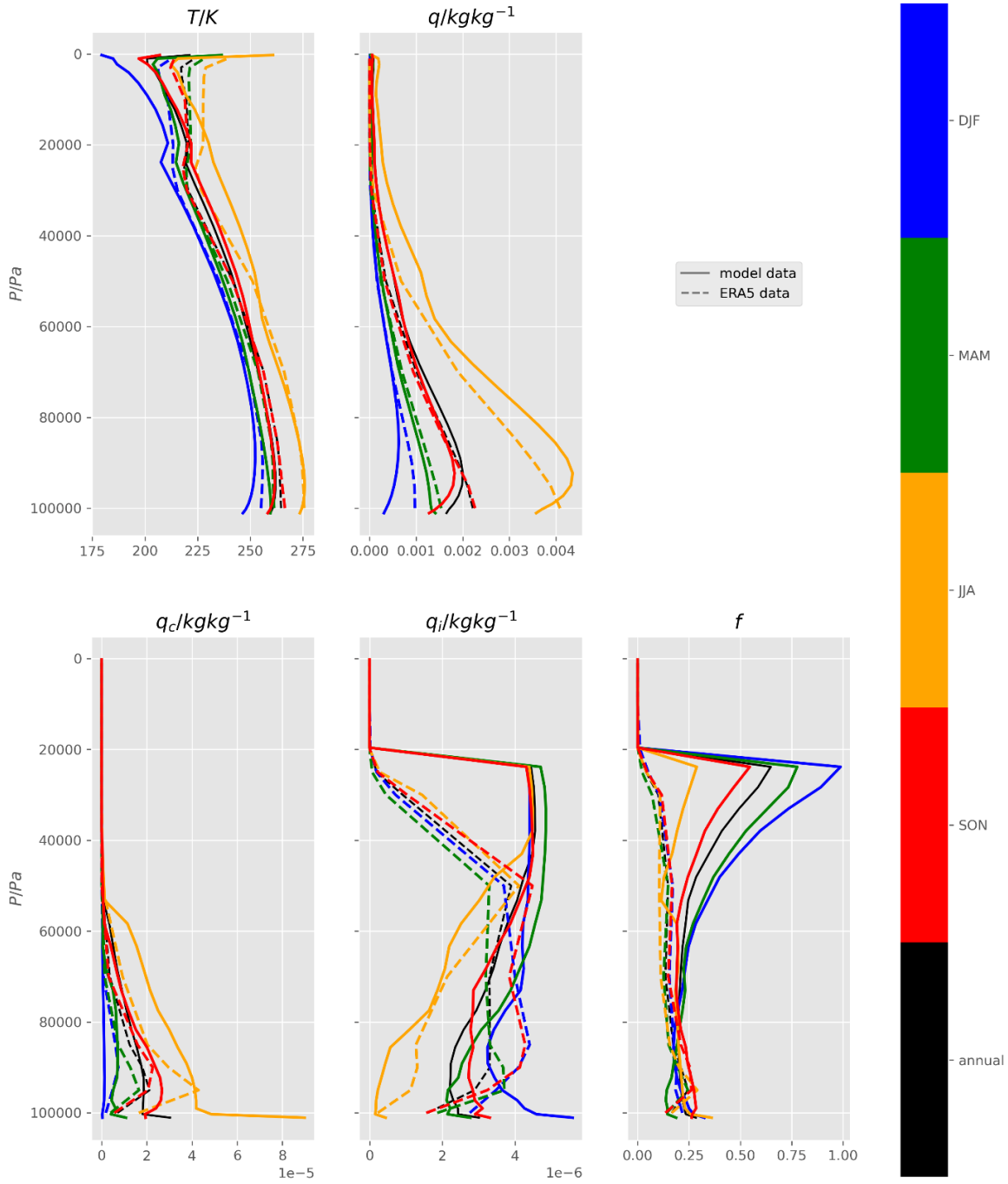


Figure 20 Comparison of seasonal mean profiles (coloured lines) and annual mean profiles (black lines) of air temperature, T, specific humidity, q, cloud liquid water mixing ratio, q_c, cloud ice mixing ratio, q_i, and cloud area fraction, f, for the column model in steady state (solid lines) and ERA5 data (dashed lines). The ERA5 data is the area weighted mean north of $70\,°N$ after data over land has been masked with the zonal mean of data over ocean.

5 Summary

In this chapter I provided a broad overview of key features of the Arctic atmospheric climate, going into detail on its vertical atmospheric structure, clouds and heat transport. I then outline how I represent these processes in a single column model (SCM) of the Arctic atmosphere so that the effect of these features and changes in them on sea ice can be resolved. The aim of this is to improve understanding of how these features affect the bifurcation structure of Arctic sea ice. The SCM overall shows good agreement with reanalysis data, though has a cold bias in winter and has anomalous high cloud cover that disagrees with ERA5 reanalysis, but is replicated in a GCM simulation.

It is important to note that there are many important features of Arctic climate not resolved in this model. These include features of the ice cover such as snow layers and melt ponds, and partial ice coverage. The model also lacks a representation of ocean heat transport or feedbacks in horizontal heat transport. I also assume a completely sea-covered Arctic which neglects the effect of land-covered regions.

Results of experiments exploring the bifurcation structure of Arctic sea ice using this model are presented in the next two chapters.

Chapter 4 Local atmospheric processes

1 Introduction

In this chapter I use the single column model (SCM) of the Arctic atmosphere and sea ice surface outlined in the previous chapter to explore the effect of local atmospheric feedbacks on bistability in Arctic sea ice cover.

The SCM is constructed using the climt modular framework (Merwin Monteiro, McGibbon and Caballero, 2018) using the RRTMG radiation scheme (Clough *et al.*, 2005), Emanuel convection scheme (Emanuel and Živković-Rothman, 1999), SimplePhysics boundary layer scheme (Reed and Jablonowski, 2012) and additional components I created for a mixed-phase saturation-adjustment cloud scheme, atmospheric heat transport tendencies derived from Cardinale *et al.* (2021), and slab sea ice scheme from Eisenman and Wettlaufer (2009). A key feature of the SCM is its ability to resolve changes in the lapse rate of the Arctic and surface amplification associated with this (e.g. Payne, Jansen and Cronin, 2015).

The aim of the work in this chapter is to explore how features resolved in this model that aren't included in intermediate complexity models discussed in chapter 1 affect the system's bifurcation structure. I begin by considering the model in a clear sky configuration and explore how the model's vertical temperature structure affects bistability. I then explore the effect of clouds on bistability. I finish off by exploring the system's response to different atmospheric heat transport compositions and structures.

1.1 An important note

The work presented in this chapter (and throughout this thesis) is not intended to be predictive. The SCM makes a number of simplifications in its representation of Arctic climate – notably the lack of resolved atmospheric heat transport. The aim of this work is to illustrate how the interlocking systems present in its formulation affect the bifurcation structure of the Arctic.

2 The clear sky column model

In this section I present results of the model in a clear sky configuration and discuss the effect of a resolved vertical temperature profile on the system's bifurcation structure. In this configuration humidity is regulated by a large scale condensation scheme that instantly precipitates any moisture above saturation to the surface.

2.1 Bifurcation structure

Figure 21 presents the stable states found in the clear sky model configuration. In this and all similar figures stable state seasonal cycles of the model are marked by pairs of points joined by a vertical line (indicating the range of surface energy density, E, values occupied during the seasonal cycle). Perennially ice-free states are marked in red, perennially ice-covered states in blue, and seasonally ice-free states in grey. E values are marked on the right-hand y axis and the equivalent h and T_{ml} values on the left-hand y axis.

I found stable states of the model by initiating it with a range of ice-covered and ice-free initial conditions ($-1\ GJm^{-2}$, $-0.5\ GJm^{-2}$, $0\ GJm^{-2}$, $0.5\ GJm^{-2}$, $1\ GJm^{-2}$) for a range of atmospheric carbon dioxide concentrations, $[CO_2]$, and allowing it to converge to an approximately stable state. The seasonally ice-free grey state (discussed below) is only stable for a very thin range of carbon dioxide concentration concentrations. I tested for the width of this section by initiating the model with the seasonally ice-free states with the lowest (highest) carbon dioxide concentration and

decreasing (increasing) the concentration by a small increment and repeating until the system exited the seasonal branch. This state was robust even when the steady state threshold for the model was increased.

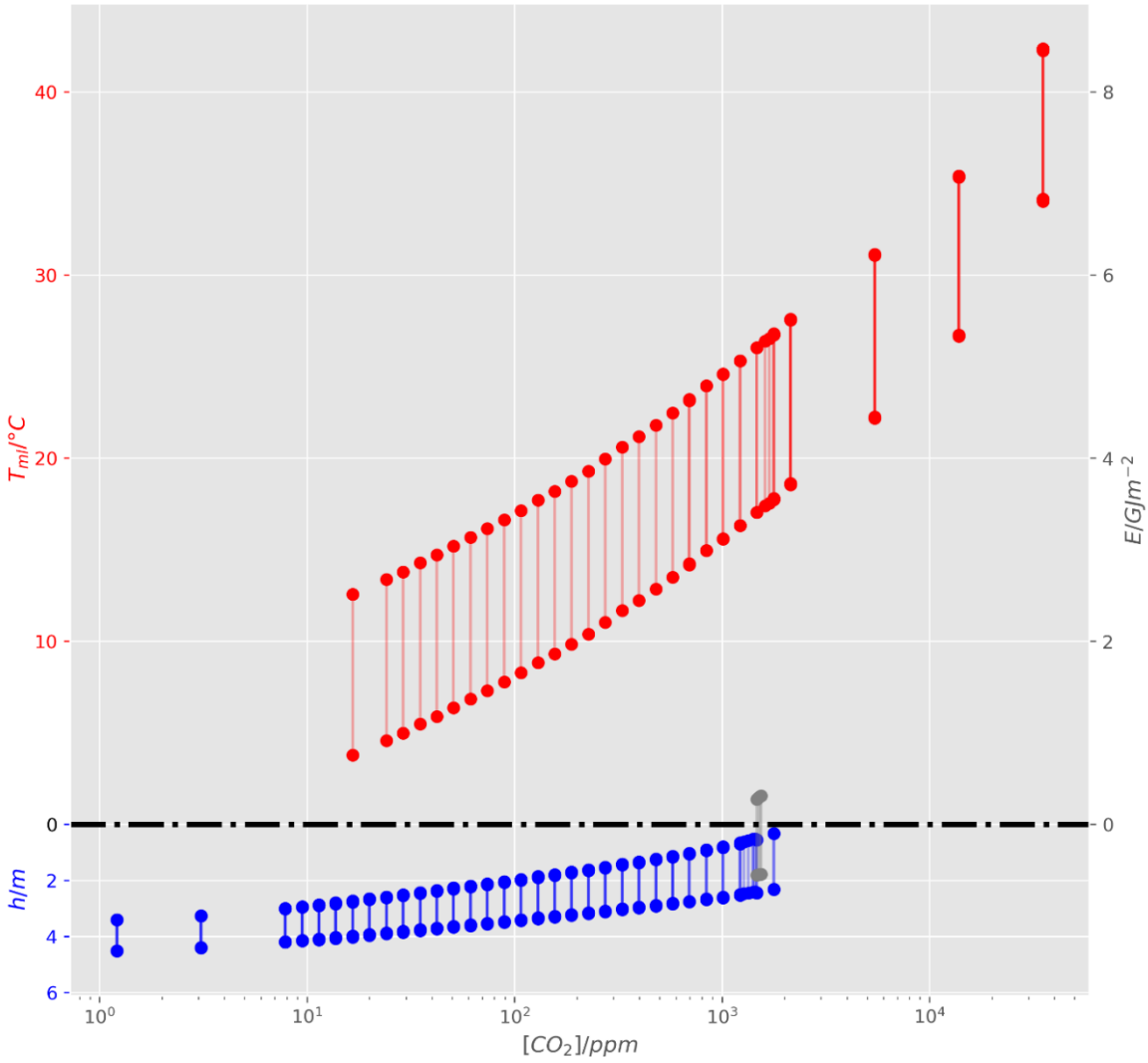


Figure 21 Stable states of the clear sky SCM for different atmospheric carbon dioxide concentrations, $[CO_2]$. Stable states are represented by pairs of points joined by a vertical line. The upper and lower points represent the extreme values of the energy density coordinate, E, for the seasonal cycle. The vertical line covers the range of E values in the seasonal cycle. Blue data represents perennially ice-covered states, grey data seasonally ice-free states and red data perennially ice-free states. E values are given on the right-hand y-axis and converted to equivalent sea ice thickness, h, and mixed layer temperature, T_{ml}, values on the left-hand y-axis.

In this configuration the model can exist in three distinct stable states: a perennially ice-covered state (blue) bounded by a bifurcation point at an upper $[CO_2]$ bound; a perennially ice-free state (red) bounded by a bifurcation point at a lower $[CO_2]$

bound; and a seasonally ice-free state (grey) bounded by bifurcation points at lower and upper $[CO_2]$ bounds. The seasonally ice-free state is only stable for an extremely small range of atmospheric CO_2 concentrations. It is also contained entirely between the bifurcation points of the perennially ice-covered and ice-free states (in a small region where the system is *tristable*). In practice, if the system was initially in one of the perennially ice-covered or ice-free states and evolved smoothly and slowly such that it underwent *bifurcation-induced tipping* the system would collapse into the alternative perennial state without ever occupying the seasonal state. The system can only ever transition into a 'sandwiched' state like this if it is pushed out of the attracting range of an adjacent stable state in noise-induced or rate-induced tipping. When in the grey seasonally ice-free branch and the system undergoes bifurcation-induced tipping by increasing (decreasing) $[CO_2]$ the system then collapses into the perennially ice-free (ice-covered) branch.

Another striking feature of the bifurcation structure of Figure 21 is the width of the bistable region. In particular, the perennially ice-free state is stable for extremely low atmospheric CO_2 concentrations, well below 100 ppm. The lack of atmospheric heat transport feedbacks in the model is likely the most significant contributor to this as this would significantly reduce the energy input to the model when ice-free. Thorndike (1992b) find a similar bifurcation structure with abrupt loss of winter sea ice in a much simpler toy model without heat transport feedbacks, suggesting heat transport is an important controlling factor for the bifurcation structure of the system. In their study, Eisenman and Wettlaufer (2009) include a parameterised heat transport feedback and find a much smaller bistable window with a smooth transition from a perennially ice-covered to a seasonally ice-covered state. While the results of this model are far beyond what would be expected of the Arctic in reality, it is a useful tool to understand the impact of individual features of the climate system.

Figure 22 shows the seasonal mean temperature profiles of the model for each stable state for $[CO_2] = 1472\,ppm$ in the tristable region. There is a marked difference in atmospheric structure between the states. The perennially ice-covered (blue) and seasonally ice-free (grey) states are convectively stable throughout the year. However, the perennially ice-free state (red) is convectively active and roughly follows a moist adiabat in the lower troposphere throughout the year as for a system in radiative-convective equilibrium. I discuss this further in the next subsection. Perenially ice-covered and perennially ice-free states outside of the tristable range have a similar temperature structure to the states shown in this figure. For larger CO_2 concentrations convection is deeper in the perennially ice-free state and for lower CO_2 concentrations it is shallower. Similarly, for larger CO_2 concentrations the winter temperature inversion is weaker and for lower CO_2 concentrations it is stronger.

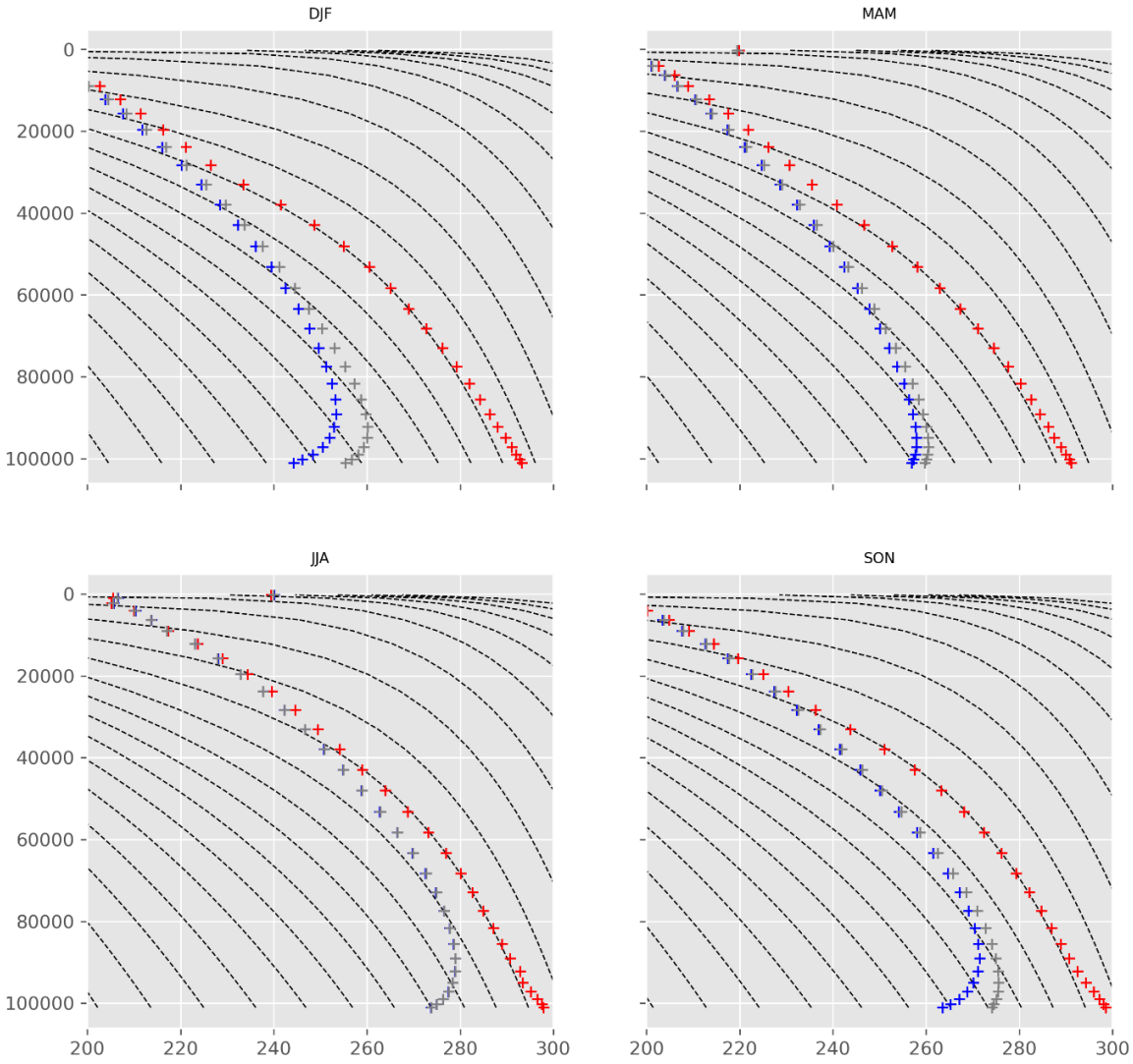


Figure 22 Seasonal mean temperature profiles of steady states of the clear sky SCM for the perennially ice-covered (blue +'s), seasonally ice-free (grey +'s), and perennially ice-free (red +'s) states with atmospheric CO_2 concentration of $1472\ ppm$. *Moist adiabats are plotted in black dashed lines. In lower left panel grey +'s lie on top of blue +'s.*

2.2 The effect of vertical structure

In chapter 3 I outline two states an atmospheric column can exist in – radiative-advective and radiative-convective equilibrium. In radiative-convective equilibrium longwave cooling of the atmosphere is primarily balanced by a combination of shortwave and convective warming; whereas in radiative-advective equilibrium the atmosphere is stable with regard to convection and longwave cooling is primarily balanced by a combination of shortwave warming and horizontal advection of heat.

When responding to an increase in concentration of longwave absorbers, e.g. CO_2, atmospheres in *radiative-convective equilibrium* are characterised by approximately vertically uniform warming, strongest in the upper troposphere. On the other hand, atmospheres in *radiative-advective equilibrium* undergo significantly surface-amplified warming (Figure 23) (Payne, Jansen and Cronin, 2015).

Representing the vertical structure of the atmosphere in the SCM allows this surface amplification effect to be resolved. This cannot be done in the 0-dimensional models discussed in chapter 1 where a single coordinate is used to represent the model state.

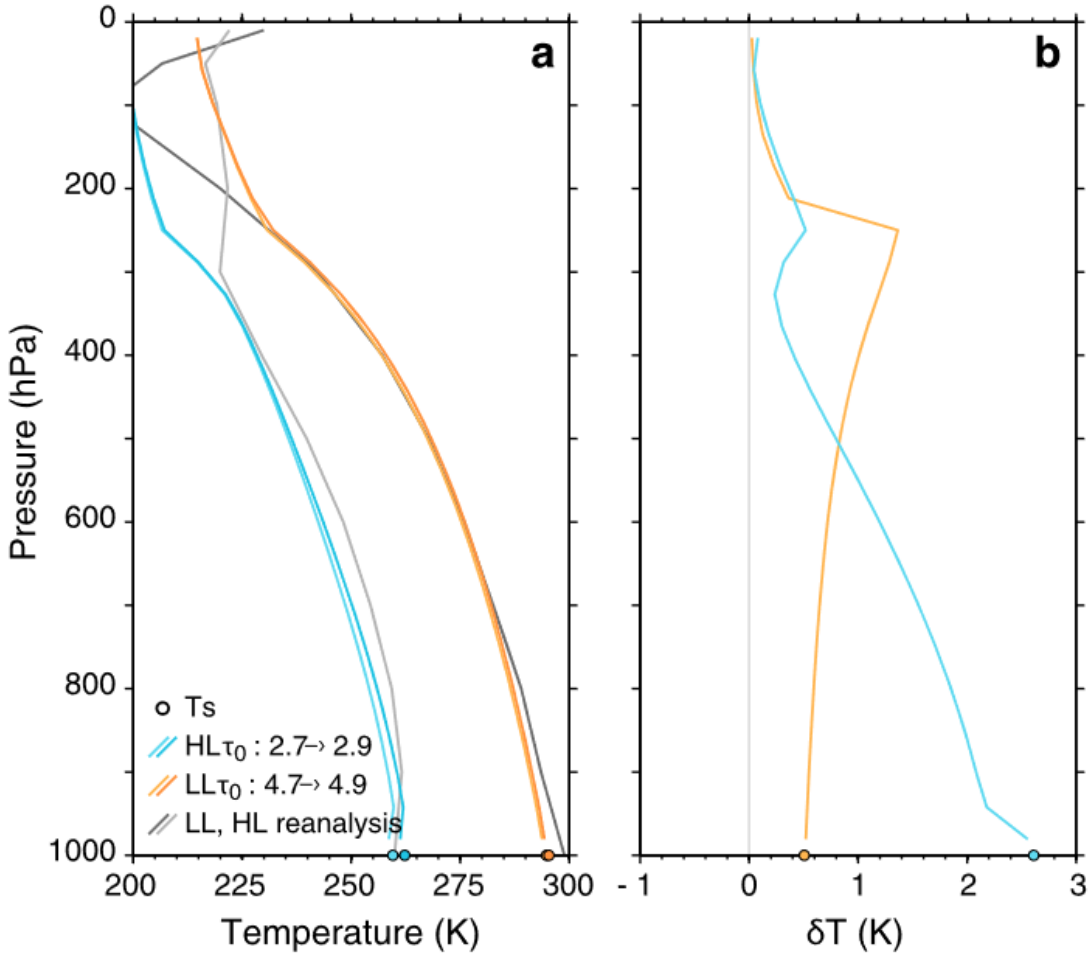


Figure 23 Panel a) shows the temperature response for an increase in column optical depth, τ_0, of 0.2 for a column in radiative-advective equilibrium (orange, termed LL for low latitude) and radiative-advective equilibrium (blue, termed HL for high latitude). Comparison profiles from reanalysis are plotted in grey. The

radiative-advective equilibrium profile has a characteristic temperature inversion. Panel b) shows the temperature difference, δT, after the increase in τ_0. From Payne, Jansen and Cronin (2015).

Bintanja, Graversen and Hazeleger (2011) demonstrate that this surface amplification of warming is stronger for larger surface temperature inversions. To explore the effect the vertical temperature structure within the SCM has on the stability of ice-covered states (where the system is convectively stable and approximately characterised by radiative-advective equilibrium) I conducted a series of runs where I perturbed the strength of mixing by turbulent heat fluxes. I did this by multiplying the drag coefficient for turbulent heat fluxes in the SimplePhysics scheme by a constant parameter. When the coefficient is multiplied by a factor greater than 1 surface mixing increases, decreasing the temperature inversion strength, and when less than 1 it increases the inversion strength. While these perturbations to surface mixing modify the partitioning of energy between the atmosphere and surface, they make no change to the input of energy into the system.

Figure 24 plots the results of these experiments. The upper panel plots the annual mean temperature inversion for a given mixing factor and the lower panel plots the atmospheric CO_2 concentration, $[CO_2]$, at which the ice-covered state ceases to be stable.

As expected, increasing surface mixing reduces the strength of the atmospheric temperature inversion. Increasing surface mixing also initially stabilises the ice-covered state for greater CO_2 concentrations, in line with results from Bintanja, Graversen and Hazeleger (2011). However, for mixing factors greater than 4 the ice-covered state doesn't stabilise any further within the resolution of my experiments. Moreover, the ice-covered state transitions to an ice-free state at a slightly *lower* atmospheric CO_2 concentration for a mixing factor of 10 compared to

a mixing factor of 8. The mechanism for this plateau and slight reversal in trend is uncertain.

Despite these ambiguities, these results clearly illustrate that the stability of the ice-covered states is sensitive to the partitioning of energy into atmosphere and surface – something not represented in simple models without an atmospheric component.

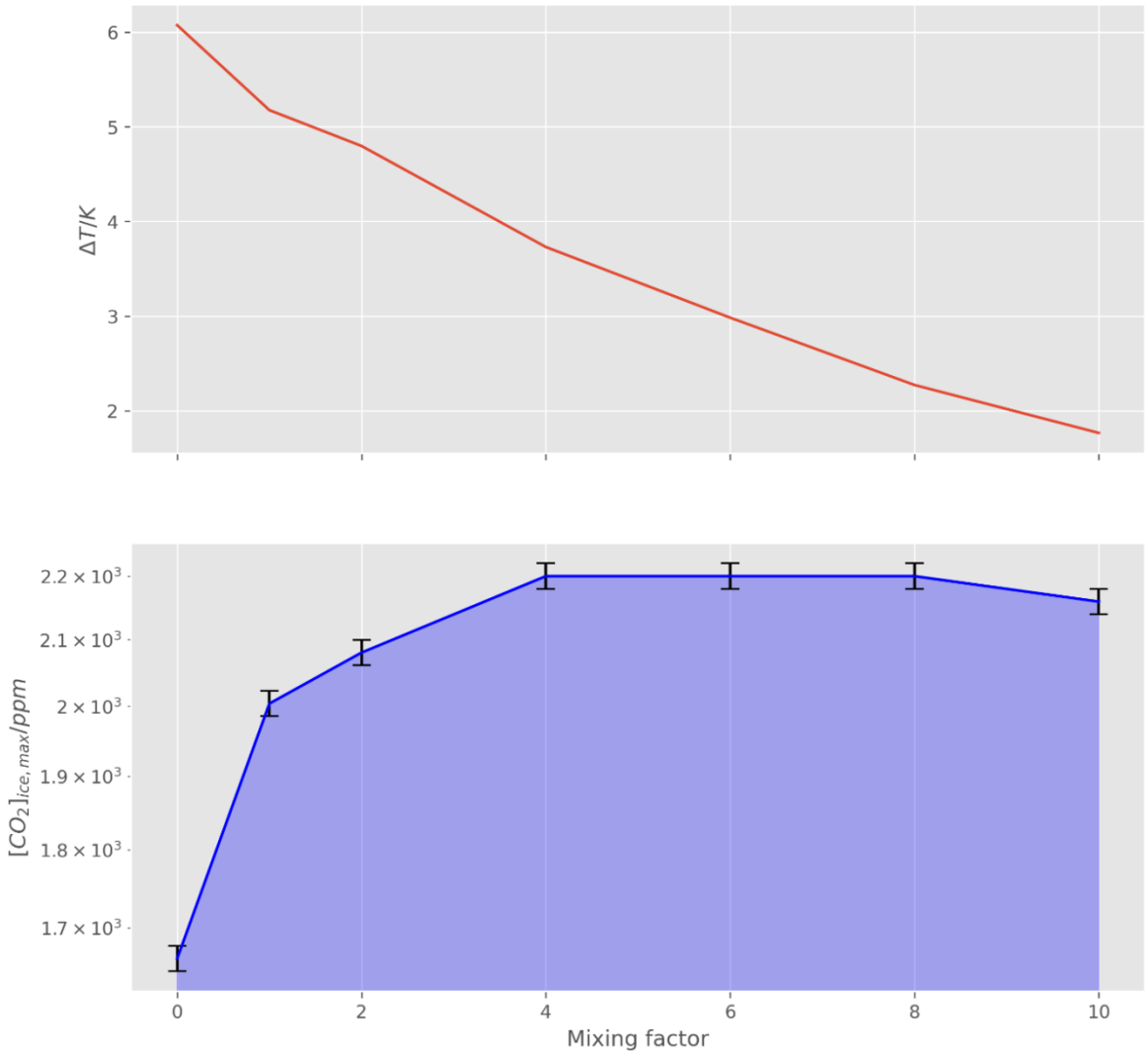


Figure 24 Bottom panel shows the atmospheric CO_2 concentration, $[CO_2]$, at which the ice-covered state ceases to be stable when turbulent heat fluxes are multiplied by a given mixing factor (blue line with black error bars). The blue region marks CO_2 concentrations where the ice-covered state is stable. For a mixing factor of 0, there is no turbulent heat exchange. Top panel shows the annual mean temperature inversion, ΔT, of the atmospheric column for a given mixing factor.

3 The cloudy column model

In this section I present results of the SCM using the cloud scheme as outlined in Chapter 3. I use two different methods of representing cloud area fraction, f, due to the difficulty in parameterising this quantity: using the contemporary cloud area fraction profile taken from ERA5 reanalysis data over the period $1979 - 2022$ and using a parameterisation outlined in Chapter 3 modified from Le Treut and Li (1991).

Figure 25 shows steady state profiles of the effective cloud (calculated as the product of cloud area fraction and total cloud water) for the SCM using the ERA5 cloud area fraction and parameterised cloud area fraction in perennially ice-covered (blue) and perennially ice-free (red) states for atmospheric CO_2 concentrations of $330\ ppm$ (solid lines) and $840\ ppm$ (dashed lines). The configurations have two main differences. The parameterisation consistently represents a much more pronounced layer of high clouds. Secondly, the parameterisation can show changes in f as the model state changes, whereas the ERA5 profile remains fixed. Notably, the layer of low clouds in the ice-covered state disappears in the ice-free state for parameterised cloud area fraction and a thick cloud layer forms near $60{,}000\ Pa$. The thicker layer of low clouds when the system is ice-covered can loosely be explained by the fact that there is the same moisture transport into the column when ice-covered and ice-free, and when the system is ice-free the saturation specific humidity is lower and the column is convectively stable increasing the condensable water available to form low clouds. Figure 25 also shows profiles of air temperature and specific humidity. Resolving clouds weakens the temperature inversion seen in the perennially ice-free state.

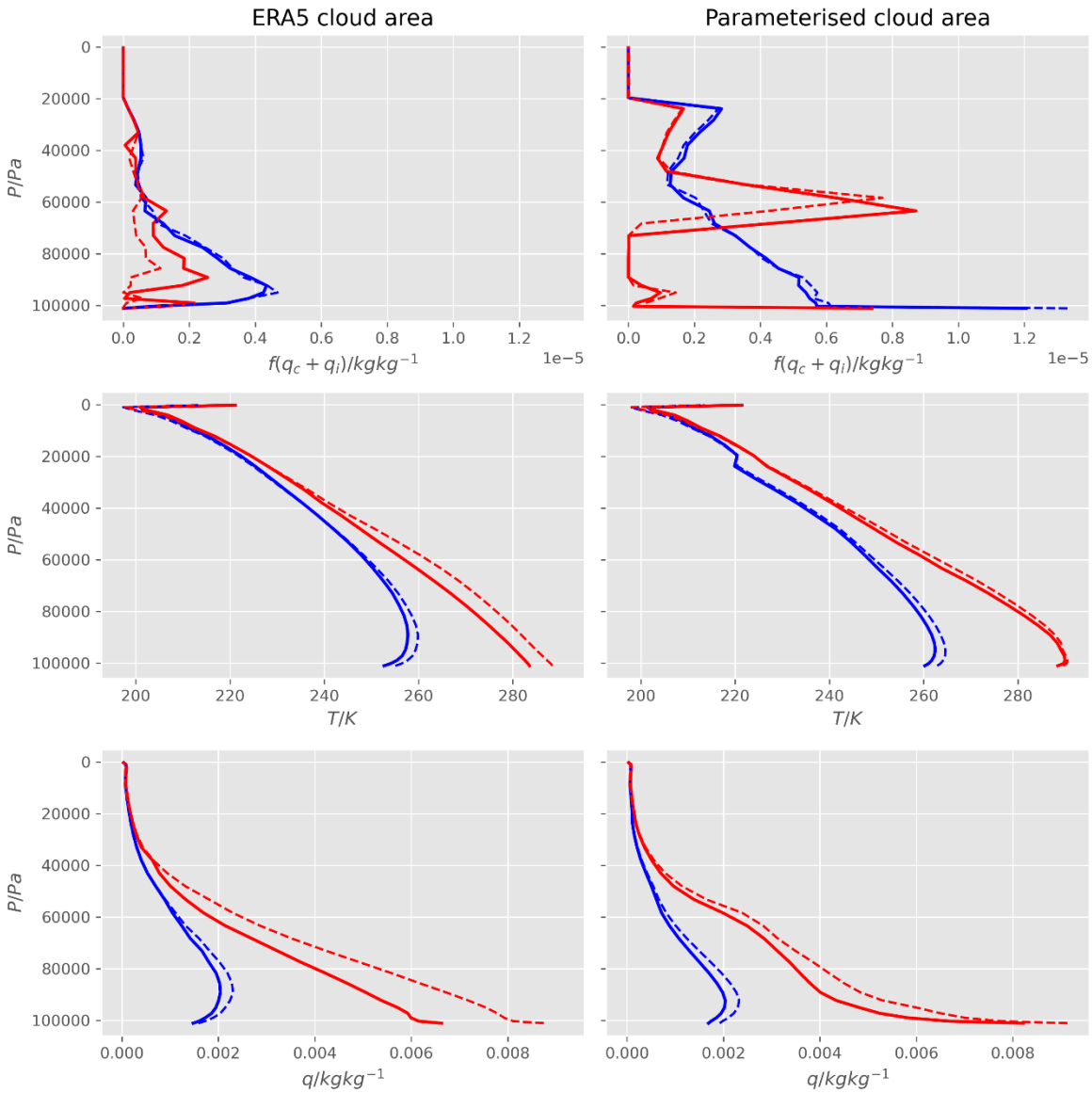


Figure 25 Comparison of SCM profiles using the ERA5 cloud area fraction (left) and parameterised cloud area fraction (right) for perennially ice-covered (blue) and perennially ice-free (red) states. Profiles shown are annual means of: effective cloud (top row), air temperature (middle row), and specific humidity (bottom row). Solid lines correspond to the steady state of the model with $330\ ppm$ *CO_2 and dashed lines for* $840\ ppm$*. Effective cloud is calculated as the product of cloud area fraction and total cloud water,* $f(q_c + q_i)$*.*

The impact of these differences in cloud area representation are illustrated in Figure 26. Here the left-hand column shows the stable states of the SCM (as in Figure 21) when parameterised cloud area fraction is used (top row) and when the fixed ERA5 area fraction is used (middle row). The right-hand column shows the annual mean net surface cloud radiative effect for each stable state of the model.

Both configurations exhibit roughly the same qualitative structure as the clear sky configuration – perennially ice-covered (blue) and ice-free (red) states that cease to be stable before becoming seasonally ice-free. Surprisingly, in my experiments I also found stable seasonally ice-free (grey) states for the ERA5 cloud area fraction configuration in two $[CO_2]$ regions – it is possible that these both exist on the same branch of states. Surprisingly, the surface energy density, E, of these states *decreases* as $[CO_2]$ increases. This is characteristic behaviour of unstable states in systems with saddle-node bifurcations, however these states appear to be stable to perturbations. It is possible that the increased complexity of the cloud scheme modifies the system's stability structure to create an additional stable state in the vicinity of the canonical saddle-node unstable state, while still retaining the same overall structure. It is also possible that these are states on the unstable branch which have been stabilised due to numerical error in the model. However, the mechanism for this is unclear. I don't see similar behaviour in any other configuration, though this could be because of the limited resolution of my model runs.

There are clear differences between the perennially stable states of the parameterised cloud area fraction configuration and the ERA5 cloud area fraction configuration. In the ERA5 configuration the perennially ice-covered state ceases to be stable at a much higher CO_2 concentration and in the parameterised configuration the perennially ice-free state ceases to be stable at a much lower CO_2 concentration. Overall the bistable window is slightly wider in the parameterised configuration.

The higher bifurcation point of the ice-covered branch in the ERA5 configuration is driven by a significantly less positive surface cloud radiative effect. In both configurations there is a slight negative feedback as the cloud radiative effect decreases with increasing $[CO_2]$. This is much stronger with parameterised cloud

area fraction and means the rate of decrease in ice thickness with increasing $[CO_2]$ is slower.

The increased stability of the ice-free branch in the parameterised configuration can also be explained in terms of cloud feedbacks. Here there is a clear strong negative feedback on the cloud radiative effect when $[CO_2]$ is increased between $10^1 - 10^3\ ppm$. This means that for a perennially ice-free state in this region, when $[CO_2]$ is *reduced* there is an increase in the warming effect of clouds that stabilises the surface temperature. This explains why surface temperature is less sensitive to changing $[CO_2]$ for the perennially ice-free state in this region. On the other hand, the ERA5 configuration doesn't exhibit any strong feedback on cloud radiative effect with increasing $[CO_2]$ and its ice-free state has a steeper gradient with increasing $[CO_2]$.

In addition, I conducted a series of similar experiments using the cloud area fraction parameterisation with only low cloud formation allowed and a maximum cloud height of $550\ hPa$. I used the low cloud criteria of cloud base height $< 1{,}980\ m$. The results of these experiments are shown in the bottom row of Figure 26. Like the ERA5 configuration, there is no strong feedback on cloud radiative effect with increasing $[CO_2]$ in the perennially ice-free state. This indicates that the source of the negative feedback is from higher clouds resolved by the parameterisation. This is illustrated in Figure 27. For lower CO_2 concentrations along the perennially ice-free branch there is a thicker region of upper tropospheric clouds which provide a warming effect on the surface that disappear as $[CO_2]$ increases, similar to the stabilising high clouds seen in Abbot and Tziperman (2008) though at a lower altitude. As these clouds disappear the annual mean surface cloud radiative effect goes from being net positive to net negative.

It is also notable that in this low cloud configuration the perennially ice-covered state remains stable at higher atmospheric CO_2 concentrations than either of the other configurations. This is driven by a particularly strong negative feedback on the cloud radiative effect with increasing $[CO_2]$.

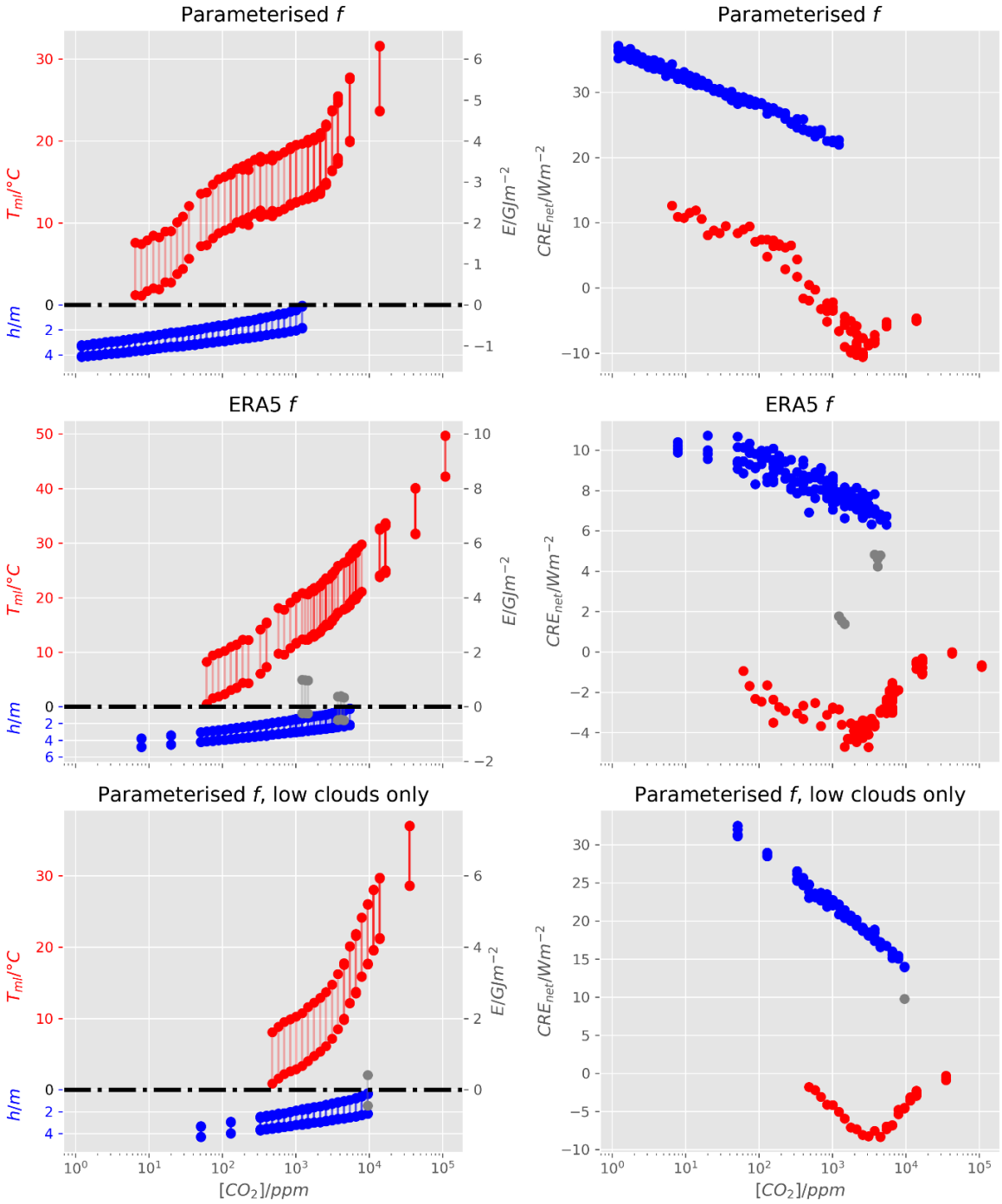


Figure 26 Graphs showing the surface state (left) and net surface cloud radiative effect, CRE_{net}, (right) of steady states of the SCM using the cloud area fraction parameterisation (top row), ERA5 cloud area (middle row) and parameterised low clouds only (bottom row). The left-hand diagrams showing the steady state of the model

surface are constructed as in Figure 21. The right-hand diagrams plot the annual mean net surface cloud radiative effect for each datapoint in the left-hand diagrams. As in Figure 21 blue points represent perennially ice-covered states, red points perennially ice-free states, and grey seasonally ice-free states. Notably, the system contains a bifurcation point associated with the destabilisation of a perennially ice-free state..

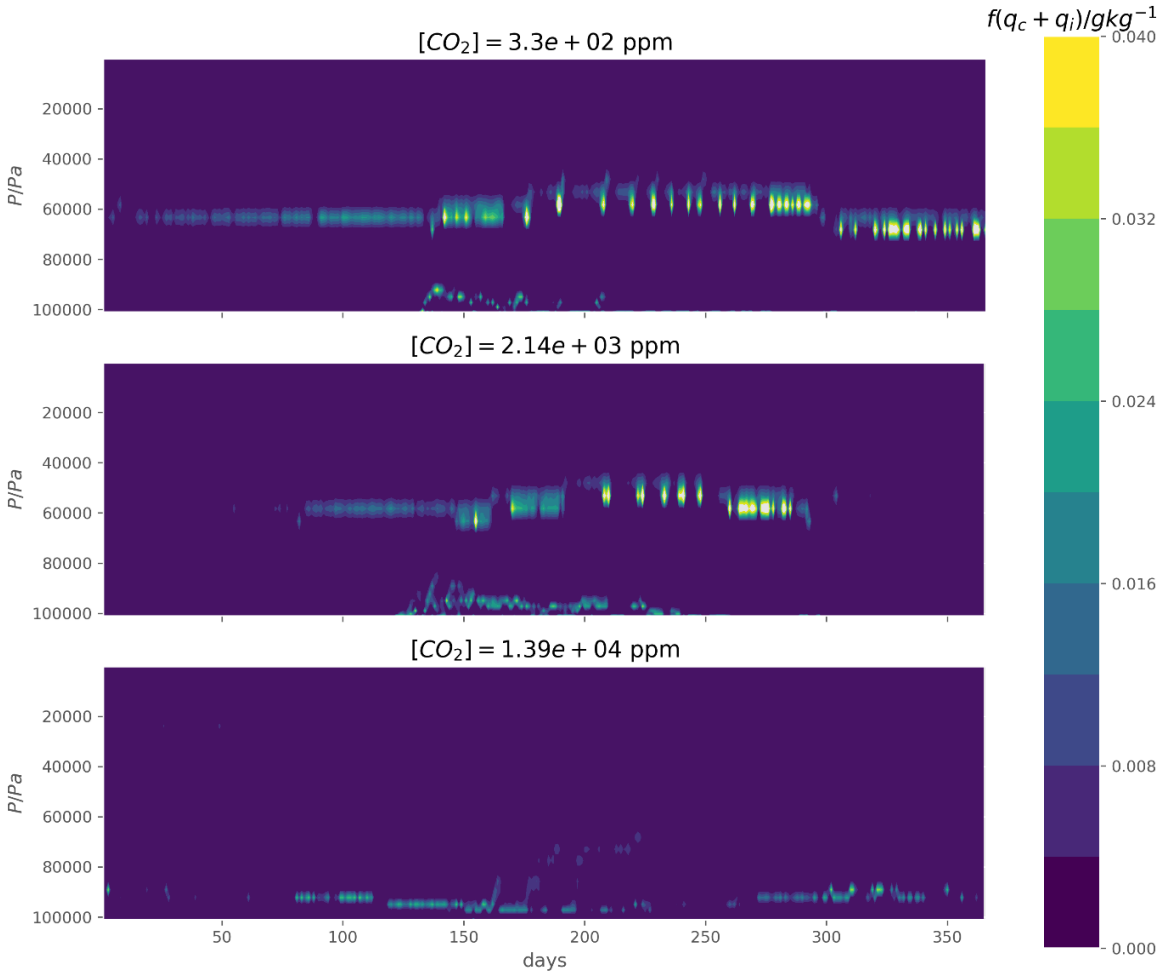


Figure 27 Effective cloud cover (calculated as the product of cloud area fraction, f, and total cloud water, $q_c + q_i$), for perennially ice-covered states using parameterised cloud fraction (same configuration as the top row of Figure 26) for 3 atmospheric CO_2 concentrations, $[CO_2]$, evenly distributed in log space. There is a decrease in the coverage of high tropospheric clouds as $[CO_2]$ increases.

These results indicate a stabilising effect of high clouds on ice-free states which could act to strengthen bistability in the system. However, potential biases in favour of high clouds in the area fraction parameterisation make the strength of this effect uncertain.

These results also imply a stabilising effect of low clouds on the perennially ice-covered state. Comparing the perennially ice-covered branches of the low cloud only configuration to the clear sky configuration (Figure 21), it is clear that the ice-covered state ceases to be stable at higher atmospheric CO_2 concentrations when low clouds are resolved. This appears to be partially driven by a stronger negative feedback in the surface cloud radiative effect for increasing $[CO_2]$ in this state – indicated by the much steeper decline in the surface cloud radiative effect as atmospheric CO_2 concentrations increase on this branch. Another potentially important factor for this stabilisation is the weakening of the temperature inversion caused by low clouds reducing the warming efficiency at the surface.

4 Sensitivity to heat transport structure

Finally, to demonstrate the system's sensitivity to different kinds of forcing I conducted a set of experiments probing the SCM's bifurcation structure when perturbed with different constant atmospheric heat fluxes with atmospheric CO_2 held constant.

Models without a resolved atmosphere don't resolve features such as the vertical structure of atmospheric heat fluxes or its composition. To explore the effects of these features I found stable states for the system when forced with atmospheric heat transport with varying composition and vertical structure. Each forcing perturbation to the column model, F, has vertical profile, Q, defined by a power law:

$$F = \int_0^{p_S} Q(p)dp \tag{56}$$

$$Q(p) = n\frac{F}{p_S}\left(\frac{p}{p_S}\right)^{n-1} \tag{57}$$

where p is the air pressure and p_s the surface air pressure. For greater values of the exponent n the heat transport is more heavily weighted towards the surface.

I found stable states of the model for the following perturbations:

1. Dry atmospheric heat transport, $n = 1$.
2. Dry atmospheric heat transport, $n = 2$.
3. Moist atmospheric heat transport, $n = 2$.

In each case the system was run in a cloudy configuration using the cloud area fraction parameterisation. The results are plotted below in Figure 28.

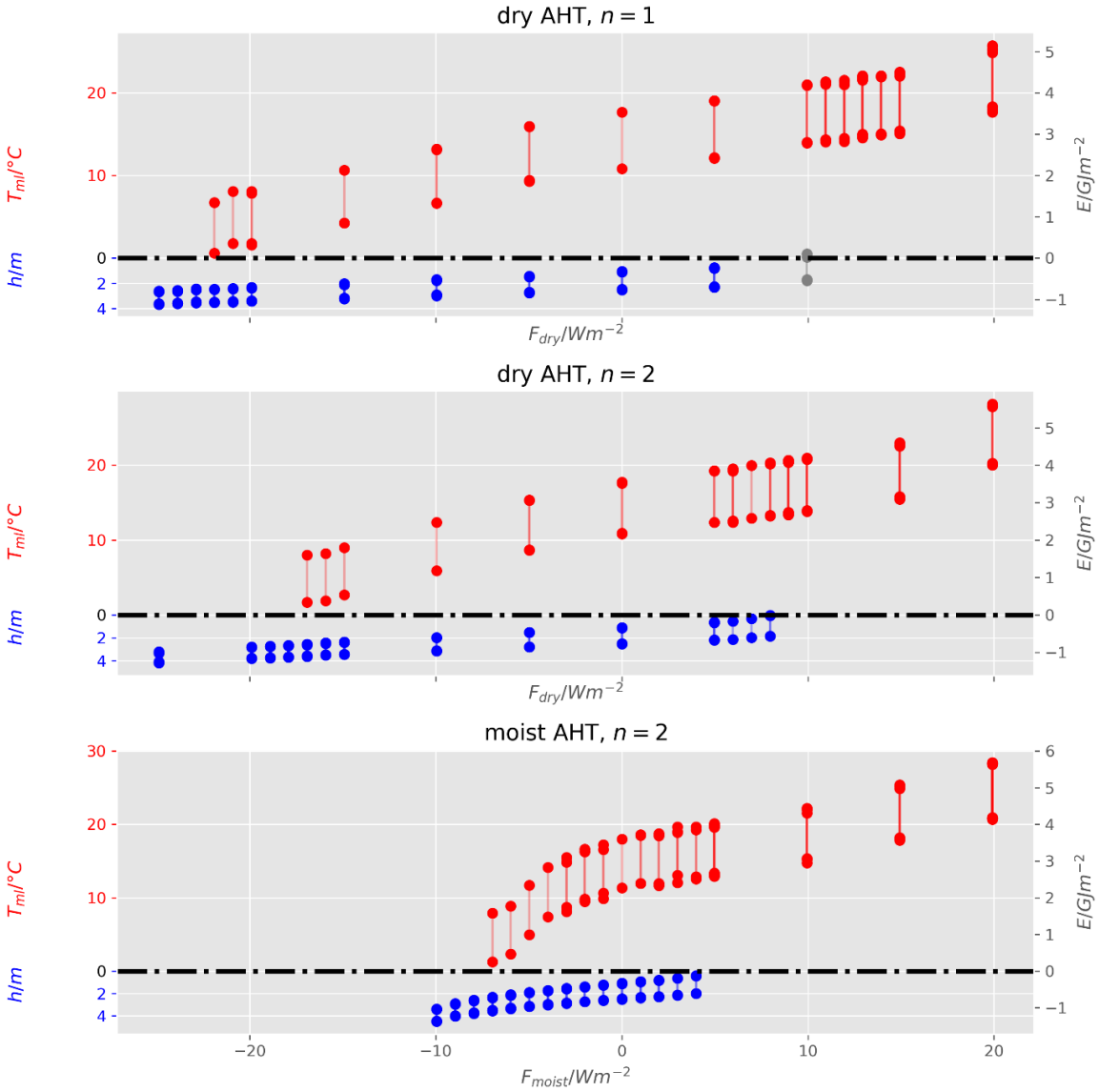


Figure 28 Stable states for the SCM with constant atmospheric CO_2 when forced with additional atmospheric heat transport, plotted as in Figure 21. The SCM is run with the cloud scheme using the cloud area fraction parameterisation. Top panel shows results for dry additional heat transport with power law parameter $n = 1$;

middle panel for dry additional heat transport with $n = 2$; and bottom panel for moist additional heat transport with $n = 2$.

When the dry heat transport perturbation is made more bottom heavy by increasing the power law exponent, n, from 1 to 2, the width of the bistable region decreases. This is driven by the more surface heavy heat transport being more effective at warming the surface (and more effective at cooling when negative). This means that the ice-covered state ceases to be stable at a lower perturbation and the ice-free state at a higher perturbation.

There is an even stronger difference when the system is forced with perturbations to latent heat transport. The bistable window is less than half the size as for the dry equivalent with the same vertical profile. This is due to the twofold warming effect of latent heat transport due to longwave emission of water vapour and clouds. The steep decline seen in ice-free surface temperatures near the bifurcation point is driven by the gradual disappearance of low cloud cover with decreasing F_{moist} and a consequent weakening of the surface cloud shortwave effect.

These results demonstrate that changes in the vertical structure and composition of atmospheric heat transport can have significant effects on the bistability of the system. As these features can't be resolved in simple models without a resolved atmosphere such as Eisenman and Wettlaufer (2009) they can't account for these effects.

5 Conclusions

In this chapter I present results showing the bistability structure of Arctic sea ice in a single column model (SCM) resolving the Arctic atmosphere coupled to a slab thermodynamic model of sea ice.

I first consider the clear sky configuration of the model and find three stable states: perennially ice-covered and perennially ice-free states that cease to be stable at upper and lower bounds of atmospheric CO_2 respectively; and a seasonally ice-free state stable for a very thin range of atmospheric CO_2 concentrations between these bifurcation points. Notably, in this configuration – and all other configurations in this chapter – there is a bifurcation associated with the loss of summer sea ice. When passed in a bifurcation-induced tipping event the system immediately transitions to a perennially ice-free state. This is in contrast to results seen in Eisenman and Wettlaufer (2009) and is possibly due to the lack of resolved atmospheric heat transport feedbacks. Strikingly, these results (and others in this chapter) show a broad region of bistability extending well below contemporary CO_2 levels. This is likely driven by the lack of atmospheric heat transport feedbacks stabilising warmer ice-free states.

In the perennially ice-free state the system is close to radiative-convective equilibrium, whereas in the perennially ice-covered state it is close to radiative-advective equilibrium and has a strong temperature inversion. Following work showing surface-amplified warming and sensitivity to vertical temperature profiles in systems in radiative-advective equilibrium (Bintanja, Graversen and Hazeleger, 2011; Henry *et al.*, 2021) I tested the stability of the perennially ice-covered state for model states with weaker inversions due to increased surface mixing. These results demonstrate that for stronger surface mixing the temperature inversion strength decreases and the atmospheric CO_2 concentration of the bifurcation point of the perennially ice-covered branch *increases* but plateaus while the temperature inversion still decreases. The increased stability of the ice-covered branch with decreasing inversion strength is in agreement with the decrease in surface warming efficiency for weaker temperature inversions seen in Bintanja, Graversen and

Hazeleger (2011), however the reason for the plateau (and slight decrease in stability seen for very large mixing) is unclear and suggests other mechanisms may be affected by these perturbations to surface mixing.

I also present stable states for the SCM when run with a mixed phase saturation-adjustment cloud scheme. I consider two representations of cloud area fraction: fixing cloud area fraction to values from contemporary ERA5 reanalysis and a diagnostic parameterisation outlined in the previous chapter. Both configurations show a similar bifurcation structure to the clear sky configuration with perennially ice-covered and ice-free states bounded by bifurcation points. Interestingly, the ERA5 configuration shows evidence of a branch of stable seasonally-free states that *decrease* in surface energy density as atmospheric CO_2 increases. This behaviour is characteristic of unstable states of system's with saddle-node bifurcations. The mechanism for the stability of these states is unclear.

In both configurations for the perennially ice-covered branch there is a slight negative feedback in the surface cloud radiative effect as atmospheric CO_2 increases. This decreases the sensitivity of ice thickness to changes in CO_2 and increases the stability of the state (though this is balanced out by a year-round positive cloud radiative effect when ice-covered). When cloud area fraction is parameterised, the ice-free branch shows a similar negative feedback in cloud radiative effect between CO_2 concentrations of 100 and $1000\,ppm$ driven by gradual disappearance of high clouds with increasing CO_2. These high clouds stabilise the ice-free state to lower CO_2 concentrations and increase the bistability of the system. When the parameterisation is used but high clouds are artificially removed at each timestep no feedback is seen and there is a thinner bistable window.

Finally, I give a simple demonstration of the sensitivity of the column model to changes to the composition and vertical structure of atmospheric heat transport. When CO_2 is held constant and the SCM is forced with constant perturbations to atmospheric heat transport the width of the bistable region is reduced for more bottom-heavy and moist heat transport perturbations. This demonstrates the sensitivity of Arctic sea ice to these features that are often not resolved in simple models.

The results shown in this chapter illustrate the importance of vertical structure, clouds and heat transport on the bifurcation structure of sea ice. However, simplifications in the model lead to simulations of unrealistically wide bistable regions. This is likely driven by a lack of atmospheric heat transport feedbacks. In the next chapter I explore the effect simple heat transport feedbacks have on the system.

Chapter 5 Atmospheric heat transport

1 Introduction

In Chapter 4 I explored the stability of sea ice in an Arctic single column model for different atmospheric CO_2 concentrations when prescribed with contemporary seasonal cycles of atmospheric heat transport (Cardinale *et al.*, 2021). A robust feature of these configurations is extremely wide bistable regions – often extending to carbon dioxide concentrations less than contemporary concentrations (Figure 21). This is largely driven by the stabilisation of warm ice-free states for low CO_2. In particular, the ice-free state is stabilised by large atmospheric heat transport which is held at the same seasonal cycle as for the contemporary ice-covered state.

Winton (2008b) and Wagner and Eisenman (2015b) both identify changes in atmospheric heat transport as having a smoothing effect on bistability in Arctic sea ice. Wagner and Eisenman (2015b) demonstrate that including a representation of diffusive heat transport in a latitude-resolving model with thermodynamic sea ice can eliminate bistability. When diffusivity is set to 0 the system is bistable, but quickly becomes monostable as it increases, including for diffusivities that agree with the contemporary climate. In their original paper, Eisenman and Wettlaufer (2009) include a simple temperature dependent representation of heat transport, proportional to the temperature difference between the model surface temperature and the weighted average temperature seasonal cycle of the region $0\,°N - 70\,°N$,

and find a bistable system with a stable ice-covered state with a smooth loss of summer sea ice and a stable perennially ice-free state.

Both Eisenman and Wettlaufer (2009) and Wagner and Eisenman (2015b) model represent atmospheric heat transport with temperature tendencies proportional to the meridional temperature gradient and don't explicitly model the Arctic atmosphere. Their simplicity means these models can't resolve more nuanced features of atmospheric heat transport such as its vertical structure, the different effects of dry and moist transport, and changes in heat transport not driven by the meridional temperature gradient. However, they clearly mark atmospheric heat transport as a highly important feature for the bifurcation structure of Arctic sea ice.

Various studies demonstrate that while the *dry* component of atmospheric heat transport into the Arctic is roughly proportional to the meridional temperature gradient, the *moist* component is driven by warming of the lower latitudes (e.g. Yoshimori *et al.*, 2014). Held and Soden (2006) demonstrate that the increase in atmospheric heat transport is roughly in line with thermodynamic effects captured in the Clausius-Clapeyron equation. In a simple GCM with a slab ocean and no representation of clouds or sea ice Henry and Vallis (2021) find very little change in the overall atmospheric heat transport into the Arctic when atmospheric CO_2 is increased by factors of 4 and 16. Here the reduction in dry heat transport is almost exactly balanced by an increase in moist heat transport.

My aim in this chapter is to explore the effect that heat transport feedbacks have on the bifurcation structure of the single column models as explored in the previous two chapters.

As previous work indicates that changes in heat transport are largely driven by changes in the meridional temperature gradient and warming of lower latitudes it is

very difficult to represent this accurately in a single column model. To do this it is necessary to make assumptions about the evolution of lower latitudes. To maintain the simplicity of my model I use a crude parameterisation based on an extension of the heat transport feedback used in Eisenman and Wettlaufer (2009) that accounts for the warming of lower latitudes, changes in moist heat transport, and the vertical profile of atmospheric heat transport.

In the next section I give an overview of how I represent these feedbacks in the SCM. In the following section I present results using these parameterisations, showing: the bifurcation structure of the model with heat transport feedbacks and the effect of varying the strength of meridional heat transport and lower latitude warming on bistability. Finally, I present my conclusions.

2 Methods

2.1 Dry heat transport feedback

Following Eisenman and Wettlaufer (2009) I parameterise the dry component of atmospheric heat transport into the Arctic, F_{dry}, as proportional to the meridional temperature gradient, ΔT:

$$F_{dry} = k\Delta T \tag{58}$$

where k is a constant of proportionality.

I calculate ΔT as the difference between the lowest level air temperature of the SCM, T_0, and the area-weighted average seasonal cycle of the 2-metre air temperature of the region $0\,°N - 70\,°N$ over the period 1980-2016 (the same period as the Cardinale *et al.* (2021) data used to force models in the previous chapter) in ERA5 reanalysis, termed T_{south}.

$$\Delta T = T_0(t) - T_{south} \tag{59}$$

To account for warming in lower latitudes I assume T_{south} increases with atmospheric CO_2 in line with a climate sensitivity, CS, for a doubling of the CO_2 concentration, $[CO_2]$:

$$T_{south}([CO_2], t) = T_{south,0} + CS\, log_2\left(\frac{[CO_2]}{[CO_2]_0}\right) \tag{60}$$

where $T_{south,0}$ is the T_{south} seasonal cycle as calculated from reanalysis and $[CO_2]_0$ is the reference CO_2 concentration, taken here to be $330\ ppm$.

I tuned k to the contemporary climate by calculating the steady state seasonal cycles of the system for a range of values and comparing the atmospheric heat transport values to data from reanalysis (Cardinale *et al.*, 2021) (Figure 29). Of the values tested, $k = 2.8\, Wm^{-2}K^{-1}$, gave the best agreement and is used throughout this chapter unless stated otherwise.

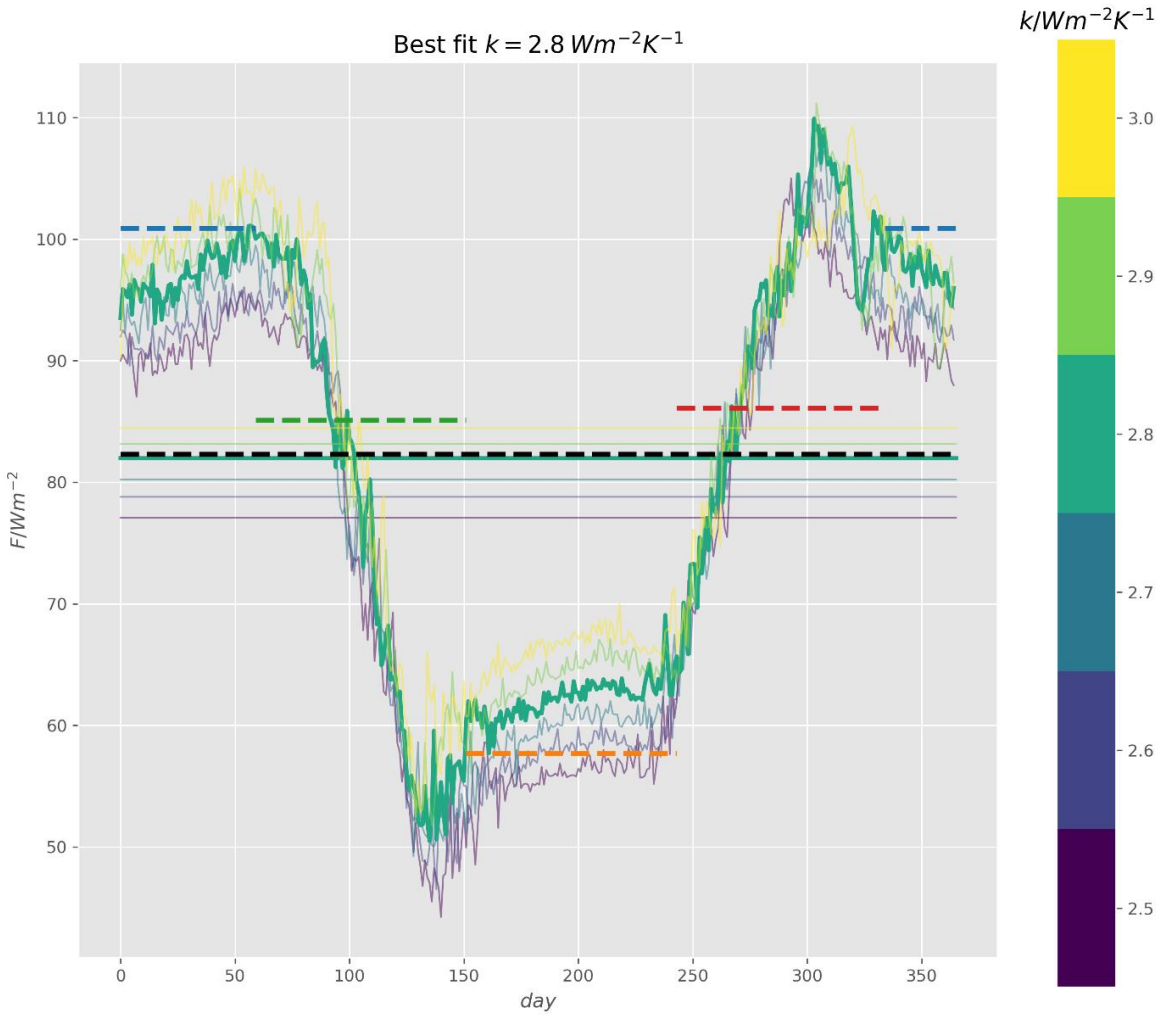


Figure 29 Comparison of the steady state seasonal cycle of atmospheric heat transport for the single column model in contemporary conditions for a range of k values (solid lines) to data from reanalysis (Cardinale et al.*, 2021) (dashed lines). Solid horizontal lines represent the annual mean of the SCM seasonal cycles, with the thicker line representing the $k = 2.8\ Wm^{-2}K^{-1}$ best fit, and the black dashed line represents the annual mean of reanalysis data. The dashed coloured lines represent the seasonal averages of the reanalysis data. $k = 2.8\ Wm^{-2}K^{-1}$ gives the best agreement with reanalysis.*

Unless stated otherwise I use a value of $CS = 3\ K$ throughout this chapter taken from the middle of the range found in CMIP6 models. Note that as I am only considering the climate sensitivity of 'extra-Arctic' regions from $0 - 70\ °N$ which warm at a much slower rate than the poles, the value of CS should be slightly lower than the equilibrium climate sensitivities calculated for global average temperatures. The sensitivity of the system to changes in CS is explored in section 3.3.

2.2 Moist heat transport feedback

Following Held and Soden (2006) and Yoshimori *et al.* (2014) I assume that transport of latent heat into the Arctic increases in line with the Clausius-Clapeyron as lower latitudes warm. I use the same assumption for the warming of lower latitudes as for the dry heat transport feedback (60) and use the latent heat transport from Cardinale *et al.* (2021) as the base value for changes in heat transport, $F_{moist,0}$.

$$F_{moist} = F_{moist,0}\, exp\left(\frac{L}{R_v}\frac{CS\, log_2\left(\frac{[CO_2]}{[CO_2]_0}\right)}{T_{south,0} + CS\, log_2\left(\frac{[CO_2]}{[CO_2]_0}\right)}\right) \quad (61)$$

For this parameterisation, moist heat transport is purely controlled by the warming of lower latitudes and therefore by the atmospheric CO_2 concentration. F_{moist} increases with T_{south} in line with the Clausius-Clapeyron relation, assuming T_{south} increases with $[CO_2]$ in line with a climate sensitivity CS. Unlike the dry heat transport feedback parameterisation, this means that for the *same* $[CO_2]$ different model states have the same moist heat transport.

3 Results

3.1 Introducing heat transport feedbacks

Figure 30 shows the stable states of the SCM when atmospheric heat transport is represented with the feedbacks outlined above using $k = 2.8\, Wm^{-2}K^{-1}$ and $CS = 3.0\, K$ in a clear sky configuration. The stability of the system is markedly different to the case without heat transport feedbacks (Figure 21). Notably here there is a smooth loss of summer sea ice as in Eisenman and Wettlaufer (2009), stabilised by the reduction in summer heat transport for seasonally ice-free states. The bistable region is also much smaller, this is driven by the perennially ice-free (red) bifurcation point occurring at a much higher CO_2 concentration than when heat transport

feedbacks are not included due to the sharp reduction in heat transport for ice-free states. Here the bistable region corresponds to a fractional CO_2 increase of 0.22. While ice-cover thins at a greater rate when heat transport feedbacks are included, the ice-covered branch (blue/grey) ceases to be stable at similar CO_2 concentrations in both configurations. Finally, near the bifurcation point of the upper branch there is a thin region of seasonally ice-free (grey) states separated by an abrupt transition from the perennially ice-free states. It is currently unclear whether these belong to a thin, third branch of stable states or if they occupy the same branch as the perennially ice-free states and are separated by a monostable abrupt transition. It's interesting to note that the transient response of a system with a monostable abrupt transition with slow relaxation times (e.g. Li *et al.*, 2013) may be hard to distinguish from a system with a thin bistable window like Figure 30 as both cases exhibit similar hysteretic/quasi-hysteretic behaviour.

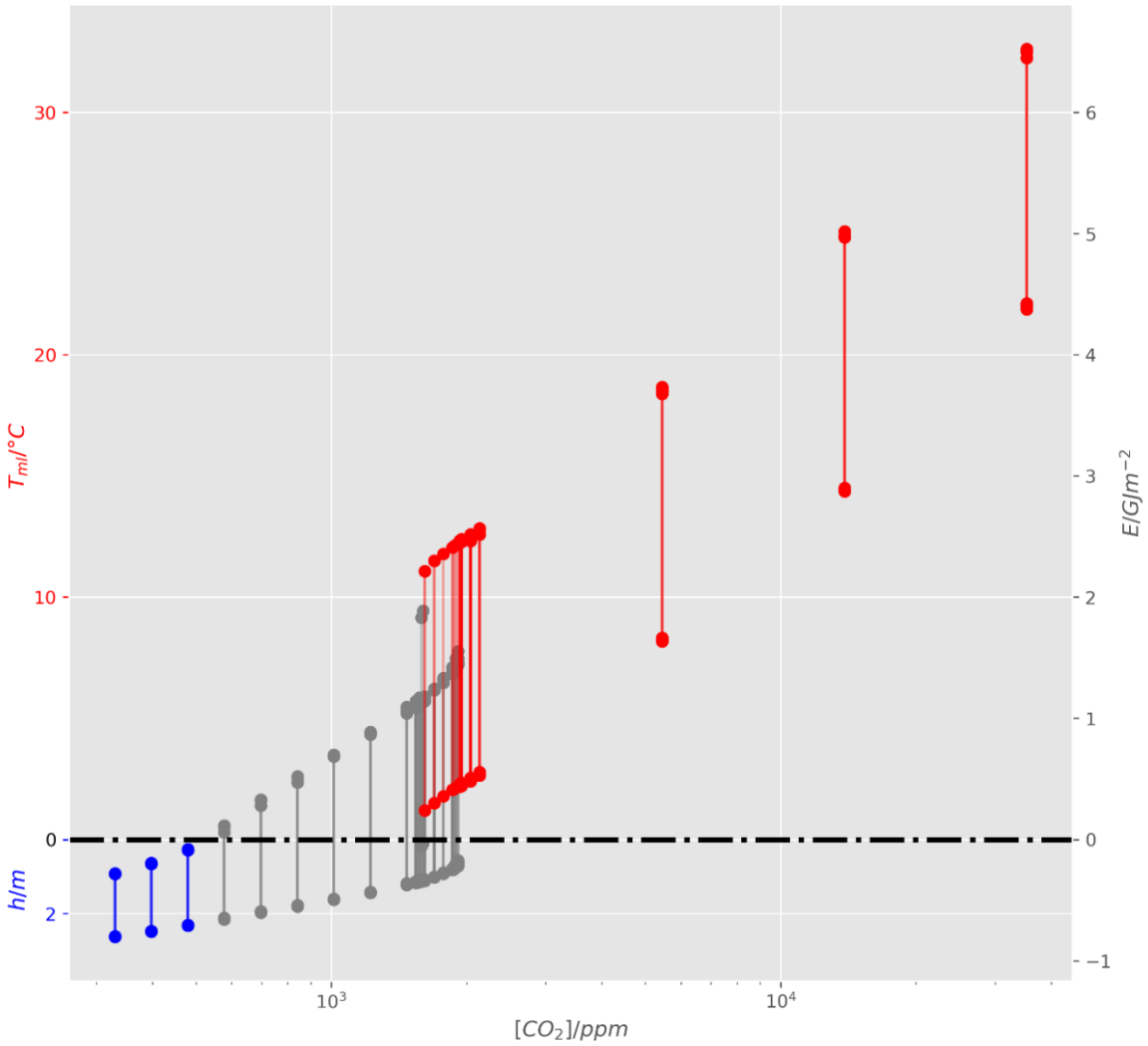


Figure 30 As in Figure 21 using feedbacks for dry and moist heat transport (using $k = 2.8\ Wm^{-2}K^{-1}$ and $CS = 3.0\ K$) and without the cloud scheme.

Figure 31 presents the same data as Figure 30 when the SCM is run using the cloud scheme with parameterised cloud area fraction, here the bistable region corresponds to a fractional CO_2 increase of 0.23. The qualitative behaviour of the system is very similar to the clear sky configuration with smooth loss of summer sea ice and a bifurcation associated with the abrupt loss of winter sea ice. With clouds included, both bifurcation points get shifted to lower $[CO_2]$. For the ice-covered (blue/grey) branch this is driven by clouds accelerating the melt of sea ice, particularly winter ice, hastening the onset of total ice loss. For the ice-free (red) branch, clouds don't significantly alter the energy of the branch for a given $[CO_2]$,

instead the shift in the bifurcation point is driven by stabilisation of cooler perennially ice-free states at lower $[CO_2]$ values.

Notably, the inclusion of heat transport feedbacks seemingly eliminates the stabilising effects of low and high clouds on ice-covered and ice-free states respectively seen in the previous chapter when heat transport was held at a constant seasonal cycle.

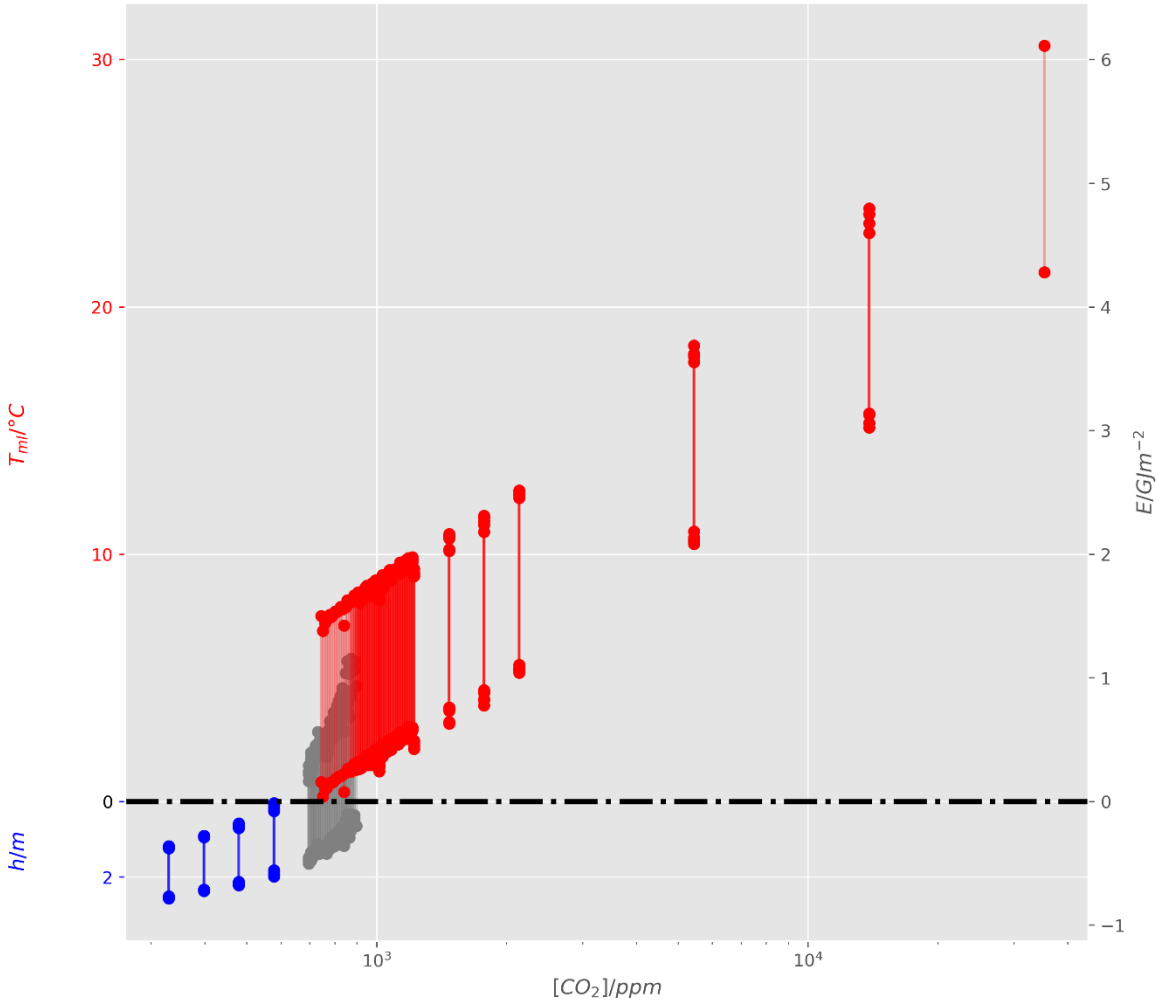


Figure 31 As in Figure 30 for the SCM including the cloud scheme using parameterised cloud area fraction.

3.2 Sensitivity to dry heat transport feedback strength

The results in Figure 30 and Figure 31 differ from those in Wagner and Eisenman (2015b) who find that in an energy balance model with resolved diffusive heat transport and seasonality, bistability is eliminated. They also find that bistability is

recovered for low diffusivities and decreases as the system's diffusivity increases. The key differences between the heat feedbacks in my model and in Wagner and Eisenman (2015b) are that my model represents latent heat transport and its predicted increase as lower latitudes warm, and that where Wagner and Eisenman (2015b) explicitly resolves a diffusive heat transport I approximate it as outlined in equation (58).

To see if this model shows similar sensitivity to the diffusivity of dry heat transport I ran the model with a range of values for the dry heat transport coefficient, k, and measured the width of their bistable regions. For comparison with their results which exclude the moist heat transport feedback I repeated this with moist heat transport fixed to the seasonal cycle at $330\ ppm$.

Figure 32 plots the relationship between the dry heat transport coefficient, k, and the width of the bistable region, B, for the SCM with resolved sensible and latent heat feedbacks (blue) and sensible heat feedback only (red). Here I calculate B as the fractional increase of $[CO_2]$ across the bistable region. Note that $B = 0$ represents the point at which the system ceases to be bistable.

When only the dry heat transport feedback is included (red line) the system becomes less bistable as k increases, but remains weakly bistable as far as $k = 5\ Wm^{-2}K^{-1}$. Moreover, the sensitivity of the system to increasing k decreases for larger k values, similar to behaviour seen in Wagner and Eisenman (2015b).

The decrease in bistability is caused by the difference in heat transport at the two bifurcation points. As the bifurcation point of the ice-covered state corresponds to a lower surface temperature, it therefore experiences a greater dry heat transport than the bifurcation point of the ice-free state. As the strength of the feedback increases with k this means the difference in heat transport between the two points increases

– causing the ice-covered bifurcation point to shift further to the left than the ice-free bifurcation point, therefore reducing bistability in the system. As the system approaches a monostable state, this differential effect tends to zero.

Including the moist heat transport feedback (blue line) decreases the bistability of the system in a similar way. The increase in moist heat transport for larger $[CO_2]$ values shifts the bifurcation point of the ice-covered state more than for the (lower $[CO_2]$) ice-free state bifurcation point. As the bistable window decreases in width the relative difference in latent heat transport at the two bifurcation points decreases and the effect tends to zero.

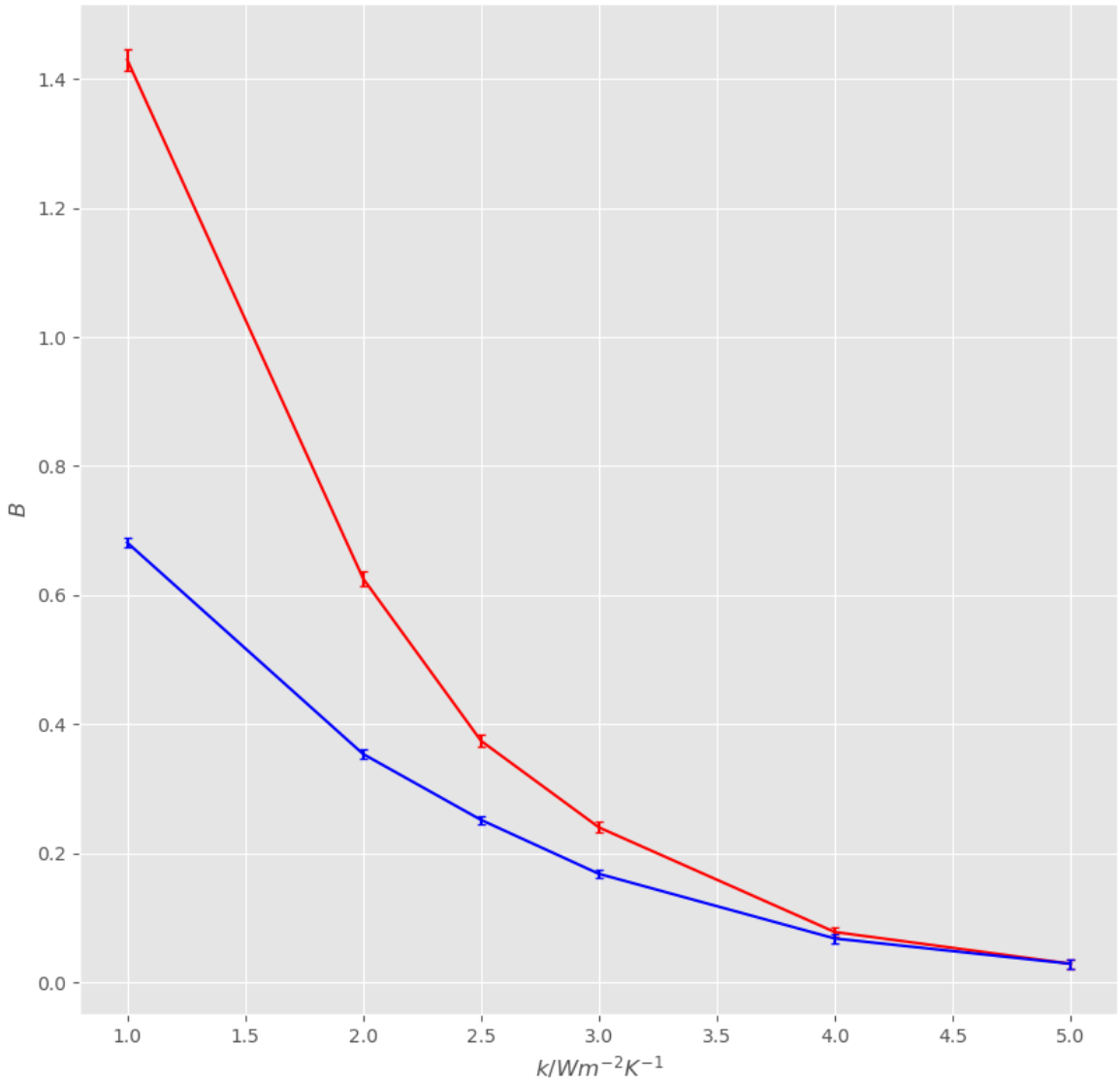


Figure 32 Width of the bistable region, B, plotted against the diffusive heat transport coefficient, k, for the SCM in a clear sky configuration with resolved dry and moist heat transport feedbacks (blue) and resolved sensible feedback only (red). CS was set at $3\ K$ for all simulations. The error bars mark the uncertainty on each B measurement. B is calculated as the fractional increase of $[CO_2]$ across the bistable region. $B = 0$ therefore, marks the point where the system ceases to be bistable.

3.3 Sensitivity to climate sensitivity

Throughout this chapter I have represented the effect of the warming of lower latitudes on heat transport feedbacks using an 'extra-Arctic' climate sensitivity parameter, $CS = 3\ K$. However, there is considerable spread in the climate sensitivity of models in CMIP6 and the relative rate at which lower latitudes warm has an effect on the heat transport into the Arctic. To explore this, I conducted a

similar analysis as in the previous section for variable CS and with k fixed at $2.8\ Wm^{-2}K^{-1}$ for resolved dry and moist heat transport feedbacks.

Figure 33 shows the relationship between increasing CS and the width of the bistable region, B, (defined as above). For larger CS the width of the bistable region decreases, however the system's sensitivity is weaker for larger CS. The system remains bistable for CS up to $6\ K$ (data for $CS = 6\ K$ is not included in Figure 33 due to the low $[CO_2]$ resolution of those experiments).

As with k, the shrinking of the bistable region for increasing climate sensitivity can be explained by considering the change in atmospheric heat transport as $[CO_2]$ increases. From Clausius-Clapeyron (see equation (61)) it can be easily calculated that moist heat transport reaches greater values for greater warming in lower latitudes – therefore larger CS induces a greater difference in heat transport between two $[CO_2]$ values, decreasing bistability by the same mechanism as discussed above. Similarly, for dry heat transport, the difference in dry heat transport between two $[CO_2]$ values is to first order proportional to CS, so a larger CS decreases the width of the bistable region.

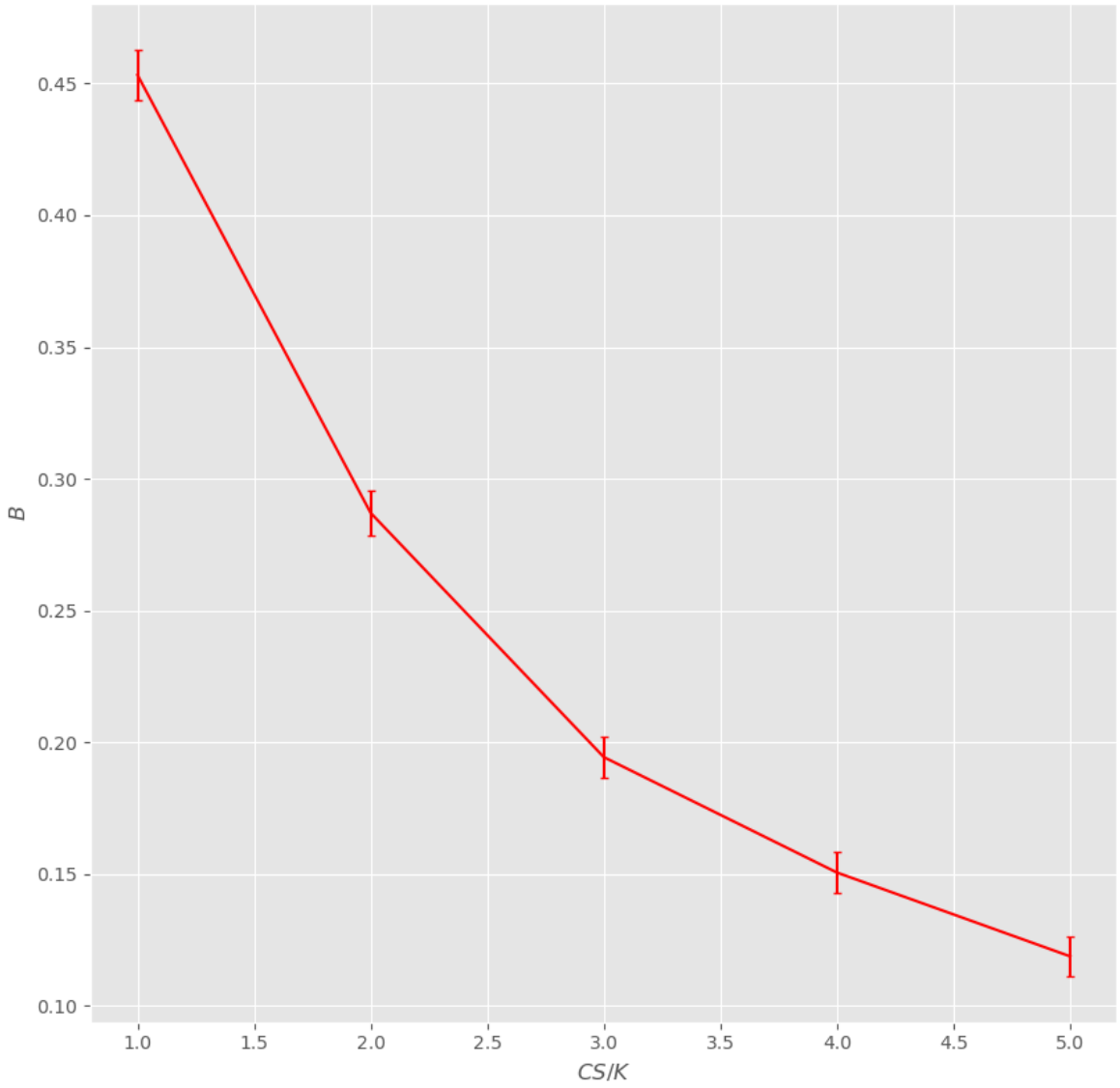


Figure 33 As for Figure 32 for the SCM in a clear sky configuration with resolved dry and moist heat transport feedbacks for varying CS (plotted on x axis) with k set at $2.8\ Wm^{-2}K^{-1}$ for all simulations.

4 Conclusions

In this chapter I explore how the introduction of simple atmospheric heat transport feedbacks affect the stability structure of sea ice in the single column model (SCM) of the Arctic introduced in Chapter 3.

When the SCM is forced laterally by a state-independent seasonal cycle of atmospheric heat transport it exhibits a broad range of atmospheric CO_2 concentrations where perennially ice-covered and perennially ice-free states are

bistable – extending to CO_2 concentrations well below contemporary conditions. Moreover, seasonally ice-free conditions are only stable for a small range of CO_2 concentrations and are ‘sandwiched’ in between the perennially ice-covered and ice-free states in a third stable state. This stability structure is similar to that seen in Thorndike (1992a), but strongly differs from most other modelling studies. A significant contributor to this is the lack of feedbacks in atmospheric heat transport – allowing perennially ice-free states to remain stable at very low CO_2 concentrations and destabilising seasonally ice-free states.

I introduced feedbacks for dry and moist atmospheric heat transport to the model. I parameterised dry heat transport as proportional to the temperature gradient between the SCM and ERA5 reanalysis data modified by a climate sensitivity parameter for departures from contemporary CO_2 concentrations; and moist heat transport by altering contemporary heat transport in line with the Clausius-Clapeyron relation for departures from contemporary CO_2 concentrations.

Including these feedbacks significantly altered the stability structure of the system: introducing a smooth loss of summer sea ice and significantly reducing the size of the bistable region of the system. A structure similar to that seen in Eisenman and Wettlaufer (2009).

Testing for a range of dry heat transport feedbacks shows a weakening of bistability for stronger heat transport feedbacks, tending towards a monostable system – though all configurations tested exhibited at least a thin bistable region.

Similarly, increasing the rate of warming of lower latitudes weakened bistability in the system. However, the range of configurations tested, spanning expected climate sensitivities from CMIP6 models, each exhibited a bistable region.

These results mark changes in atmospheric heat transport as a significant factor in determining the stability structure of Arctic sea ice. However, they differ with Wagner and Eisenman (2015b) who find diffusive heat transport eliminates bistability completely in a latitude resolving model without a resolved atmosphere or latent heat transport feedback. An interesting next step would be to couple a 1-dimensional array of these SCMs into a latitude resolving model with diffusive dry heat transport and a resolved latent heat transport feedback to see if bistability is eliminated – completely bridging the gap between the more detailed representation of Arctic climate in the SCM and the heat transport in latitude-resolving models. A further, more complicated, step would be to increase complexity further by integrating the components of the SCM into the dynamical core of an atmospheric GCM to explicitly resolve changes in atmospheric heat transport as the model changes state. This would keep these parameterisations constant while introducing new physics into the system.

Chapter 6 Conclusions

1 Introduction

In this chapter I briefly summarise the work in my thesis and present some conclusions. I then go onto suggest further work motivated by my findings.

2 Conclusions

Initially, I investigate the effect of spatial variation and mechanical processes on bistability using the ice thickness distribution. Firstly, I consider using a Fokker-Planck parameterisation of mechanical processes (Toppaladoddi and Wettlaufer, 2015, 2017) and demonstrate that a systematic error in the scheme undermines conservation of ice volume, particularly for large open water fractions, making it unsuitable for modelling the disappearance of sea ice. This scheme could be modified to ensure conservation of ice volume by including functional dependence on ice thickness, h, and thickness distribution, $g(h)$, in the parameters k_1 and k_2. However, constraining the form of these functions to fit to observations would be a difficult task. I then consider a coagulation parameterisation of mechanical processes (Godlovitch, Illner and Monahan, 2011) that ensures conservation of ice thickness and demonstrate that using this parameterisation as the rate of mechanical processes increases the width of the model's bistable region decreases until it eventually vanishes. This process is likely driven by mechanics increasing the model's open water fraction, thereby increasing the total energy input into sea ice melt. This analysis is limited by poorly constrained parameters for the coagulation parameterisation and likely overestimation of the contribution of the energy flux into open water to basal sea ice melt. These results are notable for

finding that bistability in a simple model can be eliminated entirely by introducing ice mechanics – bringing the results in line with the majority of GCM simulations. This is an interesting result and could be probed further by tuning the coagulation mechanics parameterisation to observations and testing its sensitivity to other kernel choices. Moreover, this chapter illustrates the effectiveness of two different mechanics parameterisations for the ice thickness distribution for modelling the disappearance of ice cover. I find that the coagulation mechanics parameterisation is better suited for this use case than the Fokker-Planck parameterisation.

I then explore the effect of ice-atmosphere interactions on sea ice's bifurcation structure using a single column model of the Arctic atmosphere coupled to a slab thermodynamic model of sea ice forced with changes to atmospheric CO_2. Initially I do this using a fixed seasonal cycle of atmospheric heat flux for all states. For both clear sky and cloudy configurations, I find distinct stable perennially ice-covered and ice-free states that cease to be stable at bifurcation points with an exceedingly large bistable region. The bistable region extends to atmospheric CO_2 concentrations well below contemporary levels, this is largely driven by the lack of atmospheric heat transport feedbacks stabilising the perennially ice-free states at these concentrations.

To test for the effect of vertical temperature structure I follow Bintanja, Graversen and Hazeleger (2011) and conduct experiments with modified surface mixing strengths which modify the inversion strength near the surface. I find that as surface mixing reduces the inversion strength, the ice-covered state is stabilised at higher CO_2 concentrations. This is likely due to the reduced surface heating efficiency of a weaker inversion. However, the increased stabilisation plateaus before the annual mean inversion disappears completely and even appears to reverse trend for low inversion strengths. The mechanism for this non-monotonic relationship is unclear

and warrants further work to investigate it. These results clearly indicate the importance of vertical temperature structure and the portioning of energy between the atmosphere and model surface for the system's stability – something not resolved in simple models without an atmospheric component.

When a cloud scheme is introduced to the model it maintains the same overall bifurcation structure, however some interesting differences emerge. When ice-covered, the surface radiative effect of clouds is net positive and leads to an increase in downwelling radiative flux. However, for increasing CO_2 there is a negative feedback on this cloud radiative effect driven by low clouds which reduces the rate at which ice melts for increasing CO_2. These two factors act to lower and raise the CO_2 concentration of the bifurcation point – their net effect varies depending on the details of the cloud parameterisation. A similar stabilising effect on the perennially ice-free state due to high clouds can be seen when changes in cloud area fraction are parameterised. At low CO_2 concentrations a layer of elevated clouds produces a strong warming effect on the surface, increasing the stability of low CO_2 ice-free states. For higher CO_2 values these clouds disappear and the annual average surface cloud radiative effect becomes negative. For the configurations tested, when high and low clouds are allowed to evolve they extended the region of bistability. Overall, I found that while resolving clouds in the model changed the position of the bifurcation points and whether or not the system resolved a seasonally ice-free band, they did not significantly alter the bifurcation structure of the system which still showed perennially ice-free and perennially ice-covered bands bounded by bifurcation points, with a large region of overlap. Similarly, changes to the inversion structure of the system by changing surface mixing slightly changed the position of the perennially ice-covered band's bifurcation

point but didn't significantly change the transition away from the perennially ice-free state.

I then conducted some additional tests for the model's bifurcation structure when forced with perturbations to atmospheric heat transport with CO_2 held constant. For more bottom-heavy heat transport the region of bistability is narrower – this is due to the increased efficiency of bottom-heavy heat transport of warming the surface. Likewise, when forced with moist heat transport the system has a significantly thinner bistable window than with dry, due to its additional impact on water vapour and clouds as longwave emitters. Again, this demonstrates the importance of accurately resolving the structure and composition of atmospheric heat transport to accurately simulate the bifurcation structure of sea ice – something that cannot be done in models without resolved atmospheres. Single column models of the kind used here are also vast simplifications as they must be forced by prescribed heat transport. An atmospheric GCM coupled to a surface component would allow for reactive heat transport into the Arctic with a resolved structure.

Finally, I conducted some experiments using simple parameterisations of feedbacks for dry and moist heat transport into the Arctic. When included, these drastically altered the system's bifurcation structure – more than any other change considered – introducing a smooth transition between a perennially ice-covered and seasonally ice-free state, while maintaining a bifurcation separating these from a perennially ice-free state. When the strength of meridional transport of dry heat was increased, the bistable region shrank – tending towards zero. Similarly, when the parameterised rate of warming of lower latitudes was increased the bistable region shrank – but in my experiments the system remained bistable for warming in line with a climate sensitivity of $6\,K$. These decreases in bistability are driven by the difference in heat transport between the cooler, higher CO_2 ice-covered bifurcation

point and the hotter, lower CO_2 ice-free bifurcation point. The drastic differences between these configurations and configurations without resolved heat transport feedbacks mark changes in atmospheric heat transport as a crucial feature in the accurate resolution of the bifurcation structure of Arctic sea ice. Compared to the other modifications I make in this thesis, resolving atmospheric heat transport has by far the most significant impact on the system's bifurcation structure. This indicates that this has a much larger influence on the bifurcation structure than the other climate features I investigate. Similar results are seen in GCM experiments (Winton, 2008) indicating the robustness of this feature beyond simple models. My model uses a highly simplified parameterisation of heat transport – it would be interesting for future work to investigate how more realistic parameterisations affect bifurcation structure.

3 Further work

A potential extension of the ice thickness distribution work would be to tune the coagulation parameterisation by fitting the steady state distribution to observed Arctic ice thickness distributions. This could be repeated for a variety of coagulation kernels, beyond the constant kernel used in this thesis. A potential method for doing this would be to compare the decay rate of the thick-ice tail of the modelled thickness distribution (a robust feature of the ice thickness distribution) to the observed decay rate. I also assume an unchanging coagulation kernel as the Arctic changes state, another interesting line of work would be to investigate potential state-dependency in the kernel. Both lines of work would allow for a more accurate picture of how mechanical processes will impact the bifurcation structure of Arctic sea ice.

The role of atmospheric heat transport feedbacks is highlighted as deeply important for the system's bifurcation structure. A priority for further work would be to better

constrain its effect by increasing the complexity of these feedbacks. This could be done by for example by coupling a 1-dimensional array of the single column models together to make a latitude-resolving model and parameterising diffusive heat transport with a fixed vertical profile. Further complexity could be added by integrating the ice and cloud physics of the SCM into the dynamical core of an atmospheric GCM to allow for more comprehensive simulation of atmospheric circulation. Initially this could be done using a simple aquaplanet configuration before adding simple continental geometries.

It would also be very interesting to conduct similar analysis of atmospheric processes to that done in chapter 4 for model setups with improved atmospheric heat transport feedbacks – including the parameterisations used in chapter 5. Further extensions to the atmospheric feedback analysis include a more detailed analysis of the effect of enhanced mixing on the perennially ice-covered state up to the elimination of the temperature inversion, and into the mechanism for the observed 'plateau' in its stability. Moreover, further work could be done to isolate the effect of changes to the temperature inversion strength on model stability when clouds are included.

Another interesting avenue of further work would be to explore the effect of stochasticity on the system. Throughout this thesis I assume completely deterministic, regular forcing cycles. The only non-deterministic element is in the McICA cloud area fraction representation which contains a random element. Future work could examine the effect of introducing stochasticity to the system on its stable states and transient behaviour. This could be done for any level of complexity – from the simple EW09 slab ice model similar to the approach in Moon and Wettlaufer (2017), through the ice thickness distribution model, to the single column model, and

onto more complex configurations. Another possible extension could be consideration of the mechanisms explored in this thesis to Antarctic sea ice cover.

Bibliography

Abbot, D.S., Silber, M. and Pierrehumbert, R.T. (2011) 'Bifurcations leading to summer Arctic sea ice loss', *Journal of Geophysical Research Atmospheres*, 116(19), pp. 1–11. Available at: https://doi.org/10.1029/2011JD015653.

Abbot, D.S. and Tziperman, E. (2008) 'Sea ice, high-latitude convection, and equable climates', *Geophysical Research Letters*, 35(3), pp. L03702–L03702. Available at: https://doi.org/10.1029/2007GL032286.

Abbot, D.S. and Tziperman, E. (2009) 'Controls on the Activation and Strength of a High-Latitude Convective Cloud Feedback', *Journal of the Atmospheric Sciences*, 66(2), pp. 519–529. Available at: https://doi.org/10.1175/2008JAS2840.1.

Andreas, E.L. *et al.* (2010) 'Parameterizing Turbulent Exchange over Sea Ice in Winter', *Journal of Hydrometeorology*, 11(1), pp. 87–104. Available at: https://doi.org/10.1175/2009JHM1102.1.

Armour, K.C. *et al.* (2011) 'The reversibility of sea ice loss in a state-of-the-art climate model', *Geophysical Research Letters*, 38(16). Available at: https://doi.org/10.1029/2011GL048739.

Ashwin, P. *et al.* (2012) 'Tipping points in open systems: bifurcation, noise-induced and rate-dependent examples in the climate system', *Philosophical Transactions of the Royal Society A: Mathematical, Physical and Engineering Sciences*, 370(1962), pp. 1166–1184. Available at: https://doi.org/10.1098/rsta.2011.0306.

Aylmer, J., Ferreira, D. and Feltham, D. (2020) 'Impacts of Oceanic and Atmospheric Heat Transports on Sea Ice Extent', *Journal of Climate*, 33(16), pp. 7197–7215. Available at: https://doi.org/10.1175/JCLI-D-19-0761.1.

Bathiany, S. *et al.* (2016) 'Beyond bifurcation: using complex models to understand and predict abrupt climate change', *Dynamics and Statistics of the Climate System*, pp. dzw004–dzw004. Available at: https://doi.org/10.1093/climsys/dzw004.

Bintanja, R., Graversen, R.G. and Hazeleger, W. (2011) 'Arctic winter warming amplified by the thermal inversion and consequent low infrared cooling to space', *Nature Geoscience*, 4(11), pp. 758–761. Available at: https://doi.org/10.1038/ngeo1285.

Brovkin, V. *et al.* (2021) 'Past abrupt changes, tipping points and cascading impacts in the Earth system', *Nature Geoscience*, 14(8), pp. 550–558. Available at: https://doi.org/10.1038/s41561-021-00790-5.

Budyko, M.I. (1969) 'The effect of solar radiation variations on the climate of the Earth', *Tellus*, 21(5), pp. 611–619. Available at: https://doi.org/10.1111/j.2153-3490.1969.tb00466.x.

Cardinale, C.J. *et al.* (2021) 'Stratospheric and Tropospheric Flux Contributions to the Polar Cap Energy Budgets in: Journal of Climate - Ahead of print', *Journal of Climate*. Available at: https://journals.ametsoc.org/view/journals/clim/aop/JCLI-D-20-0722.1/JCLI-D-20-0722.1.xml?tab_body=pdf.

Clough, S.A. *et al.* (2005) ‘Atmospheric radiative transfer modeling: a summary of the AER codes’, *Journal of Quantitative Spectroscopy and Radiative Transfer*, 91(2), pp. 233–244. Available at: https://doi.org/10.1016/j.jqsrt.2004.05.058.

Cronin, T.W. and Jansen, M.F. (2016) ‘Analytic radiative-advective equilibrium as a model for high-latitude climate’, *Geophysical Research Letters*, 43(1), pp. 449–457. Available at: https://doi.org/10.1002/2015GL067172.

Curry, J.A. *et al.* (1996) ‘Overview of Arctic Cloud and Radiation Characteristics’, *http://dx.doi.org/10.1175/1520-0442(1996)009<1731:OOACAR>2.0.CO;2* [Preprint]. Available at: https://doi.org/10.1175/1520-0442(1996)009<1731:OOACAR>2.0.CO;2.

Devasthale, A. *et al.* (2010) ‘Quantifying the clear-sky temperature inversion frequency and strength over the Arctic Ocean during summer and winter seasons from AIRS profiles’, *Atmospheric Chemistry and Physics*, 10(12), pp. 5565–5572. Available at: https://doi.org/10.5194/acp-10-5565-2010.

Dong, X. *et al.* (2010) ‘A 10 year climatology of Arctic cloud fraction and radiative forcing at Barrow, Alaska’, *Journal of Geophysical Research: Atmospheres*, 115(D17). Available at: https://doi.org/10.1029/2009JD013489.

ECMWF, H. (2023) ‘IFS Documentation CY48R1 - Part IV: Physical Processes’, in *IFS Documentation CY48R1*. ECMWF (IFS Documentation, 4). Available at: https://www.ecmwf.int/en/publications/ifs-documentation (Accessed: 13 July 2023).

Eicken, H. and Lange, M.A. (1989) ‘Sea ice thickness data: The many vs. the few’, *Geophysical Research Letters*, 16(6), pp. 495–498. Available at: https://doi.org/10.1029/GL016i006p00495.

Eisenman, I. (2012) ‘Factors controlling the bifurcation structure of sea ice retreat’, *Journal of Geophysical Research: Atmospheres*, 117(D1). Available at: https://doi.org/10.1029/2011JD016164.

Eisenman, I. and Wettlaufer, J.S. (2009) ‘Nonlinear threshold behavior during the loss of Arctic sea ice’, *Proceedings of the National Academy of Sciences of the United States of America*, 106(1), pp. 28–32. Available at: https://doi.org/10.1073/pnas.0806887106.

Emanuel, K.A. and Živković-Rothman, M. (1999) ‘Development and Evaluation of a Convection Scheme for Use in Climate Models’, *Journal of the Atmospheric Sciences*, 56(11), pp. 1766–1782. Available at: https://doi.org/10.1175/1520-0469(1999)056<1766:DAEOAC>2.0.CO;2.

Ferreira, D., Marshall, J. and Rose, B. (2011) ‘Climate Determinism Revisited: Multiple Equilibria in a Complex Climate Model’, *Journal of Climate*, 24(4), pp. 992–1012. Available at: https://doi.org/10.1175/2010JCLI3580.1.

Forbes, R. (2021) ‘Ice and Mixed-Phase Microphysics’.

Fu, Q. and Hollars, S. (2004) ‘Testing Mixed-Phase Cloud Water Vapor Parameterizations with SHEBA/FIRE–ACE Observations’, *Journal of the*

Atmospheric Sciences, 61(16), pp. 2083–2091. Available at: https://doi.org/10.1175/1520-0469(2004)061<2083:TMCWVP>2.0.CO;2.

Godlovitch, D., Illner, R. and Monahan, A. (2011) 'Smoluchowski coagulation models of sea ice thickness distribution dynamics', *Journal of Geophysical Research: Oceans*, 116(C12), pp. 12005–12005. Available at: https://doi.org/10.1029/2011JC007125.

Held, I.M. and Soden, B.J. (2006) 'Robust Responses of the Hydrological Cycle to Global Warming', *Journal of Climate*, 19(21), pp. 5686–5699. Available at: https://doi.org/10.1175/JCLI3990.1.

Henry, M. *et al.* (2021) 'Decomposing the Drivers of Polar Amplification with a Single-Column Model', *Journal of Climate*, 34(6), pp. 2355–2365. Available at: https://doi.org/10.1175/JCLI-D-20-0178.1.

Henry, M. and Vallis, G.K. (2021) 'Reduced High-Latitude Land Seasonality in Climates with Very High Carbon Dioxide', *Journal of Climate*, 34(17), pp. 7325–7336. Available at: https://doi.org/10.1175/JCLI-D-21-0131.1.

Holland, M.M. *et al.* (2006) 'Influence of the sea ice thickness distribution on polar climate in CCSM3', *Journal of Climate*, 19(11), pp. 2398–2414. Available at: https://doi.org/10.1175/JCLI3751.1.

Holland, M.M., Bitz, C.M. and Tremblay, B. (2006) 'Future abrupt reductions in the summer Arctic sea ice', *Geophysical Research Letters*, 33(23). Available at: https://doi.org/10.1029/2006GL028024.

Horvat, C., Tziperman, E. and Campin, J.-M. (2016) 'Interaction of sea ice floe size, ocean eddies, and sea ice melting', *Geophysical Research Letters*, 43(15), pp. 8083–8090. Available at: https://doi.org/10.1002/2016GL069742.

Langen, P.L. and Alexeev, V.A. (2004) 'Multiple equilibria and asymmetric climates in the CCM3 coupled to an oceanic mixed layer with thermodynamic sea ice', *Geophysical Research Letters*, 31(4), pp. L04201–L04201. Available at: https://doi.org/10.1029/2003GL019039.

Le Treut, H. and Li, Z.-X. (1991) 'Sensitivity of an atmospheric general circulation model to prescribed SST changes: feedback effects associated with the simulation of cloud optical properties', *Climate Dynamics*, 5(3), pp. 175–187. Available at: https://doi.org/10.1007/BF00251808.

Lenton, T.M. *et al.* (2008) *Tipping elements in the Earth's climate system*. Available at: www.pnas.org/cgi/content/full/.

Lenton, T.M. (2013) 'Environmental Tipping Points', *Annual Review of Environment and Resources*, 38(1), pp. 1–29. Available at: https://doi.org/10.1146/annurev-environ-102511-084654.

Li, C. *et al.* (2013) 'The Transient versus the Equilibrium Response of Sea Ice to Global Warming', *Journal of Climate*, 26(15), pp. 5624–5636. Available at: https://doi.org/10.1175/JCLI-D-12-00492.1.

Liu, J. *et al.* (2016) 'Has arctic sea ice loss contributed to increased surface melting of the Greenland ice sheet?', *Journal of Climate*, 29(9), pp. 3373–3386. Available at: https://doi.org/10.1175/JCLI-D-15-0391.1.

Manabe, S. and Wetherald, R.T. (1975) 'The Effects of Doubling the CO2 Concentration on the climate of a General Circulation Model', *Journal of the Atmospheric Sciences*, 32(1), pp. 3–15. Available at: https://doi.org/10.1175/1520-0469(1975)032<0003:TEODTC>2.0.CO;2.

Maykut, G.A. and McPhee, M.G. (1995) 'Solar heating of the Arctic mixed layer', *Journal of Geophysical Research*, 100(C12). Available at: https://doi.org/10.1029/95jc02554.

Maykut, G.A. and Untersteiner, N. (1971) 'Some results from a time- dependent thermodynamic model of sea ice', *J Geophys Res*, 76(6), pp. 1550–1575. Available at: https://doi.org/10.1029/jc076i006p01550.

McIlhattan, E.A., Kay, J.E. and L'Ecuyer, T.S. (2020) 'Arctic Clouds and Precipitation in the Community Earth System Model Version 2', *Journal of Geophysical Research: Atmospheres*, 125(22), p. e2020JD032521. Available at: https://doi.org/10.1029/2020JD032521.

Medeiros, B. *et al.* (2011) 'Arctic Inversion Strength in Climate Models', *Journal of Climate*, 24(17), pp. 4733–4740. Available at: https://doi.org/10.1175/2011JCLI3968.1.

Mengel, J.G., Short, D.A. and North, G.R. (1988) 'Seasonal snowline instability in an energy balance model', *Climate Dynamics*, 2(3), pp. 127–131. Available at: https://doi.org/10.1007/BF01053470.

Merwin Monteiro, J., McGibbon, J. and Caballero, R. (2018) 'Sympl (v. 0.4.0) and climt (v. 0.15.3) - Towards a flexible framework for building model hierarchies in Python', *Geoscientific Model Development*, 11(9), pp. 3781–3794. Available at: https://doi.org/10.5194/gmd-11-3781-2018.

Moon, W. and Wettlaufer, J.S. (2012) 'On the existence of stable seasonally varying Arctic sea ice in simple models', *Journal of Geophysical Research: Oceans*, 117(C7). Available at: https://doi.org/10.1029/2012JC008006.

Moon, W. and Wettlaufer, J.S. (2017) 'A Stochastic Dynamical Model of Arctic Sea Ice', *Journal of Climate*, 30(13), pp. 5119–5140. Available at: https://doi.org/10.1175/JCLI-D-16-0223.1.

North, G.R. (1990) 'Multiple solutions in energy balance climate models', *Global and Planetary Change*, 2(3), pp. 225–235. Available at: https://doi.org/10.1016/0921-8181(90)90003-U.

Notz, D. *et al.* (2013) 'Arctic sea-ice evolution as modeled by Max Planck Institute for Meteorology's Earth system model', *Journal of Advances in Modeling Earth Systems*, 5(2), pp. 173–194. Available at: https://doi.org/10.1002/jame.20016.

Payne, A.E., Jansen, M.F. and Cronin, T.W. (2015) 'Conceptual model analysis of the influence of temperature feedbacks on polar amplification', *Geophysical*

Research Letters, 42(21), pp. 9561–9570. Available at: https://doi.org/10.1002/2015GL065889.

Perovich, D.K. *et al.* (2008) 'Sunlight, water, and ice: Extreme Arctic sea ice melt during the summer of 2007', *Geophysical Research Letters*, 35(11), pp. 11501–11501. Available at: https://doi.org/10.1029/2008GL034007.

Perovich, D.K. and Polashenski, C. (2012) 'Albedo evolution of seasonal Arctic sea ice', *Geophysical Research Letters*, 39(8), p. n/a-n/a. Available at: https://doi.org/10.1029/2012GL051432.

Persson, P.O.G. *et al.* (2002) 'Measurements near the Atmospheric Surface Flux Group tower at SHEBA: Near-surface conditions and surface energy budget', *Journal of Geophysical Research: Oceans*, 107(C10), p. SHE 21-1-SHE 21-35. Available at: https://doi.org/10.1029/2000JC000705.

Petty, A.A. *et al.* (2020) 'Winter Arctic Sea Ice Thickness From ICESat-2 Freeboards', *Journal of Geophysical Research: Oceans*, 125(5), p. e2019JC015764. Available at: https://doi.org/10.1029/2019JC015764.

Pincus, R., Barker, H.W. and Morcrette, J.-J. (2003) 'A fast, flexible, approximate technique for computing radiative transfer in inhomogeneous cloud fields', *Journal of Geophysical Research: Atmospheres*, 108(D13). Available at: https://doi.org/10.1029/2002JD003322.

Post, E. *et al.* (2013) 'Ecological consequences of sea-ice decline', *Science*, 341(6145), pp. 519–524. Available at: https://doi.org/10.1126/science.1235225.

Reed, K.A. and Jablonowski, C. (2012) 'Idealized tropical cyclone simulations of intermediate complexity: A test case for AGCMs', *Journal of Advances in Modeling Earth Systems*, 4(4). Available at: https://doi.org/10.1029/2011MS000099.

Ridley, J.K., Lowe, J.A. and Hewitt, H.T. (2012) 'How reversible is sea ice loss?', *Cryosphere*, 6(1), pp. 193–198. Available at: https://doi.org/10.5194/tc-6-193-2012.

Schweiger, A. *et al.* (2011) 'Uncertainty in modeled Arctic sea ice volume', *Journal of Geophysical Research: Oceans*, 116(C8). Available at: https://doi.org/10.1029/2011JC007084.

Sellers, W.D. (1969) 'A Global Climatic Model Based on the Energy Balance of the Earth-Atmosphere System', *Journal of Applied Meteorology (1962-1982)*, 8(3), pp. 392–400.

Semmler, T. *et al.* (2016) 'Seasonal Atmospheric Responses to Reduced Arctic Sea Ice in an Ensemble of Coupled Model Simulations', *Journal of Climate*, 29(16), pp. 5893–5913. Available at: https://doi.org/10.1175/JCLI-D-15-0586.1.

Serreze, M.C. *et al.* (2007) 'The large-scale energy budget of the Arctic', *Journal of Geophysical Research Atmospheres*, 112(11), pp. 1–17. Available at: https://doi.org/10.1029/2006JD008230.

Serreze, M.C. and Barry, R.G. (2014) *The Arctic Climate System*. 2nd edn. Edited by A.J. Dessler, J.T. Houghton, and M.J. Rycroft. Cambridge University Press, p. 442.

Shupe, M.D. and Intrieri, J.M. (2004) 'Cloud Radiative Forcing of the Arctic Surface: The Influence of Cloud Properties, Surface Albedo, and Solar Zenith Angle', *Journal of Climate*, 17(3), pp. 616–628. Available at: https://doi.org/10.1175/1520-0442(2004)017<0616:CRFOTA>2.0.CO;2.

Stefan, J. (1891) 'Ueber die Theorie der Eisbildung, insbesondere über die Eisbildung im Polarmeere', *Annalen der Physik*, 278(2), pp. 269–286. Available at: https://doi.org/10.1002/andp.18912780206.

Stommel, H. (1961) 'Thermohaline Convection with Two Stable Regimes of Flow', *Tellus*, 13(2), pp. 224–230. Available at: https://doi.org/10.1111/j.2153-3490.1961.tb00079.x.

Sundqvist, H. (1978) 'A parameterization scheme for non-convective condensation including prediction of cloud water content', *Quarterly Journal of the Royal Meteorological Society*, 104(441), pp. 677–690. Available at: https://doi.org/10.1002/QJ.49710444110.

Tao, W.-K., Simpson, J. and McCumber, M. (1989) 'An ice-water saturation adjustment', *Monthly Weather Review*, 117(1), pp. 231–235. Available at: https://doi.org/10.1175/1520-0493(1989)117<0231:aiwsa>2.0.co;2.

Thorndike, A. (2000) 'Sea ice thickness as a stochastic process', *Journal of Geophysical Research: Oceans*, 105(C1), pp. 1311–1313. Available at: https://doi.org/10.1029/1999JC900271.

Thorndike, A.S. *et al.* (1975) 'The thickness distribution of sea ice', *Journal of Geophysical Research*, 80(33), pp. 4501–4513. Available at: https://doi.org/10.1029/jc080i033p04501.

Thorndike, A.S. (1992a) 'A toy model linking atmospheric thermal radiation and sea ice growth', *Journal of Geophysical Research: Oceans*, 97(C6), pp. 9401–9410. Available at: https://doi.org/10.1029/92JC00695.

Thorndike, A.S. (1992b) 'Estimates of sea ice thickness distribution using observations and theory', *Journal of Geophysical Research: Oceans*, 97(C8), pp. 12601–12605. Available at: https://doi.org/10.1029/92JC01199.

Tietsche, S. *et al.* (2011) 'Recovery mechanisms of Arctic summer sea ice', *Geophysical Research Letters*, 38(2), p. n/a-n/a. Available at: https://doi.org/10.1029/2010GL045698.

Toppaladoddi, S., Moon, W. and Wettlaufer, J.S. (2023) 'Seasonal Evolution of the Arctic Sea Ice Thickness Distribution', *Journal of Geophysical Research: Oceans*, 128(5), p. e2022JC019540. Available at: https://doi.org/10.1029/2022JC019540.

Toppaladoddi, S. and Wettlaufer, J.S. (2015) 'Theory of the Sea Ice Thickness Distribution', *Physical Review Letters*, 115(14). Available at: https://doi.org/10.1103/PhysRevLett.115.148501.

Toppaladoddi, S. and Wettlaufer, J.S. (2017) ‘Statistical Mechanics and the Climatology of the Arctic Sea Ice Thickness Distribution’, *Journal of Statistical Physics*, 167(3–4), pp. 683–702. Available at: https://doi.org/10.1007/s10955-016-1704-8.

Vella, D. and Wettlaufer, J.S. (2008) ‘Explaining the patterns formed by ice floe interactions’, *Journal of Geophysical Research: Oceans*, 113(C11). Available at: https://doi.org/10.1029/2008JC004781.

Wagner, T.J.W. and Eisenman, I. (2015a) ‘False alarms: How early warning signals falsely predict abrupt sea ice loss’, *Geophysical Research Letters*, 42(23), p. 10,333-10,341. Available at: https://doi.org/10.1002/2015GL066297.

Wagner, T.J.W. and Eisenman, I. (2015b) ‘How Climate Model Complexity Influences Sea Ice Stability’, *Journal of Climate*, 28(10), pp. 3998–4014. Available at: https://doi.org/10.1175/jcli-d-14-00654.1.

Winton, M. (2006a) ‘Amplified Arctic climate change: What does surface albedo feedback have to do with it?’, *Geophysical Research Letters*, 33(3). Available at: https://doi.org/10.1029/2005GL025244.

Winton, M. (2006b) ‘Does the Arctic sea ice have a tipping point?’, *Geophysical Research Letters*, 33(23). Available at: https://doi.org/10.1029/2006GL028017.

Winton, M. (2008) ‘Sea Ice-Albedo Feedback and Nonlinear Arctic Climate Change’, in *Arctic Sea Ice Decline: Observations, Projections, Mechanisms, and Implications*. wiley, pp. 111–131. Available at: https://doi.org/10.1029/180GM09.

Yoshimori, M. *et al.* (2014) ‘Relative contribution of feedback processes to Arctic amplification of temperature change in MIROC GCM’, *Climate Dynamics*, 42(5–6), pp. 1613–1630. Available at: https://doi.org/10.1007/s00382-013-1875-9.

Zeeman, E.C. (1982) ‘Bifurcation, Catastrophe, and Turbulence’, in P.J. Hilton and G.S. Young (eds) *New Directions in Applied Mathematics: Papers Presented April 25/26, 1980, on the Occasion of the Case Centennial Celebration*. New York, NY: Springer, pp. 109–153. Available at: https://doi.org/10.1007/978-1-4612-5651-9_7.

Zickfeld, K. *et al.* (2005) ‘Is the Indian summer monsoon stable against global change?’, *Geophysical Research Letters*, 32(15). Available at: https://doi.org/10.1029/2005GL022771.